

CERN/LHCC/2008-004
ATLAS TDR 18
17 January 2008

ATLAS Forward Detectors for Measurement of Elastic Scattering and Luminosity

ATLAS Collaboration

Technical Design Report

Issue:	1
Revision:	0
Reference:	ATLAS TDR 018, CERN/LHCC 2008-04
Created:	17 January 2008
Last modified:	17 January 2008
Prepared by:	ATLAS Luminosity and Forward Physics Community

All trademarks, copyright names and products referred to in this document are acknowledged as such.

ATLAS Collaboration

Argentina

University of Buenos Aires, Buenos Aires
National University of La Plata, La Plata

Armenia

Yerevan Physics Institute, Yerevan

Australia

Research Centre for High Energy Physics, Melbourne University, Melbourne
University of Sydney, Sydney

Austria

Institut für Experimentalphysik der Leopold-Franzens-Universität Innsbruck, Innsbruck
Fachhochschule Wiener Neustadt (FHWN), Wiener Neustadt

Azerbaijan Republic

Institute of Physics, Azerbaijan Academy of Science, Baku

Republic of Belarus

Institute of Physics, National Academy of Science, Minsk
National Centre for Particle and High Energy Physics, Minsk

Brazil

Universidade Federal do Rio de Janeiro, COPPE/EE/IF, Rio de Janeiro

Canada

University of Alberta, Edmonton
University of Carleton/C.R.P.P., Carleton
Group of Particle Physics, University of Montreal, Montreal
Department of Physics, McGill University, Montreal
University of Regina, Regina
Department of Physics, University of Toronto, Toronto
Simon Fraser University, Burnaby, BC
TRIUMF, Vancouver
Department of Physics, University of British Columbia, Vancouver
University of Victoria, Victoria

CERN

European Laboratory for Particle Physics (CERN), Geneva

Chile

Pontificia Universidad Catolica de Chile (PUC), Santiago and Universidad Tecnica Federico Santa Maria (UTFSM), Valparaiso

China

Joint Cluster formed by IHEP Beijing, USTC Hefei, University of Nanjing and University of Shandong

Colombia

Universidad Antonio Narino (UAN), Bogota

Czech Republic

Academy of Sciences of the Czech Republic, Institute of Physics and Institute for Computer Science, Prague
Charles University in Prague, Faculty of Mathematics and Physics, Prague
Czech Technical University in Prague, Faculty of Nuclear Sciences and Physical Engineering, Faculty of Mechanical Engineering, Prague

Denmark

Niels Bohr Institute, University of Copenhagen, Copenhagen

France

Laboratoire d'Annecy-le-Vieux de Physique des Particules (LAPP), IN2P3-CNRS, Annecy-le-Vieux
Laboratoire de Physique Corpusculaire, Université Blaise Pascal (LPC), IN2P3-CNRS, Clermont-Ferrand
Laboratoire de Physique Subatomique et de Cosmologie de Grenoble (LPSC), IN2P3-CNRS Université Joseph Fourier, Grenoble
Centre de Physique des Particules de Marseille (CPPM), IN2P3-CNRS, Marseille
Laboratoire de l'Accélérateur Linéaire (LAL), IN2P3-CNRS, Orsay
LPNHE, Universités de Paris VI et VII, IN2P3-CNRS, Paris
Commissariat à l'Energie Atomique (CEA), DSM/DAPNIA, Centre d'Etudes de Saclay, Gif-sur-Yvette

Georgia

Institute of Physics of the Georgian Academy of Sciences and Tbilisi State University, Tbilisi

Germany

Physikalisches Institut, Universität Bonn, Bonn
Institut für Physik, Universität Dortmund, Dortmund
Technical University Dresden, Dresden
Fakultät für Physik, Albert-Ludwigs-Universität, Freiburg
Justus-Liebig University Giessen, Giessen
Universität Goettingen, Goettingen
Institut für Hochenergiephysik der Universität Heidelberg, Heidelberg
Humboldt Universität Berlin, Institut für Physik, Berlin
Institut für Physik, Universität Mainz, Mainz
Lehrstuhl für Informatik V, Universität Mannheim, Mannheim
Sektion Physik, Ludwig-Maximilian-Universität München, Munich
Max-Planck-Institut für Physik, Munich
Fachbereich Physik, Universität Siegen, Siegen
Fachbereich Physik, Bergische Universität, Wuppertal
DESY, Hamburg und Zeuthen
Max-Planck Institut für Physik, Munich

Greece

Athens National Technical University, Athens
Athens University, Athens
Aristotle University of Thessaloniki, High Energy Physics Department and Department of Mechanical Engineering, Thessaloniki

Israel

Department of Physics, Technion, Haifa
Raymond and Beverly Sackler Faculty of Exact Sciences, School of Physics and Astronomy, Tel-Aviv University, Tel-Aviv
Department of Particle Physics, The Weizmann Institute of Science, Rehovot

Italy

Dipartimento di Fisica dell'Università di Bologna e I.N.F.N., Bologna
Dipartimento di Fisica dell'Università della Calabria e I.N.F.N., Cosenza
Laboratori Nazionali di Frascati dell'I.N.F.N., Frascati
Dipartimento di Fisica dell'Università di Genova and I.N.F.N., Genova
Dipartimento di Fisica dell'Università di Lecce e I.N.F.N., Lecce
Dipartimento di Fisica dell'Università di Milano e I.N.F.N., Milan
Dipartimento di Scienze Fisiche, Università di Napoli 'Federico II' et I.N.F.N., Naples
Dipartimento di Fisica Nucleare e Teorica dell'Università di Pavia e I.N.F.N., Pavia
Dipartimento di Fisica dell'Università di Pisa e I.N.F.N., Pisa
Dipartimento di Fisica dell'Università di Roma I 'La Sapienza' and I.N.F.N., Roma

Dipartimento di Fisica dell'Università di Roma II 'Tor Vergata' and I.N.F.N., Roma
Dipartimento di Fisica dell'Università di Roma III 'Roma Tre' and I.N.F.N., Roma
Dipartimento di Fisica dell'Università di Udine, Gruppo collegato di Udine I.N.F.N. Trieste, Udine

Japan

Hiroshima Institute of Technology, Hiroshima
Department of Physics, Hiroshima University, Higashi-Hiroshima
KEK, High Energy Accelerator Research Organisation, Tsukuba
Kobe University, Kobe
Department of Physics, Kyoto University, Kyoto
Kyoto University of Education, Kyoto
Nagasaki Institute of Applied Science, Nagasaki
Nagoya University, Nagoya
Department of Physics, Faculty of Science, Okayama University, Okayama
Osaka University, Osaka
Department of Computer Science, Ritsumeikan University, Kusatsu
Department of Physics, Faculty of Science, Shinshu University, Matsumoto
International Center for Elementary Particle Physics, University of Tokyo, Tokyo
Physics Department, Tokyo Metropolitan University, Tokyo
Institute of Physics, University of Tsukuba, Tsukuba

Morocco

Faculté des Sciences Ain Chock, Université Hassan II, Casablanca, and Université Mohamed V, Rabat

Netherlands

FOM - Institute SAF NIKHEF and University of Amsterdam/NIKHEF
University of Nijmegen/NIKHEF, Nijmegen

Norway

University of Bergen, Bergen
University of Oslo, Oslo

Poland

Faculty of Physics and Applied Computer Science, AGH-University of Science and Technology, Cracow
H. Niewodniczanski Institute of Nuclear Physics, Polish Academy of Sciences, Cracow

Portugal

Laboratório de Instrumentação e Física Experimental de Partículas (LIP), Lisbon, in collaboration with: University of Lisboa, University of Coimbra, University Católica-Figueira da Foz and University Nova de Lisboa

Romania

National Institute for Physics and Nuclear Engineering, Institute of Atomic Physics, Bucharest

Russia

Institute for Theoretical and Experimental Physics (ITEP), Moscow
P.N. Lebedev Institute of Physics, Moscow
Moscow Engineering and Physics Institute (MEPhI), Moscow
Moscow State University, Moscow
Budker Institute of Nuclear Physics (BINP), Novosibirsk
State Research Center of the Russian Federation - Institute for High Energy Physics (IHEP), Protvino
Petersburg Nuclear Physics Institute (PNPI), Gatchina, St. Petersburg

JINR

Joint Institute for Nuclear Research , Dubna

Republic of Serbia

Institute of Physics, University of Belgrade, Belgrade

Slovak Republic

Bratislava University, Bratislava, and Institute of Experimental Physics of the Slovak Academy of Sciences, Kosice

Slovenia

Jozef Stefan Institute and Department of Physics, University of Ljubljana, Ljubljana

Spain

Institut de Física d'Altes Energies (IFAE), Universidad Autónoma de Barcelona, Bellaterra (Barcelona)

Physics Department, Universidad Autónoma de Madrid, Madrid

Instituto de Física Corpuscular (IFIC), Centro Mixto Universidad de Valencia - CSIC, Valencia and Instituto de Microelectrónica de Barcelona, Bellaterra (Barcelona)

Sweden

Fysika institutionen, Lunds universitet, Lund

Royal Institute of Technology (KTH), Stockholm

University of Stockholm, Stockholm

Uppsala University, Department of Radiation Sciences, Uppsala

Switzerland

Laboratory for High Energy Physics, University of Bern, Bern

Section de Physique, Université de Genève, Geneva

Taiwan

Institute of Physics, Academia Sinica, Taipei

Turkey

Department of Physics, Ankara University, Ankara

Department of Physics, Bogaziçi University, Istanbul

United Kingdom

School of Physics and Astronomy, The University of Birmingham, Birmingham

Cavendish Laboratory, Cambridge University, Cambridge

Department of Physics and Astronomy, University of Glasgow, Glasgow

Department of Physics, Lancaster University, Lancaster

Department of Physics, Oliver Lodge Laboratory, University of Liverpool, Liverpool

Department of Physics, Queen Mary and Westfield College, University of London, London

Department of Physics, Royal Holloway and Bedford New College, Egham

Department of Physics and Astronomy, University College London, London

Department of Physics and Astronomy, University of Manchester, Manchester

Department of Physics, Oxford University, Oxford

Rutherford Appleton Laboratory, Chilton, Didcot

Department of Physics, University of Sheffield, Sheffield

United States of America

State University of New York at Albany, New York

Argonne National Laboratory, Argonne, Illinois

University of Arizona, Tucson, Arizona

Department of Physics, The University of Texas at Arlington, Arlington, Texas

Lawrence Berkeley Laboratory and University of California, Berkeley, California

Physics Department of the University of Boston, Boston, Massachusetts

Brandeis University, Department of Physics, Waltham, Massachusetts

Brookhaven National Laboratory (BNL), Upton, New York

University of Chicago, Enrico Fermi Institute, Chicago, Illinois

Nevis Laboratory, Columbia University, Irvington, New York

Department of Physics, Duke University, Durham, North Carolina

Department of Physics, Hampton University, Virginia

Department of Physics, Harvard University, Cambridge, Massachusetts

Indiana University, Bloomington, Indiana
Iowa State University, Ames, Iowa
University of California, Irvine, California
Department of Physics, University of Massachusetts, Amherst
Massachusetts Institute of Technology, Department of Physics, Cambridge, Massachusetts
Michigan State University, Department of Physics and Astronomy, East Lansing, Michigan
University of Michigan, Department of Physics, Ann Arbor, Michigan
Department of Physics, New Mexico University, Albuquerque
Department of Physics, New York University, New York
Ohio State University, Columbus, Ohio
Department of Physics and Astronomy, University of Oklahoma
Oklahoma State University, Oklahoma
University of Oregon, Eugene, Oregon
Department of Physics, University of Pennsylvania, Philadelphia, Pennsylvania
University of Pittsburgh, Pittsburgh, Pennsylvania
Institute for Particle Physics, University of California, Santa Cruz, California
Department of Physics, Southern Methodist University, Dallas, Texas
Stanford Linear Accelerator Center, Stanford, California
State University of New York at Stony Brook, New York
Tufts University, Medford, Massachusetts
High Energy Physics, University of Illinois, Urbana, Illinois
Department of Physics, Department of Mechanical Engineering, University of Washington, Seattle, Washington
Department of Physics, University of Wisconsin, Madison, Wisconsin
Physics Department, University of Yale, New Haven, New York

Table of Contents

1	Introduction	11
1.1	References.	12
2	Methods for absolute luminosity determination	13
2.1	Elastic scattering at small angles as a handle on luminosity	13
2.2	Luminosity determination from Coulomb scattering.	14
2.3	Alternative determination of luminosity without ALFA	16
2.4	References.	17
3	Required beam properties	19
3.1	Requirement on the optics	19
3.2	Optics solution	21
3.3	Injection and transition optics.	23
3.4	Beam emittance	25
3.5	Collimation and beam halo	26
3.6	Luminosity and bunch structure	29
3.7	Determination of beam parameters	29
3.8	References.	30
4	The Roman Pot mechanics and installation	33
4.1	Introduction	33
4.2	Roman Pot mechanics	34
4.3	RF impedance and coupling with LHC beams	38
4.4	Positioning system	40
4.5	Installation and alignment	42
4.6	Roman Pots mechanics status.	44
4.7	References.	45
5	The Roman Pot detectors.	47
5.1	The detector requirements	47
5.2	The ALFA scintillating fibre detector	48
5.3	Performance estimates	58
5.4	Detector construction and metrology	59
5.5	References.	63
6	The ALFA read-out electronics	65
6.1	Introduction	65
6.2	System description	66
6.3	Roman Pot station overview	67
6.4	MAROC Front-End chip	68
6.5	PMF.	71
6.6	Roman Pot motherboard	72
6.7	Low voltage and high voltage power sources	74
6.8	Radiation level	75
6.9	References.	75

7	The ALFA trigger and read-out	77
7.1	Trigger and read-out overview	77
7.2	Trigger infrastructure and integration with ATLAS	78
7.3	Timing, Trigger and Control	81
7.4	Read-Out Drivers	81
7.5	Read-Out System	82
7.6	Detector Control System	82
7.7	Alternative read-out modes	83
7.8	References	83
8	Test beam results and future activities	85
8.1	Prototype test at DESY	85
8.2	Prototype test at CERN	88
8.3	Plans for future prototype and test beam activities	95
8.4	References	96
9	Performance estimations	99
9.1	Measurement method	99
9.2	Simulation setup	99
9.3	Expected performance	101
9.4	Luminosity and forward physics parameters	107
9.5	Summary	110
9.6	References	111
10	Machine interface, commissioning and operation	113
10.1	Beam interlock, beam loss monitors and machine protection	113
10.2	Radiation environment	113
10.3	Cables and other services	114
10.4	Powering the high beta optics	114
10.5	Commissioning	114
10.6	Operation	115
10.7	References	116
11	Responsibilities, cost and schedule	117
11.1	Responsibilities	117
11.2	Cost	117
11.3	Schedule	119
A	Members of the ATLAS ALFA Collaboration	121

1 Introduction

This Technical Design Report (TDR) describes how we intend to complement the ATLAS detector [1-1] with a set of detectors in the very forward region. This was previously discussed in a Letter of Intent to the LHCC [1-2]. The proposed detectors will be located in the LHC tunnel far away from the Interaction Point (IP). The basic idea is to measure elastic scattering at very small angles in order to get a handle on the absolute luminosity at the interaction point of ATLAS. We will approach the detectors very close to the LHC beam using “Roman Pots”. The name originates from the CERN-Rome group that in the early 70th invented this technique to study elastic scattering at the ISR [1-3]. The pots are cylindrical vessels, which are separated from the machine vacuum and equipped with bellows that allow the pots to approach the beam. This technique has since the early days of the ISR been used extensively by a number of different experiments. It was used by UA4 at CERN [1-4] when the SPS was used as a collider and later Roman Pots have been installed in the Tevatron [1-5][1-6], in RHIC [1-7] and in HERA [1-8][1-9]. More recently, the TOTEM experiment at CERN [1-10] has proposed to install Roman Pots in the LHC.

The ATLAS Roman Pots, that are discussed in this TDR, will house position sensitive detectors. As will be discussed later, we are proposing to build scintillating fiber trackers. The Roman Pots with its detectors will be installed on both sides of the Intersection Point in order to measure elastic scattering of the protons in a constrained way. The Roman Pot technique will make it possible to approach the beam to distances in the millimeter range. The small distance from the beam together with a special optics of the LHC lattice will allow to measure the elastically scattered protons down to very small scattering angles. Our aim is to reach the Coulomb Interference Region and in this way get an absolute calibration of the luminosity using the computable electromagnetic cross section. However, as will be discussed later, even without reaching the Coulomb region we will get a handle on the luminosity using the hadronically scattered protons and the optical theorem.

ATLAS pursue a number of different approaches to get an accurate estimate of the absolute luminosity. The first estimate of the luminosity of LHC will certainly come from estimates based on the machine parameters even though this method will not be of highest accuracy, at least to start with. Apart from the Coulomb normalization method discussed in this TDR, we also intend to use other processes with cross sections known to a certain degree of accuracy. The W and Z production is theoretically well investigated and there is more and more accurate data on the relevant parton distribution functions from many experiments. Another promising example is the QED process of muon pair production from double photon exchange.

On a longer time scale we see the use of Roman Pots for elastic scattering and luminosity determination as a first step towards a more extensive program of forward physics. We hope to learn about the possibilities and the difficulties in working close to the LHC beam. This will allow us to extend the program later by placing additional detectors in suitable positions in the LHC lattice in order to increase the measurable kinematical range of the forward protons.

The TDR is organized in the following manner: in chapter 2 we discuss different methods of measuring the absolute luminosity and chapter 3 concentrates on the required beam properties for Coulomb scattering. Chapter 4 deals with the Roman Pots, their mechanics and movement systems, as well as their installation and alignment. The detector is described in chapter 5 and the electronics in chapter 6. Chapter 7 deals with the trigger and read-out issues. Chapter 8 gives the result from two different test beam campaigns. The expected performance as obtained from simulations are discussed in chapter 9. In chapter 10, machine interface, commissioning and operation is treated and finally chapter 11 deals with the resources and schedule.

1.1 References

- 1-1 ATLAS Collaboration, “*Technical Proposal for a General-Purpose pp Experiment at the Large Hadron Collider at CERN*”, ATLAS Technical Proposal, CERN-LHCC/94-43 (1994).
- 1-2 ATLAS Collaboration, “*ATLAS Forward Detectors for Luminosity Measurement and Monitoring*”, Letter of Intend, CERN-LHCC/2004-010 (2004).
- 1-3 CERN-Rome collaboration, “*The Real Part of the Forward Proton Proton Scattering Amplitude Measurement at the CERN Intersecting Storage Rings*”, Phys. Lett. 66 B (1977) 390-394.
- 1-4 UA4 Collaboration, D. Bernard et. al., “*The Real Part of the Forward Proton Antiproton Elastic Scattering Amplitude at the Centre of Mass Energy of 546 GeV*”, Phys. Lett. B 198 (1987) 583-589.
- 1-5 F. Abe et al., “*Measurement of small angle antiproton-proton elastic scattering at $\sqrt{s} = 546$ and 1800 GeV*”, Phys. Rev. D 50, 5518 (1994).
- 1-6 A. Brandt et al., “*A Forward Proton Detector at DØ*”, FERMILAB-PUB-97/377.
- 1-7 PP2PP Collaboration, “*The PP2PP experiment at RHIC: silicon detectors installed in Roman Pots for forward proton detection close to the beam*”, Nucl. Instrum. and Meth. A 535, 415-420 (2004).
- 1-8 P. van Esch et al., “*The H1 forward proton spectrometer at HERA*”, Nucl. Instrum. and Meth. A, 446, 409-425 (2000).
- 1-9 ZEUS Collaboration, M. Derrick et al., “*The ZEUS Leading Proton Spectrometer and its Use in the Measurement of Elastic ρ^0 Photoproduction at HERA*”, DESY 96-183, Zeitschrift f. Physik C73 (1997) 2, 253-268.
- 1-10 TOTEM Collaboration, “*Total Cross Section, Elastic Scattering and Diffraction Dissociation at the Large Hadron Collider*”, Technical Design Report, CERN-LHCC/2004-002 (2004).

2 Methods for absolute luminosity determination

2.1 Elastic scattering at small angles as a handle on luminosity

The rate of elastic scattering is linked to the total interaction rate through the optical theorem, which states that the total cross section is directly proportional to the imaginary part of the forward elastic scattering amplitude extrapolated to zero momentum transfer:

$$\sigma_{tot} = 4\pi \cdot \text{Im}[f_{el}(t=0)] \quad 2-1$$

where at small values of t :

$$-t = (p\theta)^2 \quad 2-2$$

Here p is the beam momentum and θ the forward scattering angle. Equation 2-2 is a valid approximation for the small values of θ we are considering here. The optical theorem implies that a measurement of elastic scattering in the forward direction will always provide additional information on the luminosity. This fact can be used in several ways which are described below.

2.1.1 Luminosity determination using elastic scattering and the inelastic rate

By measuring the total interaction rate R_{tot} and the elastic rate $dR_{el}/dt|_{t=0}$ in the forward direction simultaneously, both the luminosity and the total cross section can be determined. The expressions, which can be directly derived from the optical theorem and the definition of luminosity $L = R/\sigma$, are given in (2-3) and (2-4) below:

$$L = \frac{1}{16\pi} \frac{R_{tot}^2 (1 + \rho^2)}{dR_{el}/dt|_{t=0}} \quad 2-3$$

$$\sigma_{tot} = \frac{16\pi}{(1 + \rho^2)} \frac{dR_{el}/dt|_{t=0}}{R_{tot}} \quad 2-4$$

where ρ is defined as:

$$\rho \equiv \left. \frac{\text{Re } f_{el}(t)}{\text{Im } f_{el}(t)} \right|_{t=0} \quad 2-5$$

The ρ -parameter is sufficiently well known not to contribute significantly to the systematic error. Recent predictions of the ρ -parameter at LHC energies is in the range 0.13-0.14 [2-1]. Assuming an error of ± 0.02 implies an uncertainty less than 0.5% in the luminosity from the uncertainty of ρ .

Using (2-3) above is the standard way of determining the luminosity from elastic scattering. This method requires a precise measurement of the inelastic rate with good coverage in rapidity η . The η range of ATLAS is somewhat limited in this context. The accuracy of the luminosity determination will be dominated by the uncertainty of Monte-Carlo based extrapolations of the inelastic rate to the highest η values.

2.1.2 Luminosity determination using elastic scattering at very small t -values

A different approach is to measure elastic scattering down to such small t -values that the cross section becomes sensitive to the electromagnetic amplitude. Using this additional constraint from the Coulomb term allows determination of both luminosity and the total cross section without a measurement of the inelastic rate. This method was used previously by the UA4 collaboration at the CERN SPS where a precision of 3% on the absolute luminosity measurement was achieved [2-2]. In this TDR we propose to use the same method. For ATLAS, having a precision of a few percent would be adequate for most analyses.

To reach the Coulomb interference region at the LHC is a very challenging task, as will be discussed in Section 2.2. Some of the conditions needed for a satisfactory measurement are close to the expected performance limits of the machine, which might only be known once the machine is built and operated. After some first experience has been gained with the machine and the Roman Pot operation, we aim to obtain a precision in the luminosity measurement of around 3%.

2.1.3 Alternate ways of luminosity determination using elastic scattering

While the determination of absolute luminosity by Coulomb normalization is our primary goal, we argue that a measurement of the extrapolated forward elastic rate will improve the understanding of the absolute luminosity at the ATLAS interaction point even if the Coulomb interference region is not reached. The extrapolation to the “optical point” can be used in several independent ways:

- Replacing R_{tot} in (2-3) above with $L \sigma_{tot}$ gives:

$$\frac{1}{L} = \frac{1}{16\pi} \frac{\sigma_{tot}^2 (1 + \rho^2)}{dR_{el}/dt} \Big|_{t=0} \quad 2-6$$

Thus we see that the extrapolation to $t = 0$ together with an independent measurement of the total cross section gives the luminosity. ATLAS could use the total cross section as determined by TOTEM [2-3] and thus determine the luminosity at the ATLAS Interaction Point.

- As mentioned above, (2-3) could also be used in spite of the limited η coverage of ATLAS. In this case, the accuracy of the luminosity determination would be dominated by the uncertainty of the inelastic rate at high η values. We would then have to rely upon Monte-Carlo estimates of this rate.
- Formula (2-6) could also be used using the luminosity derived from LHC machine parameters in combination with a measurement of the forward elastic rate at ATLAS. Hence a determination of the total cross section with an uncertainty half that of the LHC derived luminosity can be achieved. In this way, the precision in the ratio of a given cross section over the total cross section will always be a factor two better than the precision of the absolute luminosity obtained from the machine parameters.

2.2 Luminosity determination from Coulomb scattering

The rate of elastic scattering at small t -values can be written as

$$\frac{dN}{dt} = L\pi |f_C + f_N|^2 \approx L\pi \left| -\frac{2\alpha}{|t|} + \frac{\sigma_{tot}}{4\pi} (i + \rho) e^{-b|t|/2} \right|^2 \quad 2-7$$

where the first term corresponds to the Coulomb and the second to the strong interaction amplitude. In the above formula we have for simplicity excluded the proton form factor. The formula is oversimplified and there are also other corrections that should be included in the final analysis. Figure 2-1 illustrates the different contributions to the elastic cross section as given by (2-7). The Coulomb region, the strong interaction region and the interference region are clearly seen.

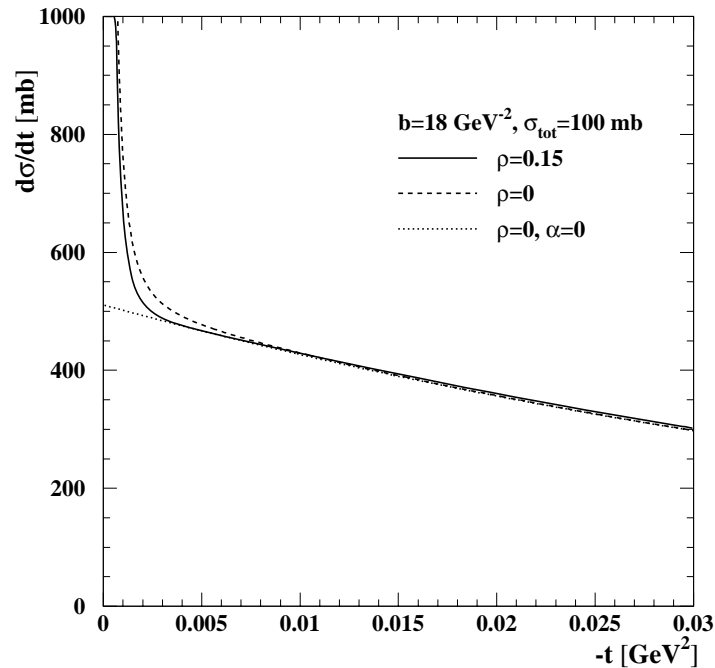


Figure 2-1 The elastic cross section as a function of t for a possible set of parameters at LHC energies. The data have been plotted for $\rho = 0$ and $\rho = 0.15$ to illustrate the Coulomb interference region. The data have also been plotted for $\alpha = 0$ to illustrate the strong interaction contribution.

At the nominal energy of the LHC (7 TeV), the strong amplitude is expected to equal the electromagnetic amplitude for $|t| = 0.00065 \text{ GeV}^2$. This corresponds to a scattering angle of $3.5 \mu\text{rad}$. To indicate the scale of the difficulty: at the SPS collider the Coulomb region was reached at scattering angles of $120 \mu\text{rad}$. This large difference is mainly due to the energy difference but also because the total cross section increases with energy. The need to reach such small scattering angles imposes very stringent requirements on the beam optics and the beam conditions, as well as on the detectors themselves.

The most suitable method concerning the optics employs a so-called parallel-to-point optics from the interaction point to the detector. In this type of optics the betatron oscillation between the interaction point of the elastic collision and the detector position has a 90 degree phase difference (in the proposed optics, this is only in the vertical plane), such that all particles scattered at the same angle are focused on the same locus at the detector, independent of the position of their interaction vertex position. Thus, a transverse position measurement at the detector translates directly to an angular measurement at the Interaction Point. In this kind of optics the beam is quasi-parallel at the Interaction Point and must have an intrinsic beam divergence significantly smaller than the smallest scattering angles to be observed. The divergence at the Interaction Point equals $\sqrt{\varepsilon/\beta^*}$, where ε is the emittance of the machine and β^* the beta-tron-function at the Interaction Point. Thus, a small emittance ε and a large β^* are required. In order to

reach the Coulomb region we need a normalized emittance ($\varepsilon_N = \varepsilon \cdot \gamma$) of the order of 10^{-6} m rad and β^* in the range 2000-3000 m.

For the position sensitive detectors we have chosen scintillating fibers which will allow us to come very close to the beam (see Chapter 5). We have called our system of scintillating fiber trackers ALFA (Absolute Luminosity For ATLAS) and all aspects of this system will be extensively discussed in this TDR.

Once the elastic rate has been measured the luminosity will be extracted by fitting (2-7) to the measured rate. The luminosity L will be determined from the fit as well as the other parameters ρ , σ_{tot} , and the slope parameter b . The details of this method and expected performance will be discussed in Chapter 9.

2.3 Alternative determination of luminosity without ALFA

In this TDR, the Coulomb normalization of the luminosity is proposed as the primary means of luminosity calibration. In addition, ATLAS has considered several alternative and complementary methods for the determination of the absolute and relative luminosity [2-4]. However, we want to stress that all the different approaches, with their individual strengths and weaknesses, complement each other and are an integral part of the full ATLAS luminosity program. They are all expected to contribute to the ultimate luminosity determination. These methods are:

- *The use of the LHC beam monitors to determine the bunch densities and the bunch-bunch effective overlap region at the IP*

Based on experience at previous machines, the determination of luminosity from machine monitor information is far from trivial and further complicated by the fact that the beam profiles at the Interaction Point cannot be directly accessed but must be extrapolated from measurements outside the experimental area. At the ISR the van der Meer beam scan method was employed to obtain a precise luminosity, and this is again considered for the LHC [2-5]. The precise limits to the accuracy of a machine-derived luminosity are currently not well known, with estimates ranging between 10 and 20%. However, with special efforts with dedicated runs and simplified machine conditions, a significantly better precision can be achieved [2-6]

It is arguable that the machine-derived luminosity will improve with experience gained in LHC operation. The LHC has been conceived “from the ground up” as a colliding beam machine, and much attention has been paid to machine instrumentation for beam diagnostics. Moreover, in running the machine with heavy ion beams, the experimental luminosity measurement is straightforward because the measurement of the forward neutron flux intercepted by so-called zero-degree calorimeter instrumentation inside the TAN radiation shield will measure the electromagnetic dissociation cross section precisely [2-7]. This has been demonstrated at RHIC where all the large detectors have adopted zero-degree calorimetry as part of their luminosity instrumentation. Thus, the cross calibration of machine instrumentation in heavy ion runs is expected to impose a powerful constraint and improve understanding and performance of the beam instrumentation in proton running.

- *Other well-calculable physics processes as luminosity monitors*

The most promising example of a QED process is the production of a muon pair by double photon exchange [2-8]. This process is experimentally clean but has a very small observable cross section because of the necessary p_T trigger conditions imposed on the muons.

Another process that has been proposed, and has been studied in some detail by ATLAS, is the QCD production of W and Z gauge bosons, and the measurement of their production rate times leptonic branching fraction. On the one hand this process measures the parton luminosity directly,

and hence may serve to normalize the parton luminosity in many other production processes of interest [2-9]. Alternatively, W/Z boson production is one of the best known QCD processes, and has been the subject of much recent theoretical work. In particular a differential calculation at NNLO of the cross-section is available[2-10], and fits to the Parton Distribution Functions at a matching order in QCD have been performed [2-11]. These developments promise to lead towards a theoretical uncertainty on the QCD cross-section to some few percents. In order to achieve this result the differences between the different PDF parametrisations in the region relevant for W/Z production at the LHC need to be mastered. Some recent work performed in ATLAS indicates that the ATLAS data themselves can be used in order to constrain the PDF's [2-12] in the relevant kinematic region. At this level of precision the Electroweak corrections need to be considered as well, and this is also a field of intense theoretical activity. Event generators incorporating these corrections[2-13] [2-14] have recently been interfaced to the ATLAS software. Based on these tools, studies are ongoing in ATLAS [2-15] to evaluate the uncertainty in the calculation of the experimental acceptance in presence of higher order corrections. The aim is mastering this uncertainty at the percent level, so that the measurement is dominated by the theoretical uncertainty on the absolute cross-section value.

2.4 References

- 2-1 J.R. Cudell et al., COMPETE Collaboration, “*Benchmarks for the forward observables at RHIC, the Tevatron Run II and the LHC*”, Phys. Rev. Lett. 89 (2002) 201801.
- 2-2 UA4 Collaboration, D. Bernard et. al., “*The Real Part of the Forward Proton Antiproton Elastic Scattering Amplitude at the Centre of Mass Energy of 546 GeV*”, Phys. Lett. B 198 (1987) 583-589.
- 2-3 TOTEM Collaboration, “*Total Cross Section, Elastic Scattering and Diffraction Dissociation at the Large Hadron Collider*”, Technical Design Report, CERN-LHCC/2004-002 (2004).
- 2-4 ATLAS Collaboration, “*Detector and Physics Performance*”, Technical Design Report, CERN-LHCC/99-14, Volume I, Chapter 13.
- 2-5 K. Potter, CERN Yellow Report, CERN 71-01 (1971).
- 2-6 H. Burkhardt and P. Grafstrom, “*Absolute luminosity from machine parameters*”, LHC-Project-Report-1019 (2007).
- 2-7 ATLAS Collaboration, “*Zero Degree Calorimeters for ATLAS*”, Letter of Intend, CERN-LHCC/2007-001 (2007).
- 2-8 A.G. Shamov and V.I. Telnov, “*Precision luminosity measurement at LHC using two-photon production of $\mu^+\mu^-$ pairs*”, Nucl. Instr. and Meth. A 494 (2002) 51-56.
- 2-9 M. Dittmar, F. Pauss and D. Zurcher, “*Towards a Precise Parton Luminosity Determination at the CERN LHC*”, Phys. Rev. D 56 (1997) 7284-7290.
- 2-10 C. Anastasiou, L.J. Dixon, K. Melnikov and F. Petriello, “*High-precision QCD at hadron colliders: Electroweak gauge boson rapidity distributions at NNLO*”, Phys. Rev. D 69 (2004) 094008 (hep-ph/0312266).
- 2-11 R.S. Thorne, A.D. Martin, R.G. Roberts and W.J. Stirling, “*Recent progress in parton distributions and implications for LHC physics*”, AIP Conf. Proc. **792**, (2005) 365 (hep-ph/0507015).
- 2-12 A. Tricoli, A.M. Cooper-Sarkar and C. Gwenlan, “*Uncertainties on W and Z production at the LHC*”, hep-ex/0509002.

- 2-13 C.M. Carloni Calame, G. Montagna, O. Nicrosini and A. Vicini, “*Precision electroweak calculation of the charged current Drell-Yan process*”, JHEP **0612** (2006) 016 (hep-ph/0609170).
- 2-14 W. Placzek and S. Jadach, “*Multiphoton radiation in leptonic W-boson decays*”, Eur. Phys. J. C **29** (2003) 325 (hep-ph/0302065).
- 2-15 M. Bellomo, PhD. thesis, Universita di Pavia 2007.

3 Required beam properties¹

To reach the Coulomb interference region it is necessary to measure very small scattering angles in the range of a few micro radians. This in turn requires both a small emittance beam and a special beam optics. Such a dedicated optics features a very large β^* at the ATLAS Interaction Point and a phase advance of the betatron function between the Interaction Point and the detectors of 90 degrees in at least one of the two transverse planes. An optics solution fulfilling the above requirements, hereafter called a high β^* -optics, can be used in combination with rather few bunches of low intensity as compared to nominal LHC to produce instantaneous luminosities in the range of $10^{27} \text{ cm}^{-2}\text{s}^{-1}$ to $10^{28} \text{ cm}^{-2}\text{s}^{-1}$.

3.1 Requirement on the optics

In general, the position of a trajectory in a transverse plane at a given point away from the IP, with a phase advance of ψ and a betatron function β at this point, is given by:

$$\begin{bmatrix} u(s) \\ u'(s) \\ (\Delta p)/p \end{bmatrix} = M \begin{bmatrix} u^* \\ u'^* \\ (\Delta p^*)/p \end{bmatrix} \quad 3-1$$

$$M = \begin{bmatrix} \sqrt{\beta/(\beta^*)}(\cos\psi + \alpha^* \sin\psi) & \sqrt{\beta \cdot \beta^*} \sin\psi & D_u \\ ((\alpha^* - \alpha)\cos\psi - (1 + \alpha\alpha^*)\sin\psi)/\sqrt{\beta/\beta^*} & \sqrt{\beta/(\beta^*)}(\cos\psi - \alpha \sin\psi) & D'_u \\ 0 & 0 & 1 \end{bmatrix} \quad 3-2$$

where u is any of the transversal space coordinates x , y and u' the trajectory slope, D is the dispersion acting on particles with a momentum loss $\Delta p/p$ and α is the spatial derivative of the betatron function. Quantities at the interaction point at $s=0$ are denoted by $*$. For elastic scattering the momentum loss is irrelevant and the dispersion acts only on the intrinsic energy smearing of the beam, of the order of 10^{-4} , which can be neglected. The observed displacement u off the nominal orbit in the detector plane is related to the particle vertex and trajectory slope at the Interaction Point by:

$$u = \sqrt{\beta/\beta^*}(\cos\psi + \alpha^* \sin\psi)u^* + \sqrt{\beta\beta^*} \sin\psi \cdot u'^* = M_{u,11} \cdot u^* + M_{u,12} \cdot \theta_u^* \quad 3-3$$

where $u'^* = \theta_u^*$ is the u -component of the scattering angle. For elastic scattering the vertex contributions to the left and right arm measurements are the same, while given the back-to-back topology the scattering angles are equal in size and opposite in sign. Hence when taking the difference of the left (L) and right (R) arm measurement the vertex contribution cancels:

$$u_L - u_R = 2M_{u,12} \cdot \theta_u^* \quad , \quad \theta_u^* = \frac{u_L - u_R}{2L_{eff,u}} \quad , \quad L_{eff,u} = \sqrt{\beta\beta^*} \sin\psi \quad 3-4$$

1. This chapter was written in collaboration with H. Burkhardt (AB/ABP).

where the effective lever arm L_{eff} determines the precision of the scattering angle measurement. The t -value is then determined by:

$$-t = p^2(\theta_x^{*2} + \theta_y^{*2}) \quad 3-5$$

and the details of the t reconstruction are given in Section 9.2.

The LHC has two separate beams in the horizontal plane with two beam pipes separated by only 194 mm. Thus there is a considerable technical advantage to approach the beam from above and below the beam axis compared to approach from the sides. We have optimized the optics for such an arrangement by using an optics with a 90-degree phase advance in the vertical plane. With this configuration we can estimate how small t values we can reach. The general formula (3-3) reduces to:

$$y = \sqrt{\beta\beta^*}\theta_y^* \quad 3-6$$

when the phase advance is $\pi/2$ and $\alpha^* \cong 0$ in the vertical plane.

The minimum t -value reachable (t_{min}) will then be given by particles unscattered in the horizontal plane and with the minimum scattering angle in the vertical plane:

$$-t_{min} = (p\theta_{min})^2 = p^2 y_d^2 / (\beta\beta^*) \quad 3-7$$

where y_d is the smallest distance possible between the center of the beam and the edge of the detector. The relevant variable for beam halo considerations is the distance from the beam center expressed in terms of the multiple of the rms size of the beam spot at the detector. The beam spot is given by:

$$\sigma = \sqrt{\varepsilon \cdot \beta} \quad 3-8$$

and thus y_d can be written as:

$$y_d = n_d \sqrt{\varepsilon \cdot \beta} \quad 3-9$$

where n_d is the smallest possible distance to the beam center expressed as a multiple of the beam spot rms size. From (3-7) and (3-9) it follows that t_{min} can be defined as:

$$-t_{min} = p^2 n_d^2 \frac{\varepsilon}{\beta^*} \quad 3-10$$

where

$$\varepsilon = \frac{\varepsilon_N}{\gamma} \quad 3-11$$

Here ε_N is the normalized emittance.

Thus t_{min} depends on the distance of the detectors to the beam, on the emittance, and on β^* . Using a normalized emittance ε_N of 1 μm rad, which we hope is reachable (Section 3.4), and a minimum distance to the detector corresponding to $n_d = 15$, we see that a t_{min} of 0.0006 GeV^2 can be reached for a β^* of 2600 meters or larger. At the value of t_{min} the acceptance vanishes and to get for example an acceptance of at least 50% at $-t=0.0006 \text{ GeV}^2$ the detector has to be placed at a closer distance of about $n_d=12$.

The formula (3-10) is relevant as long as the limitation in the closest approach to the beam is given by beam halo considerations. However, there is also another limiting factor independent of the beam halo. Possible instabilities in the closed orbit will put a limit on the minimum distance of approach. The exact limitation here is not precisely known today but will be in the millimeter range. In this case, y_d will be a fixed distance independent of the beam size and t_{min} will be proportional to $1/(\beta^*\beta)$ (see eq. (3-7)). Thus we have the additional requirement on the optics that β should not be too small. Putting in realistic numbers we find that β should be larger than about 70 meters.

We can therefore summarize the main requirements on the optics as follows:

- $\beta^* > 2600$ m, $\beta_d > 70$ m, $\alpha^* \approx 0$, negligible dispersion
- 90° phase advance in the vertical plane between the Interaction Point and the detector

3.2 Optics solution

Several high-beta optics and very high-beta insertions have been studied for the LHC [3-1][3-2][3-3][3-4]. Of those, only one has the potential of reaching the Coulomb region [3-4]. However this optics required an additional quadrupole to be introduced in the lattice. We have looked for an optics solution that does not require any hardware changes in the LHC layout, starting from the calculated optics for TOTEM with a β^* of 1540 meters [3-3].

We have found such a solution. It requires that the Roman Pots are placed between quadrupole 6 (Q6) and quadrupole 7 (Q7) in the LHC lattice. This location, which is located 240 meters away from the Interaction Point, is indicated in Figure 3-1. The solution does not require any hardware changes but it requires that quadrupole 4 (Q4) works with reversed polarity as compared to the standard optics.

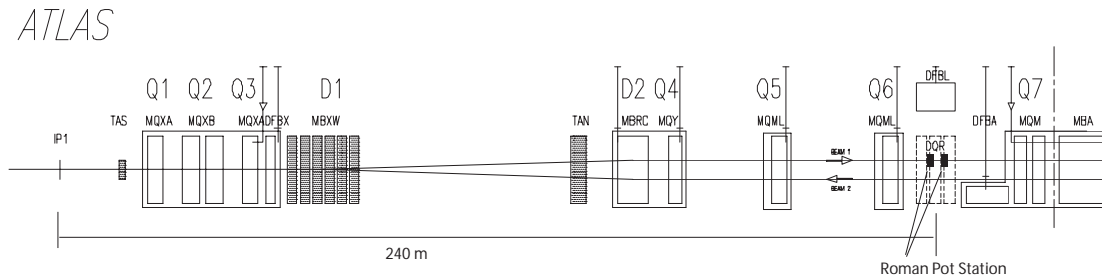


Figure 3-1 Schematic layout of the LSS1 near ATLAS with the proposed location of the Roman Pot station as seen from the center of the LHC (one side).

The possibility to switch the polarities of Q4 is discussed in Section 10.4. Figure 3-2 shows the optical functions of this solution, which has a β^* of 2625 m and Figure 3-3 shows the associated dispersion and phase advance. This optics is compatible with the optics that has been prepared by the TOTEM collaboration for the measurement of the total cross section with a β^* of 1540 m and thus TOTEM and ATLAS can run high beta optics at the same time. The expected performance of this optics in terms of acceptance and reachable t -values is discussed in Section 9.

The most significant parameters are summarized in Table 3-1.

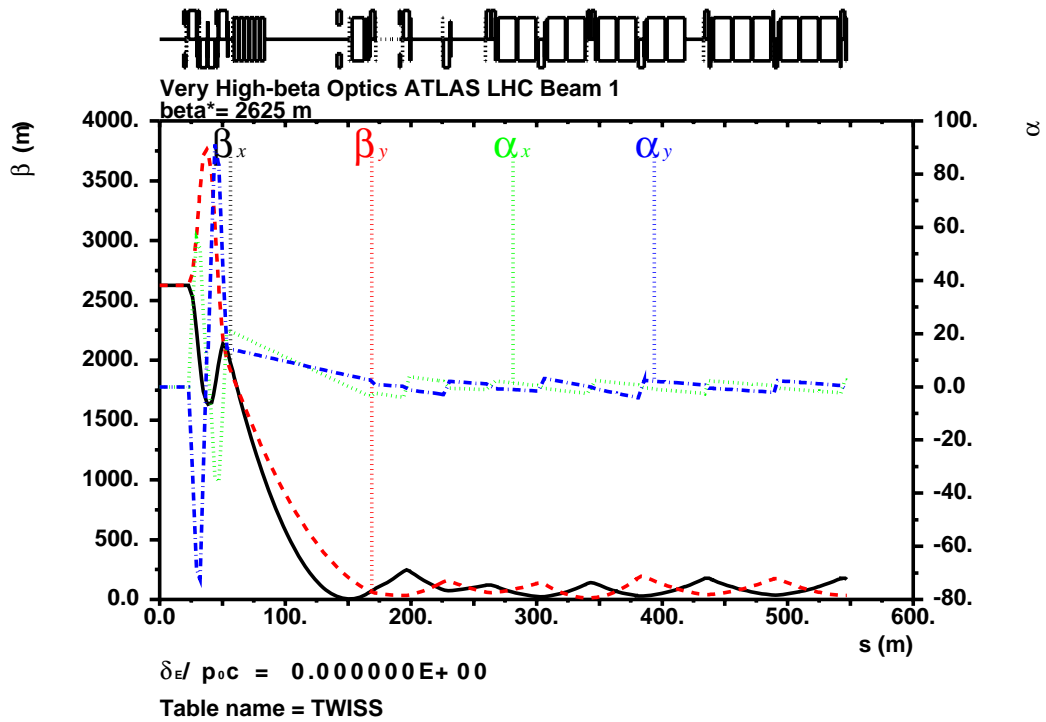


Figure 3-2 Optical functions for the high β^* optics, LHC optics version 6.5.

Table 3-1 The beam parameters for the proposed high beta* optics. The beam parameters have been calculated using a normalized transversal emittance of $1 \mu\text{m rad}$, and with the detectors located between Q6 and Q7 at 237.4 m (RP1) resp. 241.5 m (RP2) from the IP.

Interaction Point			Vertical Measurement - Detector between Q6 and Q7			
Parameter	Value	Units	Parameter	RP1	RP2	Units
ε_N	1.0	$\mu\text{m rad}$	β_y	127.1	112.5	m
β^*	2625.0	m	β_x	81.0	86.7	m
α^*	0.0		σ_y	135	113	μm
D_x^*	0.0	m	σ_x	108	127	μm
$D_x'^*$	0.0		σ_y'	2.23	2.23	μrad
σ^*	0.612	mm	σ_x'	1.72	1.72	μrad
σ'^*	0.233	μrad	$\Delta\mu_y$	0.247	0.252	2π
			$\Delta\mu_x$	0.545	0.553	2π
			$M_{y,11}$	0.004	-0.003	
			$M_{x,11}$	-0.169	-0.172	
			$M_{y,12}(L_{eff,y})$	577.5	543.4	m
			$M_{x,12}(L_{eff,x})$	-130.0	-156.7	m

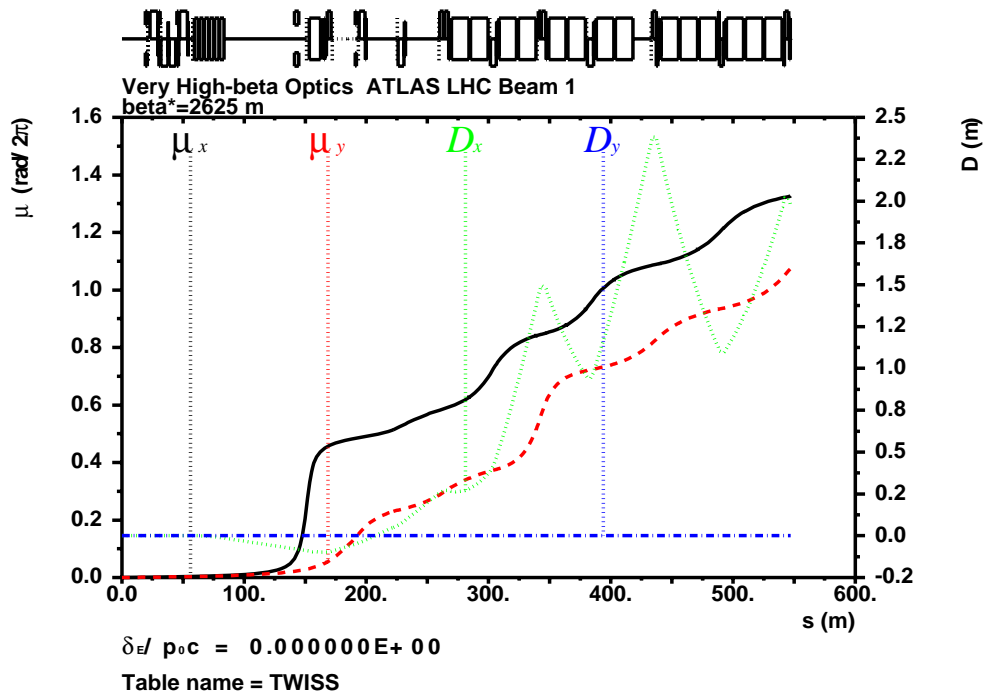


Figure 3-3 Phase advance and dispersion for the high β^* optics in Ring 1 around IP1, LHC optics version 6.5.

3.3 Injection and transition optics

Due to the aperture limitation, the injection requires a special optics. The nominal injection optics for low beta running cannot be used by TOTEM and ATLAS because the total phase advance over the insertion is different relative to the nominal low beta optics. A new injection optics has been found, keeping the same powering constraints for the trim power supplies and keeping the reversed polarity for Q4. A solution for the injection optics with β^* of 200 meters is shown in Figure 3-4.

It is also necessary to have a continuous transition between the injection optics and the collision optics keeping within the same powering constraints. As an example the transition optics is shown in Figure 3-5 for the case of a β^* of 1500 meters.

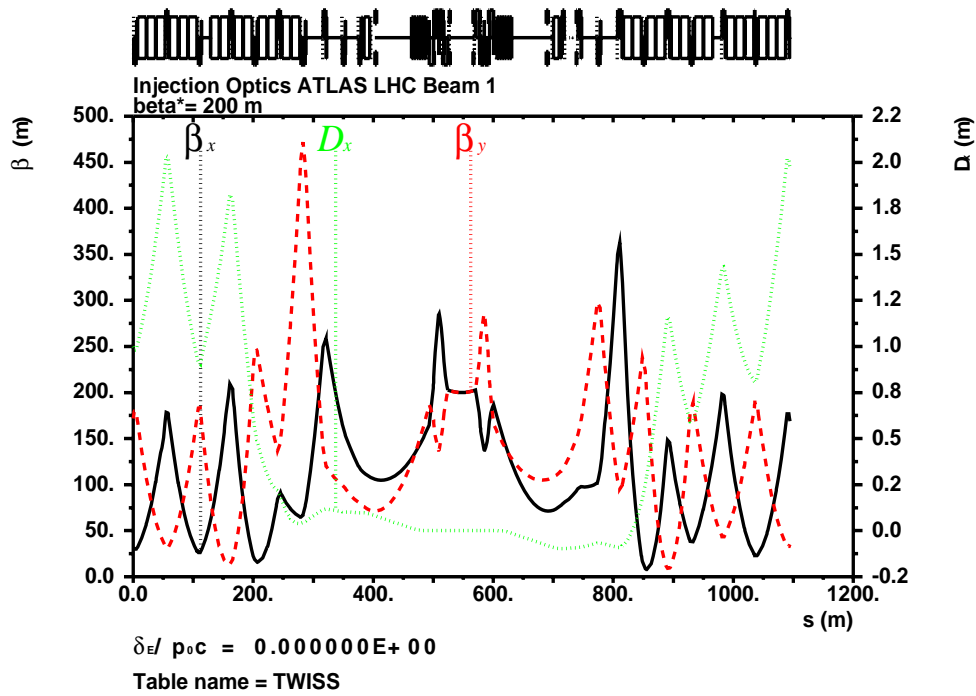


Figure 3-4 Injection optics with $\beta^* = 200$ m in Ring 1 around IP1, LHC optics version 6.5.

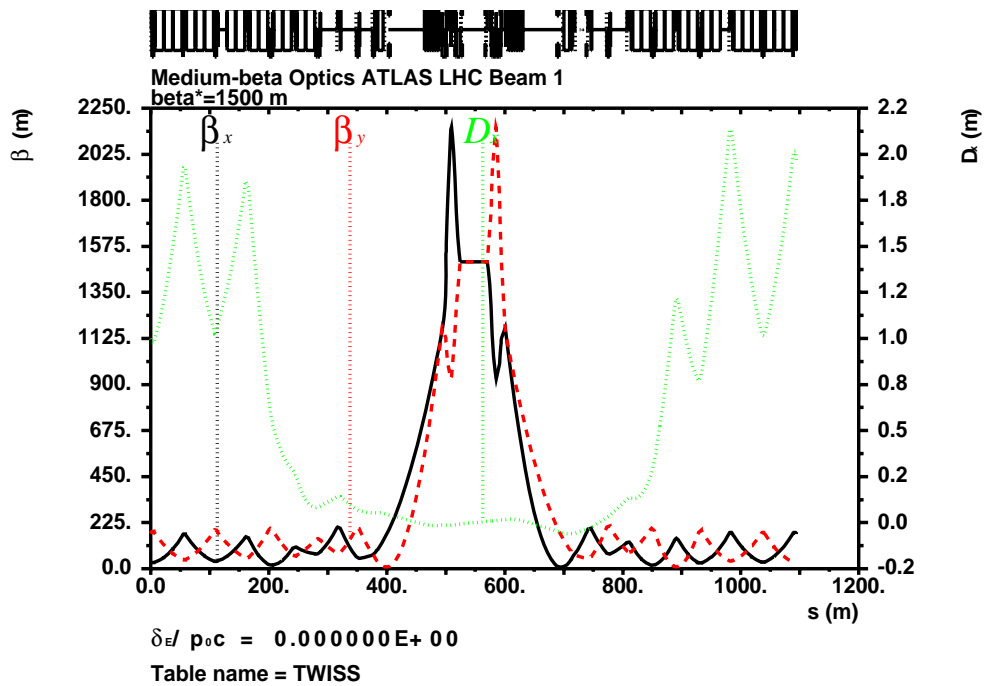


Figure 3-5 Medium beta optics for $\beta^* = 1500$ m in Ring 1 around IP1, LHC optics version 6.5.

3.4 Beam emittance

From Equation 3-10 we saw that t_{min} is directly proportional to the emittance. As discussed above this is true when the closest approach to the beam is determined by the beam halo. If on the other hand the limitation is given by closed orbit instabilities, the minimum distance will be an absolute number independent of the beam size and t_{min} will be proportional to $1/(\beta^*\beta)$ and thus independent of the emittance. This explains the schematic behaviour seen in Figure 3-6 which shows t_{min} as a function of the normalized emittance ϵ_N .

It is assumed that the beam halo limit is reached at $15 \sigma_{beam}$ and that the closed orbit limit is at 1.5 mm. It can be seen that for values of ϵ_N below 1.0 $\mu\text{m rad}$ the reachable t_{min} remains constant.

A normalized transverse emittance of 1.0 $\mu\text{m rad}$ is probably within reach. Actually this is the design value for the so called commissioning emittance in the LHC conceptual design report [3-5]. There are positive results from machine development sessions in the SPS [3-6]. Emittances of 0.9 $\mu\text{m rad}$ in the horizontal plane and 1.1 $\mu\text{m rad}$ in the vertical plane have been reached, for 7×10^{10} protons per bunch and emittances as small as 0.6-0.7 $\mu\text{m rad}$ has been obtained in both planes for a bunch intensity of 0.5×10^{10} protons per bunch. Thus at a bunch intensity of a few 10^{10} protons a transverse emittance of about 1.0 $\mu\text{m rad}$ seems feasible in the SPS. The SPS is equipped with fast scrapers, designed to remove any halo beyond 3 - 3.5 sigma in the SPS before injection into the LHC. For the smaller intensities relevant for high beta operation, the scraping in the SPS could be made much tighter [3-7]. Of course, a small emittance in the SPS is not a guarantee that the small emittance will be preserved during the transfer to LHC. This will depend on the extent to which the injection errors can be controlled. At the LHC energies, damping from synchrotron radiation should just become noticeable and will help to reduce any emittance growth.

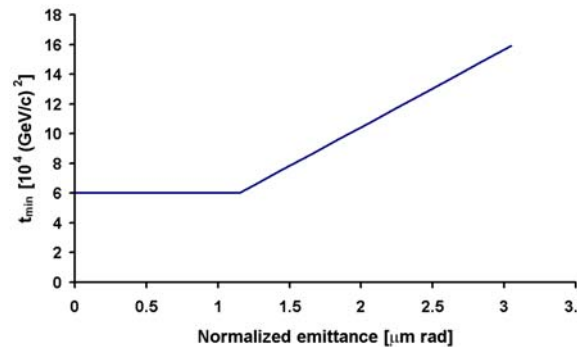


Figure 3-6 t_{min} reach as a function of the normalized emittance ϵ_N . t_{min} increases linearly with the emittance. However at very small emittances, closed orbit instabilities determine the reachable t_{min} .

3.5 Collimation and beam halo

3.5.1 Collimation

The LHC requires a powerful collimation system to protect the machine and to avoid quenches. The concept is based on a set of adjustable primary and secondary collimators [3-8]. For a given setting of the collimators, a certain population of secondary and tertiary halo is created. An example is given in Figure 3-7 corresponding to the primary collimator set at 6σ from the beam and the secondary collimator at 7σ .

We can see from Figure 3-7 that at amplitudes beyond 10σ we are in the shadow of the primary collimators and protected against the secondary halo. In principle the Roman Pot detectors can thus approach as close as 10σ to the beam provided the primary collimators are set at 6σ from the beam. Such small collimator opening will not be without problems for a low emittance beam due to impedance issues. It has been decided to use a low-Z material like graphite instead of copper for the construction of the collimator jaws. This decision is dictated by the required robustness against accidental beam losses on the jaws. The drawback with a low-Z material is an increase in the collimator impedance compared to high-Z material. The increased impedance might generate resistive-wall instabilities of the beam if the collimators openings are too small. These instabilities depend on the bunch intensity (N_p), the normalized transverse emittance (ε_N) and the collimator gap (n_g expressed in σ_{beam}). Stability limits have been calculated in [3-10] and stable conditions with a 10% safety margin are obtained for $N_p = 3 \times 10^{10}$ protons per bunch, $\varepsilon_N = 1.2 \mu\text{m rad}$ and $n_g = 10.6$. It turns out that the limit scales as:

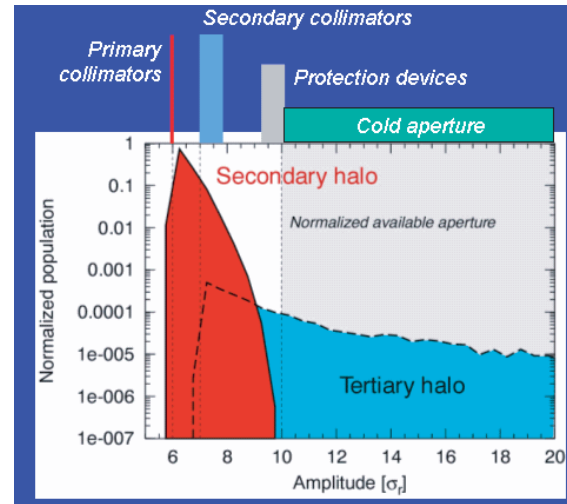


Figure 3-7 Normalized halo population as a function of particle amplitude in units of the beam r.m.s. width. The primary collimators are set at 6σ and the secondary collimators at 7σ [3-9].

$$\frac{N_p}{n_g^3 \cdot \varepsilon_N^{5/2}} \quad 3-12$$

Applying the scaling law, we see that for $N_p = 10^{10}$ protons/bunch and $n_g = 6$, the smallest possible emittance, still giving stable beam, is $1.5 \mu\text{m rad}$. Thus, if we want to maintain the primary collimators at 6σ we can not work with the desired $1 \mu\text{m rad}$ beam emittance. However the loss of a factor 1.5 in t_{min} generated by the bigger emittance can be compensated if we manage to locate the detector as close as 12σ to the beam. An emittance of $1.5 \mu\text{m rad}$ and a distance from the beam of 12σ gives the canonical $t_{min} = 0.0006 \text{ GeV}^2$ for $\beta^* = 2600$ meters.

It should be pointed out that the scaling law given above applies to a multi bunch instability and can be considered as conservative for high beta operation using few bunches at large distances. It is also true that when collimators are brought very close to the beam, wakefields become nonlinear which again results in more favorable scaling than the $1/n_g^3$ given in the estimate.

It is clear that the collimation will be a very critical issue in any attempt to reach the Coulomb interference region. It is also clear that it is difficult to predict the most favourable set of parameters in terms of values of N_p , n_g , ε_N and distance of the detectors from the beam. The best parameter space will in the end be determined during extensive beam tuning sessions. The considerations here indicate that the required t_{min} is within reach but that the task is very challenging and that the uncertainties are such that no guarantees can be given.

The impedance problem of the collimators discussed above will be of less importance after a couple of years of LHC operation. In a phase 2, it is planned to install new hybrid collimator jaws with additional metallic components.

3.5.2 Beam halo

A dedicated study was carried out to try to estimate the level of the beam halo [3-11]. We describe here briefly the method employed and the results. Later, in Section 9, we will use these estimates to investigate how the beam halo influences our measurement of elastic scattering.

Three sources of beam halo have been considered separately.

1. *Halo particles originating from inefficiencies of the betatron collimation system.* The betatron collimation system is located at IR7 and consists of primary collimators, secondary collimators and additional absorbers. It is designed to reduce the halo that derives from the slowly increasing amplitudes of the betatronic motion. The baseline setting of those collimators has been used in the simulation (primary collimators at 6σ , secondary collimators at 7σ and additional absorbers at 10σ ; σ refers to the beam σ at the position of the collimator)
2. *Halo particles from inefficiencies of the momentum collimation system.* The momentum collimation system is located at IR3 and like the betatron collimation system it consists of primary collimators, secondary collimators and additional absorbers. The off-momentum protons with relatively small betatronic amplitudes cannot be intercepted by the betatron collimation system. They can be lost in the arcs and dispersion suppressors where the horizontal dispersion function is large. To prevent such a losses the horizontal dispersion at the location of the primary momentum collimator must be larger than in the arcs. The baseline settings of the momentum collimators and additional absorbers are: 15σ for the primary collimators, 18σ for the secondary collimators, 20σ for the horizontal absorbers and 10σ for the vertical absorber. These positions are given for the standard normalized emittance of $\varepsilon_N = 3.75\ \mu\text{mrad}$. For a reduced emittance, these positions are too close to the orbit. For a normalized emittance of $\varepsilon_N = 1\ \mu\text{mrad}$ the positions that are approximately equivalent to the baseline settings are 21σ for the primary collimators, 25σ for the secondary collimators and 28σ for the horizontal absorber. The vertical absorber can be kept at 10σ . An aperture of the vertical absorbers as small as possible is highly desirable because these absorbers are the sole objects limiting the vertical tertiary halo produced by the momentum collimators. In the simulation we used a normalized emittance of $\varepsilon_N = 1\ \mu\text{mrad}$ and the wider collimator settings mentioned above
3. *Halo particles from elastic and quasi elastic scattering of the beam protons on the nuclei of the residual gas.* The scattering increase the amplitude and is thus another source of halo particles. Gas pressure in the arcs and dispersion suppressors is generally higher than in the long straight sections and the overall length of the long straight sections is only 15% of the entire length of the machine. Therefore the main source of this type of the halo should come from the residual gas in the arcs and dispersion suppressors. The local beam gas background from the long straight sections has nevertheless been estimated [3-12] and it confirms that this source is considerably smaller than the one coming from the arcs

The recent version (2005) of the STRUCT code [3-13] has been used to simulate all three types of halo. The LHC high β^* optics V6.5 of the entire machine for Beam1 was used as the input for the simulations. The goal of the simulation was to record every crossing of protons in a transverse plane at the position of the Roman Pots.

Betatron cleaning and momentum cleaning are simulated separately but the simulations are similar. The simulation starts from the impact of the primary halo proton at one of the primary collimators. The turn by turn tracking is being done until the proton is absorbed in one of the collimator jaws or reaches the limiting aperture of one of the other elements of the machine. The simulation of the beam-gas scattering in the arcs and dispersion suppressors starts from the simulation of the beam proton at some initial point. The coordinates and the angles are simulated from a 2-D Gaussians. The path length to the beam-gas interaction is selected randomly from uniform distribution and the proton beam is tracked to the point of interaction. The residual gas is assumed to be pure hydrogen. Only elastic scattering and single diffraction with the energy loss less than 1.1% are simulated. The rest of the total cross-section is considered as leading to loss of the protons. The scattered proton is tracked until it is lost in the collimators or at the limiting apertures.

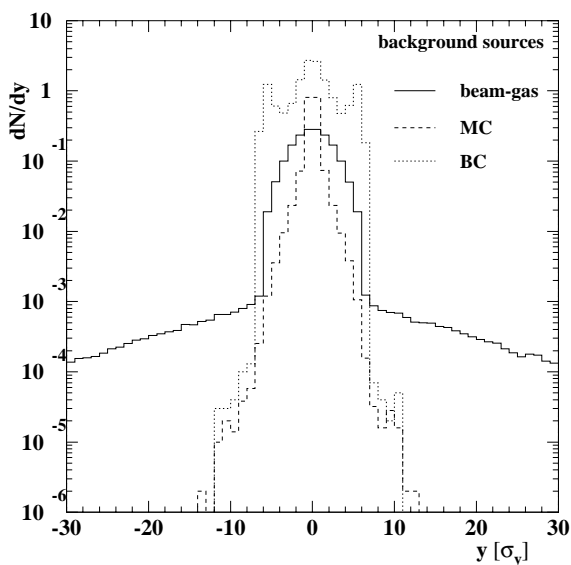


Figure 3-8 Distribution of vertical impacts of halo protons for different background sources.

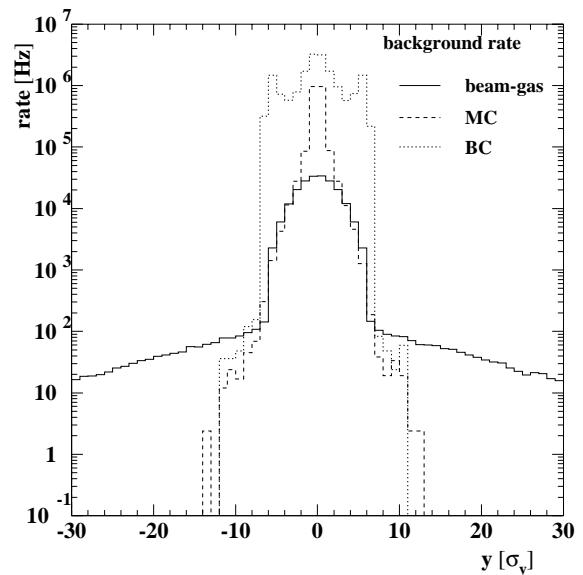


Figure 3-9 Single background rate for different background sources.

The vertical distributions of hits are shown in Figure 3-8. The distribution for betatron collimation and momentum collimation are normalized per proton impacting on the primary collimators. The distribution for the beam-gas is normalized per proton interaction with the residual gas in the arcs and dispersion suppressors. In order to relate the result of Figure 3-8 to number of halo particles/time unit we have to make assumptions about the number of particles present in the LHC ring at the start of the fill and assumptions about the beam lifetime from the different loss mechanisms. We have assumed that the number of particles is given by 43 bunches with each 10^{10} particles. For the losses of particle on the betatron collimators and on the momentum collimators we have in both cases assumed a beam lifetime of 100 hours. In the case of losses due to beam gas we have assumed a lifetime of 1000 hours. This is 10 times longer than the nominal 100 hours for collision optics. The nominal beam lifetime of 100 hours is based upon estimates of the dynamic pressure expected at full beam intensity in the LHC. With only 43 bunches and 10^{10} particles per bunch the pressure will be close to the static pressure and thus assuming a beam lifetime of 1000 hours is not overoptimistic [3-14]. Figure 3-9 gives the single halo rates R_s with the above assumptions, according to:

$$R_s = N \times \frac{k_{bunch} \cdot k_{part}}{\tau} \quad 3-13$$

where N is the number of halo particules as determined in Figure 3-8, k_{bunch} is the number of bunches, k_{part} the number of particules per bunch and τ is the beam lifetime.

The contributions from betatron and momentum collimation are negligible above 10σ . On the other hand we see an integrated rate of 2000 halo particles /second above 10σ from beam gas scattering. The halo rates of Figure 3-8 are used as input to the background simulation that will be discussed in Section 9.3.4.2. Most of the halo can be rejected by means of vertex and acolinearity cuts as will be discussed in Section 9.3.4.

3.6 Luminosity and bunch structure

The elastic cross section is huge compared to the typical cross section of interest at the LHC. Our simulations (see Chapter 9) show that if we do not want to be limited by statistics we need to collect about 10^6 events in our t range. This can be achieved in about a week for a luminosity of $10^{27} \text{ cm}^{-2}\text{s}^{-1}$, given the acceptance estimated in Chapter 9 and with some reasonable assumptions about the running efficiency. The reduction from the nominal luminosity of $10^{34} \text{ cm}^{-2}\text{s}^{-1}$ to $10^{27} \text{ cm}^{-2}\text{s}^{-1}$ is done by several different factors.

A factor of ~ 1000 is automatic from the high β^* -value. A further reduction of ~ 100 can be achieved by operating with only 43 bunches instead of 2800. This fits well a filling scheme from the PS using only one bunch per batch from the PS. There is a two fold advantage in operating with so few bunches. Firstly, there is no need for neither a crossing angle nor a vertical offset because the bunches are separated in such a way that there will be no additional collisions away from the Interaction Point. Secondly, the space between bunches is roughly $2.1 \mu\text{s}$ or 630 meters, and thus there will be no confusion in the timing between incoming and outgoing bunches at the Roman Pot stations situated a couple of 100 meters away from the Interaction Point. The β^* and the bunch number reduction gives a factor 10^5 . A further factor 100 in the reduction of luminosity originates from the fact that we will operate with 10^{10} protons per bunch rather than 10^{11} protons per bunch.

3.7 Determination of beam parameters

An accurate measurement of the luminosity and the total cross section requires an excellent knowledge of the machine parameters in the straight section of the LHC around ATLAS. The aim is to obtain:

- $\beta^*(x,y) = 2630 \text{ m} \pm 1\%$
- β at Roman Pots between Q6 and Q7 to $\pm 2\%$
- phase advance at Roman Pots to $\pm 0.5^\circ$
- beam divergence at the Interaction Point to $\pm 10\%$
- crossing angle between beams $0 \pm 0.2 \mu\text{rad}$

This is rather demanding and will require dedicated machine set-up and measurement time. Phase advance and β can be measured by exciting beam oscillations and with multi-turn beam position monitoring. In addition, the β^* values can be determined from the tune shift induced by strength variation of the

insertion quadrupoles. A change of the quadrupole gradient Δ_{KI} of a quadrupole at the position where the beta function equals β_Q will result in a tune shift of:

$$\Delta_Q = \frac{\Delta_{KI} \cdot \beta_Q}{4\pi} \quad 3-14$$

The sensitivity increases with β and should allow for a very good sensitivity and accuracy in the determination of β^* . We can expect, that the beam divergence can be calculated from measurements of beam size and the knowledge of the β function around the machine to the required accuracy.

The high β operation will be done for nominally zero crossing angle. The requirement to be able to detect any residual crossing angle at the level of $0.2 \mu\text{rad}$ is particular challenging, and may require extra or modified hardware. Directional strip line detectors will be installed on both sides of the Interaction Point close to Q1 at about 21 m from the Interaction Point. The precision to detect differences in beam position between beam 1 and beam 2 is expected to be limited to about $50 \mu\text{m}$ with the strip line detectors. Following discussion with our colleagues from the beam instrumentation group [3-15], we propose to add button pickups next to the strip line monitors using identical electronics for beam 1 and beam 2. For operation without crossing angle and the large bunch spacing proposed for the high beta operation, differences between the two beams should be measurable to about $10 \mu\text{m}$. This would allow to measure angles between the beams at the Interaction Point to $\Delta\theta = 0.5 \mu\text{rad}$ on either side. The measurements on each side can be combined to reduce the uncertainty to $0.35 \mu\text{rad}$. However, as can be seen later in Chapter 9 (Table 9-3), the precision required on the uncertainty on the crossing angle can be somewhat released without any significant impact on the total error.

3.8 References

- 3-1 TOTEM Collaboration, “*Total Cross Section, Elastic Scattering and Diffraction Dissociation at the LHC*”, Technical Proposal, CERN/LHCC 99-7 (1999).
- 3-2 A. Faus-Golfe and A. Verdier, “*Optics studies for diffractive physics at the LHC*”, EPAC 2002 proceedings.
- 3-3 A. Faus-Golfe, “*Optimized β^* insertion optics for the TOTEM experiment in IR1 and IR5 for Ring1 and Ring2 of the LHC version 6.0*”, LHC-Project-Note-207 (1999).
- 3-4 A. Faus-Golfe, M. Haguenaer and J. Velasco, “*Luminosity determination using Coulomb scattering at the LHC*”, EPAC 2002 proceedings.
- 3-5 LHC Conceptional Design Report, CERN/AC/95-05.
- 3-6 G. Arduini, private communication.
- 3-7 H. Burkhardt and R. Schmidt, “*Intensity and luminosity after beam scraping*”, CERN-AB-Note-2004-054 (ABP).
- 3-8 R. Assman et. al. , “*Design and building a collimation system for the high intensity LHC beams*”, PAC 2003 proceedings.
- 3-9 R. Assman, “*Collimation and cleaning*”, LHC Performance workshop, Chamonix XII, 2002.
- 3-10 E. Metral and A. Verdier, “*Emittance limitations due to collective effects for TOTEM beams*”, LHC-PROJECT-Note-345 (2004).
- 3-11 I. Bayshev, private communication.
- 3-12 I. Azhgirey, private communication.

- 3-13 I. Bayshev, A. Drozhdin and N. Mokhov, SSCL-MAN-0034, Dallas, March 1994.
- 3-14 A. Rossi, private communication.
- 3-15 R. Jones, private communication.

4 The Roman Pot mechanics and installation

4.1 Introduction

The Roman Pot technique has been successfully used in the past for measurements very close to the circulating beams in a number of experiments at different accelerators, as mentioned in the Introduction. The same technique will be used at LHC by TOTEM [4-1] and ATLAS. M. Oriunno from TOTEM has adapted the Roman Pot design to respect the requirements and the constraints of LHC. The ATLAS Roman Pot design has been derived from the TOTEM design and adapted to the ATLAS constraints.

The Roman Pots have been designed to approach the tracking detectors (scintillating fibre-based) at about 10σ (i.e. $\sim 1\text{ mm}$) from the circulating beams. A sketch of the Roman Pot concept can be seen in Figure 4-1, where the retracted position and the working position are shown. The working position will bring the bottom surface of a pot to a minimal distance of 10σ from the beam. The positioning of the pot will have to be agreed with the LHC and can only happen when the pots are in the shadow of an upstream collimator and during the dedicated high β^* runs (see Section 3.5).

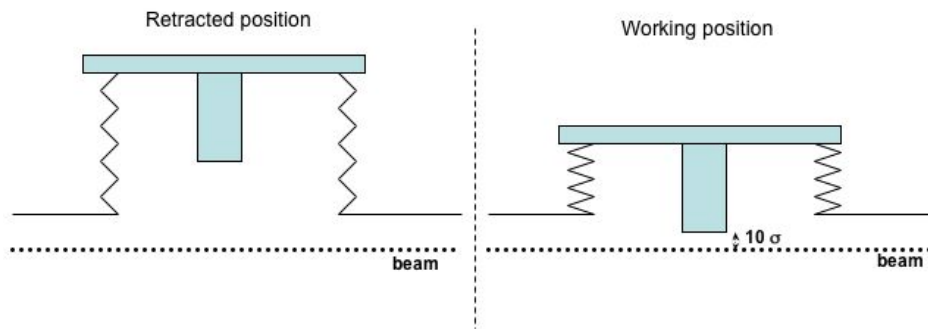


Figure 4-1 Roman Pot concept: on the left the retracted position is shown where the Pot is placed out from the beam; on the right in working position, the Pot is approached up to 10σ from the coasting beam.

The Roman Pots will be located at about 240 m from the ATLAS Interaction Point on both sides. The chosen position between the sixth and seventh quadrupole is shown in the schematic layout given in Figure 4-2.

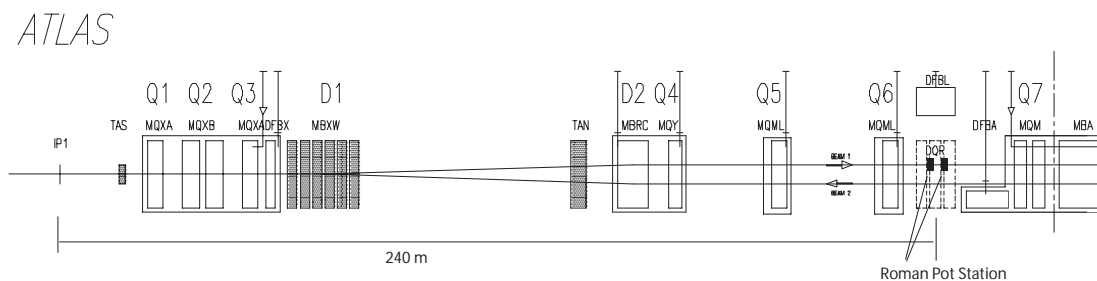


Figure 4-2 Schematic layout of the LSS1 near ATLAS with the proposed location of the Roman Pot station (one side).

We call the device that allow the independent movement of the top and bottom pots a Roman Pot unit. There will be two Roman Pot units separated by a distance of 4 m at each side of the interaction point. The complete system thus comprises in total 4 separate measuring stations and a total of 8 pots. The space for the Roman Pot units are limited by dump resistor boxes (DQR's) that are necessary for dumping the current of the main magnets in case of quenches. There will be two DQR's on each side of a Roman pot unit (Figure 4-3). The DQRs and their cables impose constraints on the available space as well as on the electrical environment. The impact on the installation will be discussed later in this chapter. In order to have enough protection from possible discharges, protecting elements in plexiglas, placed in proximity of the DQR connectors, are being included in the design of the Roman Pot Units (Figure 4-4).

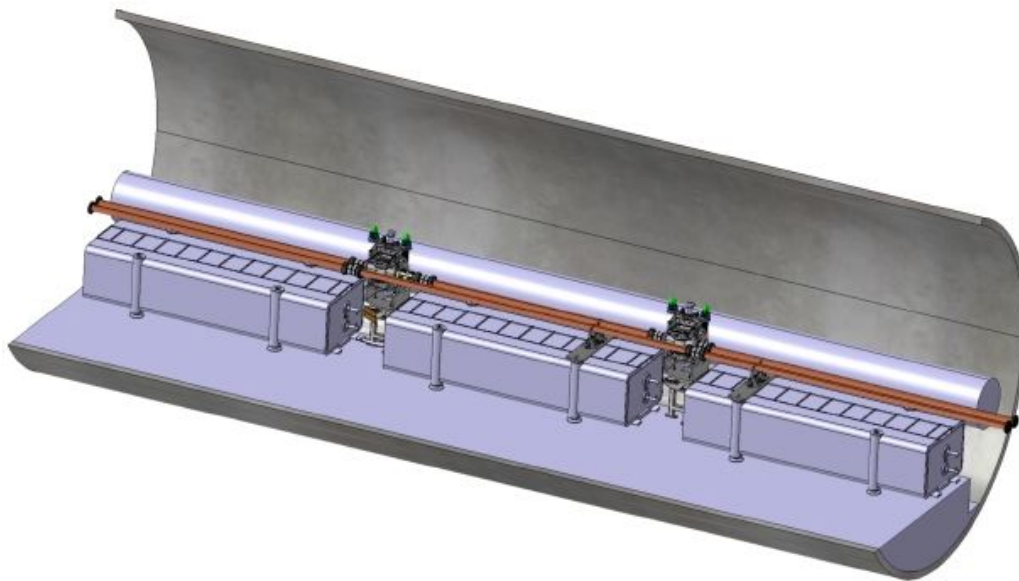


Figure 4-3 3D view of the Roman Pot Station on one side of IP1.

4.2 Roman Pot mechanics

The Roman Pots have been designed to satisfy both the strict requirements in terms of positioning precision of the detector and to also satisfy the constraints of the LHC accelerator. In order to guarantee long beam life time, all equipments placed in LHC have to be Ultra High Vacuum (UVH) equipments. The detectors and the read-out electronics have to be physically separated from the LHC primary vacuum, while ensuring the closest possible approach of the detector to the beam. For this reason the Pots will have a thin window (0.15 mm) on the section parallel to the beam, as well as thinner walls (0.5 mm) on the section perpendicular to the beam. The thin window will allow to place the detectors at a distance of about 1 mm from the beam and minimize the amount of material in front of the detector.

4.2.1 Roman Pot unit

The Roman Pot unit will allow the independent moving of the top and bottom pot to the nominal position via a high precision roller screw moved by a step motor. In order to guarantee the uniformity among all the moving elements installed in the LHC ring, the screws, the motors and the positioning sensors are those developed by the LHC Collimators group.

Each unit is composed of a main body ensuring the needed stiffness of the system, and two sets of movable arms, each able to ensure the precise vertical movement of the two pots. A 3D view of a Roman Pot unit is shown in Figure 4-4.

The pots are mounted on bellows that allow an excursion of 58 mm for the positioning around the coasting beam. The two bellows are part of the main vacuum chamber that is directly connected to one of the two LHC vacuum beam pipes. The vacuum chamber is connected via a small diameter pipe to a compensation system (Figure 4-5). Due to the LHC primary vacuum the two pots of each unit will be pulled into the main vacuum chamber with a force of about 2.7 kN. In addition the gravity force due to the movable parts weight and the detector and read-out weights, will add a component of the forces for the top pot and subtract it for the bottom pot. In order to ensure a smooth running to require less effort from the motors and to allow a retraction force, a symmetric compensation system is used to contrast all the forces. The compensation system, illustrated in Figure 4-5, consists of an interconnected vacuum chamber with two bellows of a diameter larger than the main vacuum chamber ones. They allow to have an over compensating force of about 3.6 kN that allows to compensate the contrasting vacuum force, the gravity and the residual torque of the motors, to achieve a moderate auto-retractive action.

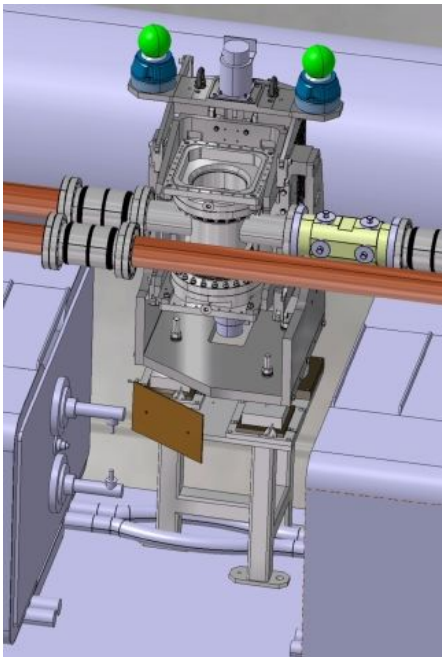


Figure 4-4 A Roman Pot Unit (3D view). It is possible to see the support and the specific shape of the base plate to have enough clearance from the DQR connectors and cables. In addition a protective plexiglas foil is added on the support in proximity of the DQR connectors, to ensure higher level of insulation. On the right the position of a BPM is shown.

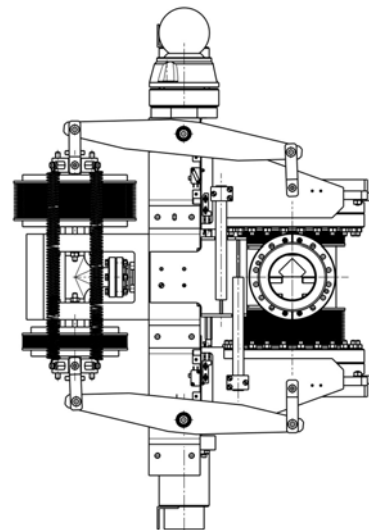


Figure 4-5 Roman Pot Unit design. On the right the top Pot is completely in the vacuum chamber, while the bottom is in retracted position. On the left one can see the Compensation System.

The coarse positioning will be done by reading the nominal beam position given by the LHC Beam Position Monitors (BPMs) located on one side of the Roman Pot Units and connected to it via a vacuum flange. The fine positioning will be done by equalizing the counts in top and bottom detectors. The precision of the coarse positioning will be determined by the reading of the Linear Variable Displacement Transducers (LVDTs) position sensors mounted on each Unit. The ultimate relative position of the two pots will be determined with high precision by the overlap detectors (see Section 5.2.3).

4.2.2 The Pot

The interior of the Pot will be in a secondary vacuum to minimize the deformation induced by the LHC primary vacuum on the bottom window of each Pot. The Pot will house the detector and therefore its design had to take into account the constraints imposed by the tracking detector as well as the compatibility with the movement system and the rest of the Roman Pot Unit.

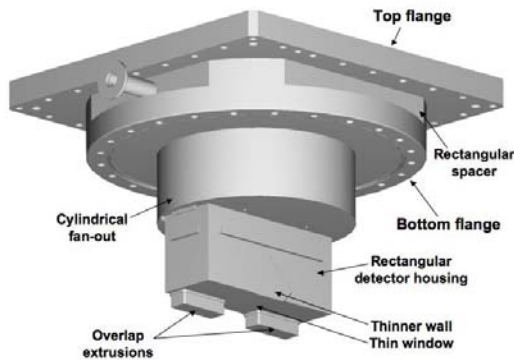


Figure 4-6 3D view of the outside of the Pot. It is possible to see the various shapes as described in the text, and the small vacuum inlet for the secondary vacuum pumping.

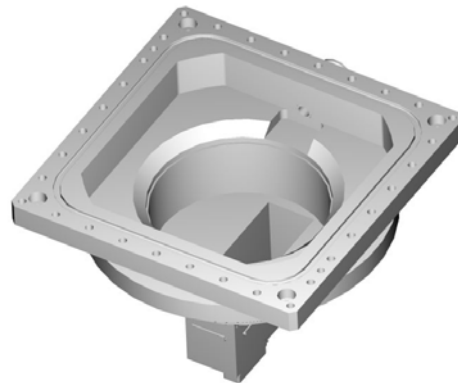


Figure 4-7 Interior 3D view of the Pot. It is possible to see the fan-out space for the fibre routing and the rectangular section of the fibre detector housing.

The main purpose of the Pot is to approach the detector as close as possible to the coasting beam respecting the limit of 10σ . For this reason the bottom of the Pot, in the region where the detector is placed (28 mm around the center) is cut and a thin window is placed to cover the aperture. The thickness of the Pot walls is of 2 mm, while the thin window is only 150 μm thick. That allows to minimize the distance between the beam and the detector. Furthermore it is also important to reduce the thickness of the Pot walls in the direction perpendicular to the beam. In the past there was the plan to have a thin window also on the side walls to reduce that thickness, but the difficulty of the realization and the risks for the vacuum tightness, suggested instead the machining of the side walls down to a thickness of 500 μm .

The thin window has been object of a long R&D phase for TOTEM carried out by S. Mathot from the TS department. The requirement for the thin window is to be able to stand a pressure of 1.5 times the atmospheric pressure. In order to assess the limit of this technique, tests have been done to reach the situation where the window is destroyed by the pressure difference. The thin window did not break up to a pressure of 83 bar. Further measurements will be done for the ATLAS Pot, that are currently under development to be finally produced in Spring-Summer 2008.

The ATLAS Pot has few important aspects that make it different from the ones used in other experiments:

- The upper part is composed by two flanges decoupled by a rectangular spacer that allows the mounting on the Roman Pot Unit mechanics from the front. In other experiments the Pot insertion is done from the top, but for the ATLAS bottom Pot there is not enough space between the Pot support and the base of the Unit. The bottom flange will be connected to the bellow of the main vacuum chamber, ensuring the primary vacuum tightness. The top flange will connect to the supports

for the photomultipliers and the rest of the electronics and will allow the tightness of the secondary vacuum.

- Between the Pot upper part and the straight rectangular bottom where the detector is housed, there is a cylindrical section. The cylindrical section allows the correct fan-out for the fibres routing that can follow smooth angles and avoid damages to the fibres
- The bottom rectangular part has also two rectangular small extrusions with a dimension of $42 \times 12.5 \times 15 \text{ mm}^3$. These extrusions will house the two overlap detectors (see Section 5.2.3).

Because of these specific features there are several constraints on the dimensions of the Pots. The dimension of the straight rectangular bottom section have to allow the housing of (see Section 5.2.3):

- 10 plates allowing the mounting of the two U-V fibre detector planes
- One 3 mm trigger scintillator to be placed in front of the detector planes
- Three plates for the overlap detectors and one small scintillator in front of the overlap detectors on both sides of each pot, all contained in the two extrusions of the pot (Figure 4-8)
- Three small size photomultipliers for the read-out of the three trigger scintillators.

In order to be able to allow the proper positioning for the bottom and top overlap detectors, the rectangular part has to be mounted off center (see Figure 4-8). Therefore another constraint is coming from the surrounding bellow that limits the possible transverse dimensions of the bottom rectangular section: due to its non-central position, the larger side of the rectangular bottom part has to have a dimension lower than the diameter of the bellow to keep a safe clearance from the bellow surface, allowing safe movements and installation. Taking into account all these constraints the dimensions of the rectangular section have been fixed at width x height x thickness = $128 \times 60 \times 46 \text{ mm}^3$.

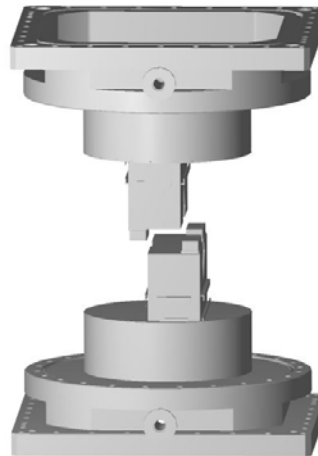


Figure 4-8 3d view of the two vertical Pots to illustrate the overlap concept.

The Pot height outside the main vacuum chamber limits the available space for the handling and for the mounting of the electronics. A careful analysis of the available space for the electronics has been carried out to derive the constraints on the dimension of the electronics. On top of the Pot flange there will be the plates for the mounting of the photomultipliers and on top for the front end boards. All front end boards are then connected via flex kapton cables to the motherboard. The space available allows the positioning

of the electronics on top of the Pot. The position of the electronics motherboards is currently under study to optimize the cable length and the access to all parts. A possible solution is shown in Figure 4-9.

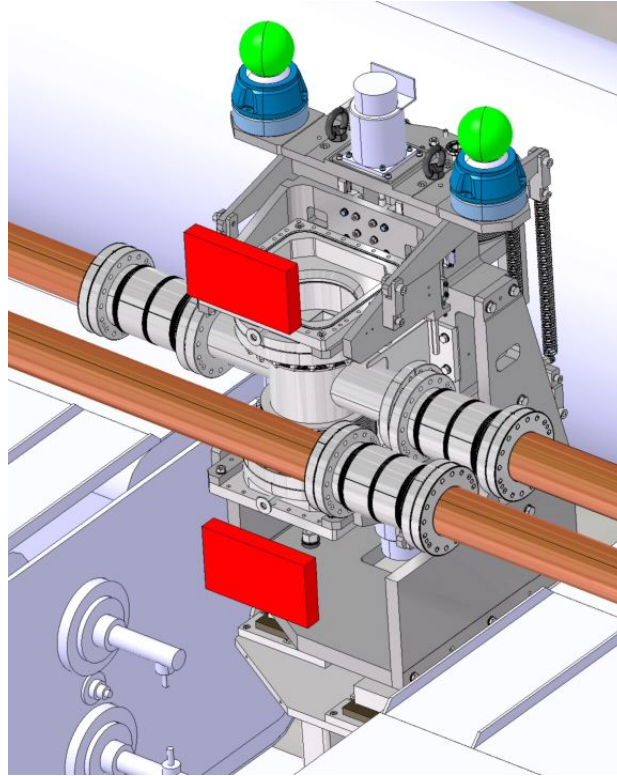


Figure 4-9 Study of available space for the motherboard.

4.3 RF impedance and coupling with LHC beams

4.3.1 Introduction

The insertion of the ATLAS Roman Pots will contribute to the total LHC coupling impedance budget. The Pot design must aim at minimizing the longitudinal and transverse impedances in order to avoid the generation of beam instabilities and power exchange between the particles and the Pot walls.

In general the impact of any accelerator element on the impedance is determined by:

- a resistive wall effect, enhanced as the beam approaches the surrounding materials and when low electrical conductivity materials are used;
- a geometrical effect, generated by any abrupt change of the beam pipe cross section.

At the LHC the resistive wall impedance will be dominated by the collimator system and the contribution of the ATLAS Roman Pots will be negligible. On the other hand, the geometrical effect has to be carefully studied and a series of laboratory measurements has been launched.

4.3.2 Laboratory measurements

The technique based on the coaxial wire method is used. RF power injected along a thin wire stretched through the detector allows to excite a field similar to the one generated by an ultra relativistic point charge. Such a method allows to determine the complex longitudinal and transverse impedances that have to be coupled to the LHC beam spectrum in order to assess the effective impedance. In general, the frequency range of interest at LHC spans from the low frequencies (higher than 8 kHz), typical of the first betatron unstable resonances, to about 2.5 GHz, where the beam harmonic amplitudes are negligible even in case of very short bunches.

Two series of laboratory measurements have been completed; the data analysis is in progress and the preliminary results are reported here. The setup is based on a Vector Spectrum Analyzer (VNA) used as both an RF source and a signal analyzer. The complex transmission coefficient is measured connecting the two VNA ports to the wire stretched along the device under test, that is the Roman Pot Unit main chamber. Its comparison to the signal taken in the same way with a reference smooth beam pipe, allows the calculation of the longitudinal impedance (Z_L/n). The details for this measurement and the definitions of all the quantities involved can be found in [4-2], [4-3] and [4-4]. The stretched wire method has been applied to an ATLAS Roman Pot prototype while setting the pots at different locations, ranging from the retracted to the nominal operation positions. A second set of measurements has been taken after mounting some ferrite tiles on the pots walls, with the aim of absorbing the electromagnetic power at the observed resonances. We mounted semi-circular ferrites, designed for other uses, on the bottom of the cylindrical section, parallel to the beam direction. Preliminary results are shown in Figure 4-10, for the real and the imaginary part of the longitudinal impedance.

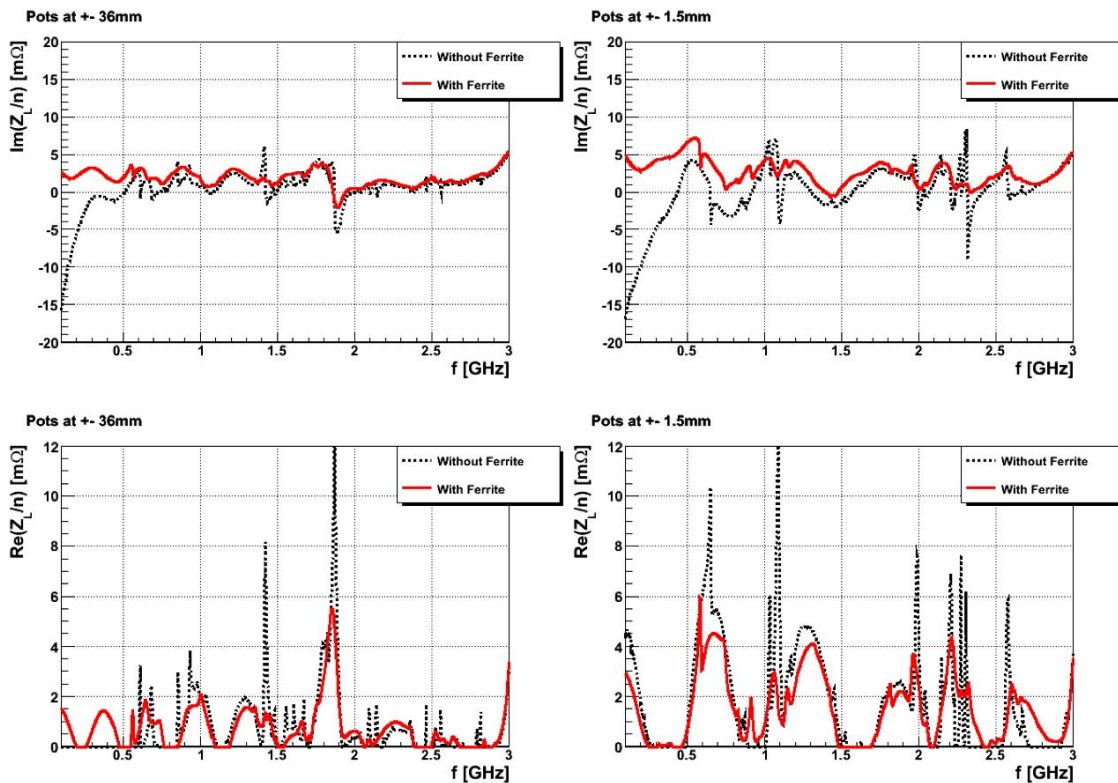


Figure 4-10 Top: Impedance imaginary part for retracted (left) and working position (right). Bottom: Impedance real part for retracted (left) and working position (right).

It must be remarked that the low frequency modulation of the signals (with period equal to about 600 MHz) is generated by multiple reflections of the injected wave that appear only due to the presence of the wire as a continuous conductor. Therefore it must be considered as a drawback of the measurement method and only the sharp resonant peaks must be considered in estimating the beam coupling impedance.

The measurements without ferrite tiles show a number of resonances spanning from about 600 MHz to about 2.5 GHz, in both the retracted and the operation pots positions. The resonance lines at 600 MHz and 1 GHz, at which the real part of the longitudinal impedance exceeds 10 m Ω , when the pots are in the operation position, are particularly worrying because they may couple to high beam harmonics.

After the installation of the ferrite absorbers, the resonance at 1 GHz is efficiently reduced to below 4 m Ω , as occurs for all lines at higher frequencies. Only the first line at about 600 MHz (with pots in operation position) remains above 5 m Ω . This small value can be further reduced adding more ferrite material. It should be noted that the dimensions of the ferrite tiles was considerably smaller than the available surface, because they were produced for a different application and used in the setup to have a first evaluation of the effects. Larger ferrite tiles will be mounted in production, to enhance their dumping effects.

More analysis is needed for the determination of the transverse impedance, calculated from the variation of the longitudinal one for different beam positions. The work in progress includes a series of numerical simulations aiming at benchmarking the laboratory measurements. A more complete and detailed report about the results and the simulation will be documented in an internal note [4-5].

4.4 Positioning system

The positioning system is composed of the motors, the rotary position sensors (resolvers) that are mounted on the motors, the longitudinal position sensors (LVDTs) and the control system. As mentioned in Section 4.2.1 we will use the equipment developed and selected by the LHC Collimation group [4-6]. Below we describe some of the main design criteria which are relevant for our application.

4.4.1 Motors

The motors are the ones selected for the LHC collimators. These are radiation hard step motors. On each motor there is a resolver, as rotary position sensor, allowing the read-out of the relative and absolute position.

The motors have been designed to have a residual torque of about 0.102 ± 0.02 Nm. The movable mechanism of the Roman Pot unit will be connected to the motors through a 2 mm pitch roller screw. The motors have an angle resolution of $(1.8^\circ \pm 0.1^\circ)$ in full step operation (200 steps/revolution). However the motors will be used in half step operation mode (400 steps/revolution) allowing a displacement of 5 μ m, that is the screw pitch divided by the number of steps for a revolution.

The expected torque load is about 0.3 Nm for the top pot and about 0.6 Nm for the bottom pot. The pull-out torque from the motors is of about 3.5 Nm to allow safety margin in the retraction of the Pot. The foreseen nominal speed is below 5 rps (revolutions per second). The motors are of 2-phase bipolar hybrid type to minimize the number of wires in the connection. No driving electronics is embedded in the motors to ensure their resistance to radiation. The motors are expected to comply to an integrated radiation dose of 30 MGray. They are expected to be operated at a temperature of 40 ± 20 °C. The selection of the motors imposed a constraint due to the expectation that they will be exposed to periodic bake-out of the me-

chanical assembly (carried out at about 150 °C). This requirement is much less stringent for our application. The expected lifetime of the motors is 15 million revolutions.

4.4.2 Rotary position sensors: resolvers

It is foreseen to measure the real angle movement on the motor axes and to use the motors with microstep drivers at 400 steps per revolution (a higher number of steps is possible). The angle resolution will be of the order of 1000 pulses per revolution. That would enable us to improve by a factor 2 the precision, if needed, by a different programming of the microstep drivers. However limitations to a real higher precision may come from the effective accuracy reachable by the mechanics and its assembly, making this possibility not usable.

Contactless resolvers have been selected as rotary position sensors due to their capability to withstand high integrated radiation dose. No conditioning electronics can be embedded in the sensor because of the high radiation resistance required (as for the motors the expectations are for an integrated radiation dose of 30 MGray). As for the motors, the expected lifetime is of 15 million revolutions.

The resolvers have two outputs: the sine and the cosine of the angle of rotation, that is easily calculated from the arctangent of the ratio. By counting the number of zero crossings one can establish the absolute position. However, given the accuracy and the size of the displacements, in normal operations the relative position is the most important and interesting quantity to be monitored and controlled.

4.4.3 Motor drivers

Microstep drivers have been chosen for the motor operations to allow the possibility of choosing the number of steps per revolution by modulating the supply current of the two motor phases. These drivers are powered from normal 220 V line plugs and are placed at a distance of about 300 m from the motors (in the experimental USA15 cavern).

Each motor driver is entirely and individually programmable through a standard industrial interface. The parameters to be programmed are:

- Number of steps/revolution: 200, 400, 800, 1600 or more (allowed by a complex modulation, but not needed for the reasons expressed in Section 4.4.2).
- Current: any level of current between 0% and 100% of the maximum current (2 A) can be set, with a resolution of at least 0.1 A.
- Remote software reset of the unit/individual drivers is possible in case of software failure, through a dedicated digital input

The full status of the driver will be available with appropriate asynchronous communication through the programming bus. A temperature sensor embedded on the driver board is installed to monitor the temperature on each driver to prevent faults.

4.4.4 Linear Variable Displacement Transducers (LVDTs)

The LVDTs are used to feedback the position of the Pot with respect to the beams circulating in the LHC. The transversal size of the proton beams will be of the order of 100 μm . The position of the Pots has to be determined with an accuracy that is a fraction of this size, of the order of $\pm 20 \mu\text{m}$. The ultimate relative

position of the two pots will be determined with high precision by the overlap detectors (see Section 5.2.3).

Since the Roman Pot mechanics will be exposed to a rather high dose of radioactivity, no electronics can be embedded in the sensor, nor placed in the proximity of the sensor. For this reason the distance between the sensor and the read-out electronics will be about 300 m.

LVDTs have been chosen for three reasons:

1. Their excitation at fixed frequency in conjunction with the ratiometric conditioning will offer the best solution with respect to immunity to EM noise over long distances.
2. The possibility to have a very high precision on a specific position by measuring the “zero” of the LVDTs will allow calibrating remotely the read-out electronics without accessing the radioactive zone.
3. By an accurate choice of the materials used the LVDT can easily be hardened to survive high levels of radiation.

The LVDT is contactless, in order to avoid problems of damage due to friction. The magnetic core is mounted on a sleeve screwed on a support. The LVDT has the form of a hollow cylinder and is fixed on the Roman Pot Unit with a specific support.

Particular care has been taken not to induce any mechanical stress on the wires of the windings and on the lead wires, as well as on any insulator present in the LVDT. Experience shows that materials which normally resist a high level of radiation may fail if submitted to continuous mechanical stress. For this reason a thermal firing treatment has been required to release all the stresses induced on the wires and insulators during the manufacture.

4.4.5 Operation and control system

The Roman Pots will be considered machine elements as the collimators. Therefore the control system is the same used for positioning and controlling the LHC collimators. The control system is based on NI-PXI systems. The control of the motors and the read-out of the position sensors and of the end-of-run switches will be available via the standard LHC control interface.

The software for the local control is based on National Instrument LabView [4-7]. The connection between the local control and the LHC control interface is provided via the FESA system [4-8], standard for the CERN accelerators controls, to provide the publication of the status to the LHC control and the transmission of the commands from it.

4.5 Installation and alignment

4.5.1 Roman Pot installation

The proposed position of the Roman Pots in the LHC lattice is driven by the requirement of having the possibility to reach the Coulomb interference region. For this reason we have to place the Roman Pots at about 240 m from the Interaction Point and beyond the sixth quadrupole Q6 (Figure 4-2).

As mentioned in Section 4.1, the only possibility is to place the Roman Pot units in between the three dump resistor boxes (DQR's) located between Q6 and Q7. The available space is very limited but the installation is feasible. The detail of this arrangement has been formulated in a ECR [4-9]. Figure 4-4 shows how one Roman Pot unit would be installed in between two DQR boxes.

Each Roman Pot unit will be supported by a support table with three legs as seen in Figure 4-4 and the main frame will in turn have three adjustable threaded rods placed on the table.

The Roman Pot units will not be ready for installation in time with the rest of the LHC initial installation and for this reason replacement chambers have been prepared by the AT/VAC group. Four replacement chambers on both left and right long straight section have already been installed. The replacement chambers will be supported by standard LHC vacuum chamber supports fixed on holes on the tunnel ground that are compatible with the future installation of the Roman Pot units support tables.

We intend to build a mock up of the area around the DQR boxes where the Roman Pots units will be installed. This will allow us to identify a suitable installation sequence and exercise the different steps involved. The time allocated for the installation may be limited due to other possible work going on in parallel on the machine and by the radiation dose levels. It is therefore important to have a precise protocol of installation.

The first step in the installation procedure will consist of the de-installation of the replacement chambers and of their supports. That will imply the vacuum breaking of the section where the Roman Pot units will have to be installed, as foreseen by sector valves installed not far from the Roman Pot units. Once the replacement chamber support is removed in each position, the three legs support table can be positioned and secured to the ground using the holes that have been already prepared in the four Roman Pot unit positions. The table will have to be aligned by the surveyors to correct for the tunnel floor inclination.

Finally the Roman Pot Unit will be placed on the table and by means of three threaded rods aligned, as described in next section.

4.5.2 Roman Pots alignment

Before the installation in the tunnel the alignment of the Roman Pot Unit will go through several stages, first at the assembling workshop using mechanical probes and comparators to spot out possible mounting defect, then by measurements done using the LASER Tracker technique [4-10]. Deviations from the vertical direction will be removed using the adjustment possibilities offered by the mechanics. The possible deformations due to operation under UHV will be measured and compensated where possible.

Each Roman Pot Unit will be supported by the support table that is positioned and fixed on the LHC tunnel ground. As mentioned in the previous section, the table will be aligned to the correct angle respect to the tunnel floor. That will be achieved by shims under the support table legs that will be installed permanently.

Between the table and the main body of the Unit there are three threaded rods that allow the precise positioning. The vertical alignment will be the first step in the sequence. The three threaded rods make the unit completely independent from the support table for what concerns the angular positioning respect to the floor, whose correctness is ensured by the support table and can be corrected to a higher precision by the vertical adjustments of the rods. That allows to decouple the alignment of the Roman Pot unit from possible imperfection and roughness of the tunnel floor.

Two of the threaded rods can also be moved on the plane parallel to the ground allowing the horizontal and angular alignment of the Unit respect to the plane orthogonal to the beam.

Once a Roman Pot unit will be correctly aligned in the space, the main vacuum chamber will be connected to the LHC beam pipe and there will be a precise alignment with respect to the Beam Position Monitor (BPM) placed on one side of the unit. The BPM will supply the first indication of the beam positioning for the coarse positioning of the Pots.

Further details of the alignment are still under discussion, like the cross-check of the position after the bake-out and the establishment of the nominal primary vacuum conditions and the periodic inspections during shutdowns.

The alignment of the detector inside the Pot and the transfer of this information to the outside is covered in the next chapter.

4.6 Roman Pots mechanics status

At the time of the preparation of this TDR the Roman Pot design has been finalized for all aspects concerning the positioning functionalities, the dimensions and the integration, both internal and with the LHC environment for the installation. A prototype of ATLAS Roman Pot unit has been produced by VAKUUM PRAHA (Czech Republic) and delivered at the end of 2006. This prototype has been equipped with the motors to perform precise measurements to fully validate the design.

The results of the measurements have helped to identify few flaws that have been promptly corrected to achieve higher precision in the movements. In detail the corrective actions have been:

- Change of material for the movable arms from Al to Stainless Steel, thus reducing by a factor three all possible deformations.
- Modify the requested planarity tolerances on both the back surface of the movable arms in the region where the movable parts of the rails are fixed and on the corresponding region on the main body where the fixed part of the rails are mounted.

The measurements done on the prototype unit, all the findings and the decision taken are documented in [4-11].

The production of the four Roman Pot Units is ongoing and expected to be delivered at CERN by the end of February 2008. An intensive program of measurements has been established that will allow, in parallel with the mounting activity, to characterize each unit and act when needed, to achieve the best possible movement precision and stability.

Two prototypes of the Pot are in preparation at CERN by the main workshop. One of them will be stressed at high vacuum up to destruction to assess the performance of the thin window and of the overlap extrusions brazing technique. The remaining prototype is being fully assembled with all the vacuum flanges, ready to be used for detector mounting tests and later for possible test beam use in Spring-Summer 2008. Depending on the results of the tests, a full production, with possible adjustments, will be started in Spring-Summer 2008.

The procurements of the motors, position sensors, encoders, limit switches, motor drivers and motor control system are in progress.

The fully assembled units with their pots will be ready for the installation, without detector, in Summer-Fall 2008. The installation will depend on the LHC schedule.

4.7 References

- 4-1 TOTEM Collaboration, TOTEM Technical Design Report, CERN-LHCC-2004-002.
- 4-2 F. Caspers, “*Impedance determinations*”, Handbook of Accelerator Physics and Engineering, World Scientific (1999).
- 4-3 F. Caspers, E. Gaxiola and T. Kroyer, “*Longitudinal and Transverse Wire Measurements for the Evaluation of Impedance Reduction Measures on the MKE Extraction Kickers*”, CERN-AB-Note-2007-028.
- 4-4 LHC Design Report, Vol. I, Chapter 5, CERN-2004-003 (2004).
- 4-5 F. Roncarolo, RF measurements and numerical simulations for the ATLAS Roman Pot system, note in preparation.
- 4-6 LHC Collimation group; Technical specifications for radiation hard stepping motors and contactless resolvers (<https://edms.cern.ch/file/625158/1/IT3385specification.pdf>); Technical specifications for radiation hard LVDT (<https://edms.cern.ch/file/690806/1/IT3425description.pdf>); Technical specifications of driver units for stepping motors (<https://edms.cern.ch/file/756464/1/IT3440specification.pdf>).
- 4-7 National Instrument, LabView and NI-PXI systems; <http://www.ni.com/>
- 4-8 A. Guerrero, J-J Gras, J-L. Nougaret, M. Ludwig, M. Arruat, S. Jackson, “*CERN Front-End Software Architecture for Accelerator Control (FESA)*”, Proceedings of ICALEPS Conference (2003).
- 4-9 I. Efthymiopoulos and P. Grafstrom, Engineering Change Request, LHC-XRP-EC-002.
- 4-10 T. Sager, “*Status report on the survey and alignment efforts at Fermilab*”, Proceedings of the Fifth International Workshop on Accelerator Alignment, ANL/FNAL 1997.
- 4-11 A. Braem et al., Measurements on ATLAS Roman Pot Unit prototype, note in preparation.

5 The Roman Pot detectors

After summarizing the basic detector requirements (Section 5.1) we describe the features and characteristics of the ALFA scintillating fibre detector (Section 5.2). This includes a discussion of the photodetectors, fibre characterization studies, overlap and trigger detectors and detector integration in the Roman Pots. It follows a discussion of the expected detector performance (Section 5.3) and finally a description of the detector construction sequence (Section 5.4).

5.1 The detector requirements

In the following we discuss the most important requirements on the detectors.

Dead space at the detector edge

The amount of dead space at the edge of detector, i.e. the size of the insensitive region, is a critical parameter. It is of vital importance to minimize this space in order to be able to approach the beam as close as possible and in this way maximize the acceptance for small $-t$ values. In addition to the dead space of the detector, one also has to consider the thickness of the window that separates the detector from the ultra high vacuum of the machine. Minimizing the thickness of this window requires that the detectors work in a secondary ‘safety’ vacuum. Electromagnetic shielding of the detector from the beam might also influence the distance of closest approach to the beam.

With the optics discussed in Section 3.2 (Table 3-1), the spot size at the detector σ_d is about 130 μm . This means that the closest possible distance to the beam will be about 1-2 mm in the case of a halo limitation (10-15 σ_d) or about 1.5 mm for a closed orbit limit. Thus, any dead space between the edge of the detector enclosure towards the beam and the sensitive (fully efficient) part of the detector larger than about 100 μm will worsen t_{min} significantly.

Spatial resolution

The spatial resolution of the detector has to be significantly smaller than the spot size of the beam at the detector σ_d in order not to be limited by the detector resolution. With a spot size of 130 μm , a spatial resolution of about 30 μm is considered adequate.

It is also necessary to measure the direction of the protons at the detector in order to be able to remove background from beam-gas interactions and beam wall interactions. With a lever arm of 4.14 m between adjacent Roman Pots, a detector resolution of about 30 μm is again adequate for this purpose (see Section 9.3.3).

Radiation hardness

Calculations by N. Mokhov indicate accumulated dose levels up to 10^5 - 10^6 Gy/yr close to the beam (215 m away from the IP and at a distance of 15 σ_d) at a luminosity of 10^{34} $\text{cm}^{-2}\text{s}^{-1}$ and $\beta^* = 0.5$ m [5-1]. These calculations only take into account the contribution from the interactions at the interaction point, which dominates at high luminosity, and thus this contribution can be scaled as the luminosity. Scaling down to a luminosity of 10^{27} $\text{cm}^{-2}\text{s}^{-1}$ gives accumulated doses of 0.01-0.1 Gy/yr. Here one should further note that a realistic running scenario for elastic scattering is of order one week.

There is also a contribution to the radiation from the beam halo. A rough estimate of its contribution based on the halo numbers given in Section 3.5.2, gives a dose of 10-100 Gy/yr. Thus, the halo contribution dominates completely and a total radiation hardness up to 100 Gy/yr is sufficient.

Electromagnetic shielding

For detectors and electronics operating close to the beam the electromagnetic radiation from the circulating bunches induces pick-up noise. Thus it is important to have detectors with low sensitivity to the electromagnetic pick-up or to install adequate electromagnetic shielding. In turn, such shielding contributes to the dead space between the beam vacuum and the sensitive part of the detector, and will limit t_{min} .

Rate capabilities and time resolution

Capabilities to deal with MHz rates would be largely sufficient. Timing resolution should be sufficient to identify the bunch crossing uniquely, and a resolution of 5 ns should be more than sufficient.

5.2 The ALFA scintillating fibre detector

A tracking detector based on scintillating fibres is able to fulfil all of the above requirements in a simple and cost effective way. Scintillating plastic fibers are intrinsically edgeless particle sensors. They are immune to signal pick-up from the circulating LHC beams and do not require cooling which facilitates operation under vacuum and integration in the Roman Pot.

Tracking detectors based on optical scintillating fibers have proven their excellent performance already in many HEP experiments, e.g. in the UA4/2 experiment at the $p\bar{p}$ collider at CERN [5-2] [5-3] or the fibre tracker of the D0 experiment [5-4] at Fermilab. Fiber trackers are simple in construction and operation. They do not need any internal calibration and can work at very high flux. Their sensitivity up to the edge is just limited by the inactive cladding ($\sim 10 \mu\text{m}$).

Our design (see Figs. 5-1 and 5-2) comprises scintillating plastic fibres of square cross section (Kuraray¹ SCSF-78, S-type, $0.5 \times 0.5 \text{ mm}^2$) which are arranged in UV or stereo geometry under an angle of 90° . As illustrated in Fig. 5-2, two layers (U and V) of 64 fibers each are glued on a $170 \mu\text{m}$ thick ceramic substrate and form a plane. Precisely machined stiffener plates of 0.5 mm thickness in the non-active regions of the plane lead to a compact and mechanically rigid assembly, a concept which has been validated by thermomechanical calculations [5-5].

Ten planes, staggered by multiples of $0.5 \text{ mm} / 10 \cdot \sqrt{2} = 70.7 \mu\text{m}$, are assembled through precisely machined hardened steel blades on precision pins to a detector with an effective fiber pitch of $50 \mu\text{m}$. Its ultimate spatial resolution, ignoring any geometrical imperfections, is $\sigma_x = \sigma_y = 50 \mu\text{m} / \sqrt{12} = 14.4 \mu\text{m}$. The z -spacing of the planes is 2.3 mm . The staggering step of $70 \mu\text{m}$ per plane means that the fibre positions are aligned under an angle $\alpha = \arctan(70/2500) = 28 \text{ mrad}$ relative to the z -axis. To achieve optimum spatial resolution with this detector concept, the beam divergence σ_x , and σ_y , must be small compared to α . Moreover, the detector axis should be aligned with the beam axis to a precision which is again small compared to α , e.g. to 3 mrad .

Most of the fibre ends are cut at the lower end under an angle of 45° . The particular geometry of the Roman Pot with its thinned window requires to cut the fibres at the periphery of the layers under 90° .

The fibres are routed over about 25 cm to a vacuum flange, in the following called *connector flange* (see Fig. 5-3). Groups of 64 fibers (8×8 fibres with a pitch of 2.3 mm) are glued into O-ring sealed connectors which fit into this flange. The scintillation light is then read by photodetectors with matched read out pitch which are mounted on the opposite side of the connector flange without an optical contact medium.

1. Kuraray Co LTD., Tokyo, Japan

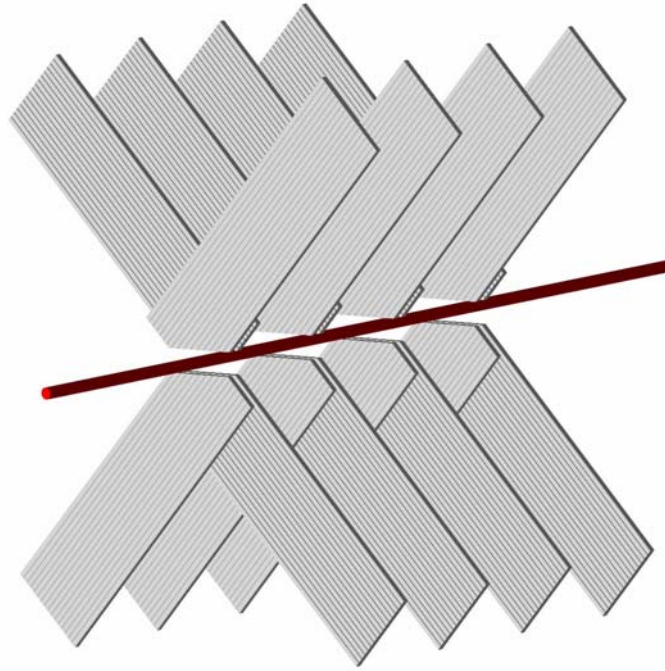


Figure 5-1 Principle of a scintillating fibre detector with 4 planes in UV geometry. The active area is limited to the overlap region of the fiber layers.

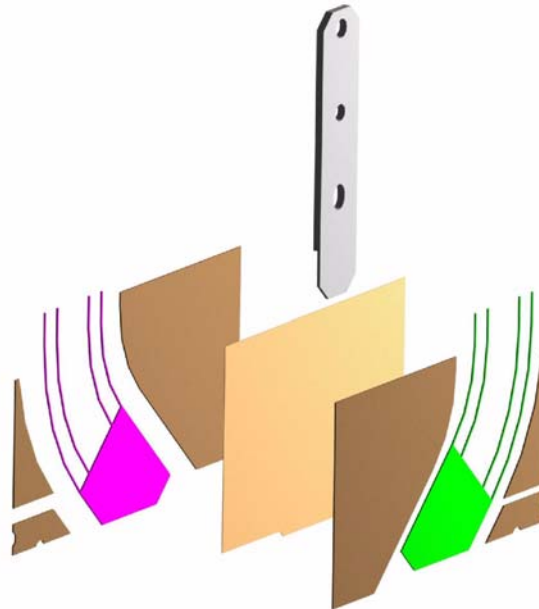


Figure 5-2 Representation of a *UV* detector plane (exploded view) showing fibres, ceramic support structures and stainless steel blade.

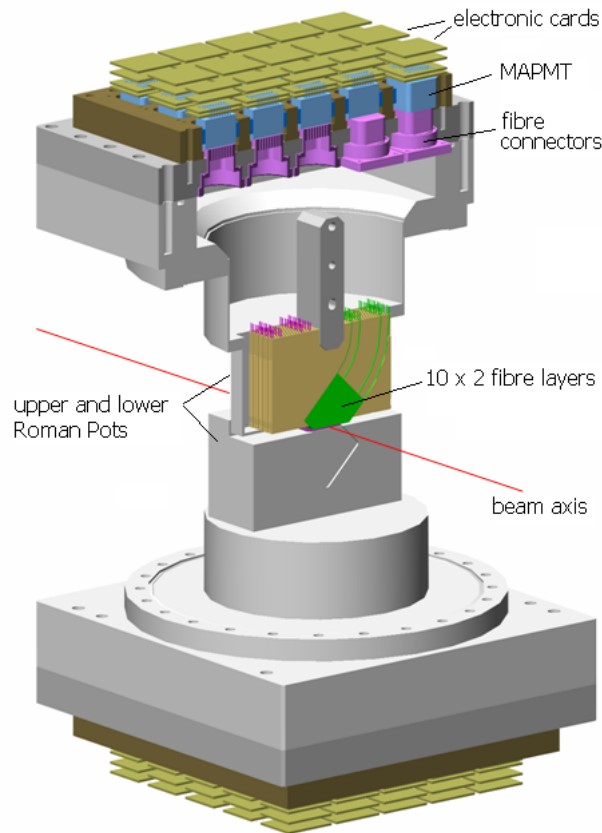


Figure 5-3 3D view of an upper and lower detector and their Roman Pots. For clarity the routing of the fibres to the photodetectors is not shown. The overlap and trigger counters are not shown in this view.

5.2.1 Photodetectors

The photodetectors are a key component of the scintillating fiber detector. The main requirements of the photodetectors are:

- High quantum efficiency at the wavelength of maximum scintillation
- Capability to detect single photons
- Fast signal characteristics to allow unambiguous identification of LHC bunches
- High gain in order to allow the use of simple read-out electronics
- Relatively low cost per read-out channel
- Robustness and reliability
- Moderate radiation hardness

Multi Anode PhotoMultiplier Tubes (MAPMTs) represent a well established commercially available and robust technology, used in numerous HEP experiments [5-6]. The quantum efficiency of the bi- or multi-alkali photocathode is of the order of 20% in the blue range of the optical spectrum. Single photoelectrons can be detected with an efficiency of typically 70%, leading to an effective detection efficiency of 14%. Currently available MAPMT technology such as the Hamamatsu¹ R7600 family provide up to 64 channels per tube with a nominal cell size of $2.3 \times 2.3 \text{ mm}^2$. The so-called flat-panel technology (Hamamatsu

H8500, H9500 with 64 or 256 channels per device) is not considered as alternative as the reduced detector length is set off by worse sensitivity and gain characteristics. The French company Photonis works on the development of a multi-anode technology similar to the one of Hamamatsu. The devices are expected to be geometrically and electrically 100% compatible to Hamamatsu's R7600 series. If successful this should lead to a price reduction and possibly also to a performance increase.

Our baseline photodetector is the Hamamatsu MAPMT R7600 with 64 channels. The 10 dynode stages lead to a gain of $\sim 10^6$ at an applied voltage of about 1000 V. The gain is reasonably uniform over the 64 channels (typically a factor 2-3 variation). Cross talk between adjacent channels is at the level of 2-3%. Mu-metal shielding is required in the presence of stray magnetic fields in excess of 10 Gauss, in order to maintain the gain and hence the detection efficiency at the nominal value. Cross-talk is not enhanced by the presence of a moderate magnetic field.

Custom designed high voltage divider and front-end readout electronics form a very compact assembly and sit directly on the MAPMTs (see Chapter 6).

In the green wavelength region the Q.E. of a standard bialkali or multi-alkali photocathode is only about 10%, disfavours the use of green-emitting and more radiation hard 3HF fibers from Kuraray. An alternative concept, possibly of interest for a later detector upgrade, is the use of Geiger mode APDs (also called Silicon photomultipliers) [5-7]. Many of their characteristics like single photon response, high detection efficiency in the visible domain, high gain ($\sim 10^6$) at low bias voltage (~ 100 V) and very good timing properties (< 1 ns) make them very attractive for ALFA, however some of their properties, the dark count rate (10^6 mm⁻²) for example, can be a problem. In a triggered readout scheme, as the one used for ALFA the latter problem is probably not a serious one. Once available with optimized characteristics and in quantity a potentially cheap solid state device like the Si-PM could allow to build a more radiation tolerant fibre detector of reduced size and cost. We intend to follow the evolution of this technology and to experimentally explore on a small scale its possible gain for our application.

5.2.2 Fibre studies

Our baseline fibre is the single cladded 0.5 mm square fibre SCSF-78, S-type, from Kuraray. The cladding thickness is 10 μ m. The fibre's emission spectrum expands from $\lambda \sim 415$ nm to above 550 nm with a maximum around 440 nm (for fibres of short length). Our design requires only relatively short pieces of fibres (~ 30 cm) but small bending radii (~ 30 mm). The S type fibre whose core consists of axially oriented polymer chains represents the better compromise between light attenuation length and minimum bending radius. To minimize optical cross-talk between closely packed fibres their surface is coated with a vacuum evaporated Al film of about 100 nm thickness which acts also as high quality mirror ($R \sim 0.8$).

Prior to design and construction of the prototype detector a number of lab tests were performed to characterize the fibres in terms of light attenuation length (in the emission wavelength band), minimum bending radius, scintillation light yield and surface quality of the end cut (under 45° and 90°). We summarize here the main results. More details can be found in [5-8][5-9][5-10].

The light attenuation length was measured by exciting the fibre laterally with a monochromatic UV light source at 350 nm at a defined distance from the photodetector which was either a PMT (Photonis XP2962) with bialkali cathode or a Silicon photodiode (Newport 818-UV). Light propagating in the fibre cladding was suppressed by a black coating. The results obtained with the PMT and short fibres (30 cm) are well described by an exponential with the attenuation length $\lambda_{\text{att}} = 70$ cm. Measurements with long fi-

1. Hamamatsu Photonics K.K., Hamamatsu City, Japan.

bles and photodiode readout can be described by two exponentials with $\lambda_{att} = 120$ cm for $0 \leq L \leq 60$ cm and $\lambda_{att} = 170$ cm for $120 \leq L \leq 300$ cm. These values remain significantly behind the >400 cm which are advertised in the Kuraray documentation for round fibres of the same type.

Special care was attributed to the surface quality of the end cuts of the fibres. As 50 % of the scintillation light is emitted in the direction away from the photodetector, light reflected from the opposite fibre end can contribute significantly to the total light yield. The fibre ends were machined with a single point diamond tool on a low vibration computer numeric controlled (CNC) machine. High rotation frequency (20.000 min^{-1}) and low feed (0.02 mm per turn) gave the best results. A reflective Aluminium coating was applied by vacuum evaporation to the fibre ends which were cut under 90° . For fibres of 30 cm length this resulted in an increase in light yield of 58 % compared to uncoated fibres. The reflectivity at the Aluminium (Al) - Polystyrene (PS) interface was found to be approximately 0.75. For fibres with a 45° end cut an uncoated surface was found to lead to the highest light yield. A significant fraction of the scintillation light hits the machined surface at angles exceeding the critical angle for total internal reflection ($\theta_{crit.} = \arcsin(n_{air}/n_{PS}) \sim 39^\circ$). The reflected light undergoes then a reflection from the fibre side which is also Al coated. Via another reflection from the machined surface the light is reinjected into the fibre and propagates now towards the photodetector. The resulting gain in light yield was found to be about 42% (again compared to an uncoated fibre with 90° end cut). The reflectivity for different configurations are summarized in Figure 5-4.

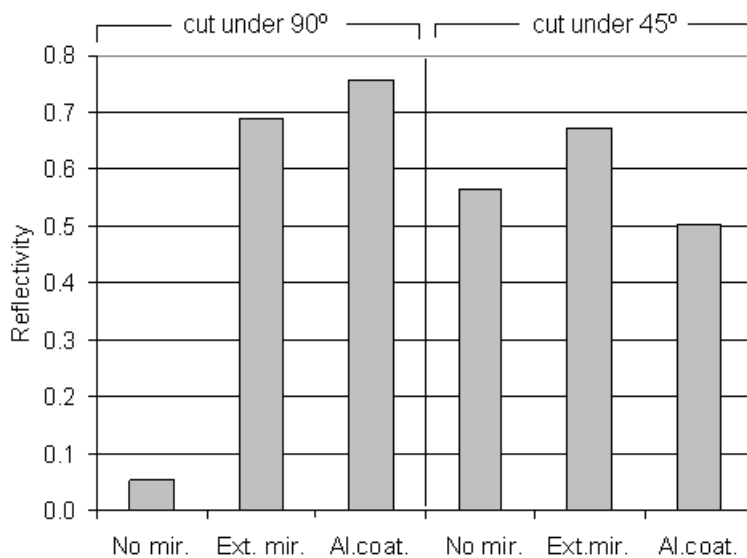


Figure 5-4 Results of machining and end coating studies with SCSF-78 fibres. For fibres with a 45° cut the use of a high quality external mirror would give the best reflectivity, however it would lead to an unwanted inactive detector edge.

For the series production, Al coating by sputtering is considered as baseline, as this technique is expected to lead to superior mechanical properties of the coated film. Sputtering was previously used for the aluminisation of the TileCal fibres [5-11].

The Kuraray SCSF-78 fibre has been investigated in terms of radiation hardness in a prototype study for the possible use of this technology in the inner tracker of HERA-B. Irradiations with protons, electrons and photons (^{60}Co) up to doses of 10 kGy (= 1 MRad) were performed [5-12][5-13]. For doses above 1 kGy the light yield was found to decrease noticeably ($\sim 10\%$ at 1 kGy, 30% at 10 kGy) however it recovered fully with a time constant of weeks after the end of the exposure. It is safe to assume that radiation

damage is not a critical issue when the detectors are used for measurements at low luminosity. The technology provides a comfortable safety margin even in case backgrounds (halo) turn out to be much higher than expected.

Still, we made a measurement of our own and scintillating fibres of various types were irradiated with protons in the IRRAD1 facility [5-14] in the T7 beam line of the CERN PS accelerator. The fibres were exposed to 24 GeV/c protons with fluences ranging from $6.78 \cdot 10^{11} \text{ p cm}^{-2}$ to $8.40 \cdot 10^{15} \text{ p cm}^{-2}$. A specially designed tooling allowed simultaneous irradiation of fibres along the beam axis and fibres perpendicular to the beam. The irradiation campaign lasted one month and seven batches of fibres were irradiated to doses ranging from about 100 Gy to more than 2 MGy. The light yield of fibres was measured by exciting them with a Sr-90 source. The fibre under test was coupled to a silicon photomultiplier¹. An Al-coated reference fibre coupled to a photomultiplier tube² served as trigger. From the spectra obtained we determined the average number of photoelectrons for each fibre and calculated the detection efficiency. The analysis is ongoing and preliminary results [5-15] show that the ALFA baseline fibre's efficiency starts decreasing for doses greater than 3 kGy. This confirms the full suitability of the scintillating fibre technology for luminosity measurements and indicates its potential for physics runs in an intermediate luminosity range.

5.2.3 Overlap detectors

The exact position of the LHC beam spot at the location of the ALFA tracking station can vary from fill to fill by a couple of mm. It is therefore necessary to position the upper and lower ALFA detectors symmetrically to the actual beam before any meaningful measurements can start. The first rough positioning will be done using a Beam Position Monitor (see Section 4.2.1) located in the immediate neighbourhood of the Roman Pot unit. Asymmetric vertical positioning of the two detector halves relative to the beam spot would show up in the data as asymmetric occupancy distributions and could be in principle corrected for offline. Similarly a horizontal relative displacement of the two halves becomes evident in the data and can be corrected. A symmetric vertical displacement of the upper and lower ALFA detectors relative to their default position can however not be derived from the data. The precision with which the distance between the two detectors is known has a direct consequence on the uncertainty of the luminosity. If the upper and lower detectors approach the beam to a distance of 1.5 mm, a systematic shift of $\Delta y = 15 \mu\text{m}$ represents a positioning error $\Delta y/y$ of 1%, and consequently an angular error $\Delta\theta/\theta$ of 1%, implying a 2% error in the luminosity. We conclude that vertical the distance between the two ALFA half detectors must be known with a precision of about $10 \mu\text{m}$ [5-16][5-17].

The vertical distance between the two detectors can be determined by means of so-called overlap detectors. The overlap detectors (ODs) are detectors which measure only the vertical coordinate. Two ODs are mounted below (and above) the actual detector planes. They move with the detector planes and their relative position to those is fixed and well known. The ODs detect particles in the beam halo region. The active areas of the ODs begin to overlap when the detector halves approach each other. The distance of the detector halves can be calculated from the measurement of particles which traverse both ODs:

$$d = \frac{1}{N} \sum (y_{1,i} - y_{2,i}) .$$

The required measurement precision is obtained by recording a sufficiently large number of tracks and calculating their average deviation in the two ODs. The achievable precision depends on three factors: (1) the intrinsic spatial resolution of the OD, (2) the statistics of particles detected with the OD, and (3) the alignment uncertainty between the ODs and the detector halves.

1. Hamamatsu MPPC (Multi Pixel Photon Counter) S10362-11-100U.
2. Hamamatsu R647-01.

The overlap detectors consist of horizontally mounted scintillating fibres of the same type and size as the main detector. They cover an active area of 6×15 mm. An OD comprises 3 planes of 30 fibres. The three planes are vertically staggered by 166 and 333 μm , respectively, such that a detector with an effective pitch of 166 μm is formed. The horizontal fibres are bent by 90° and routed upwards to the MAPMTs. In order to maximize the bending radii of the fibres, the 30 fibres are split into two layers of 15 fibres each which are mounted on the front and the back side, respectively, of a ceramic support plate. A fourth ceramic plate supports plastic scintillator tiles which act as trigger counters for the overlap detectors. Front and top view of the overlap detectors integrated with the main detectors is shown in Figures 5-5 and 5-6.

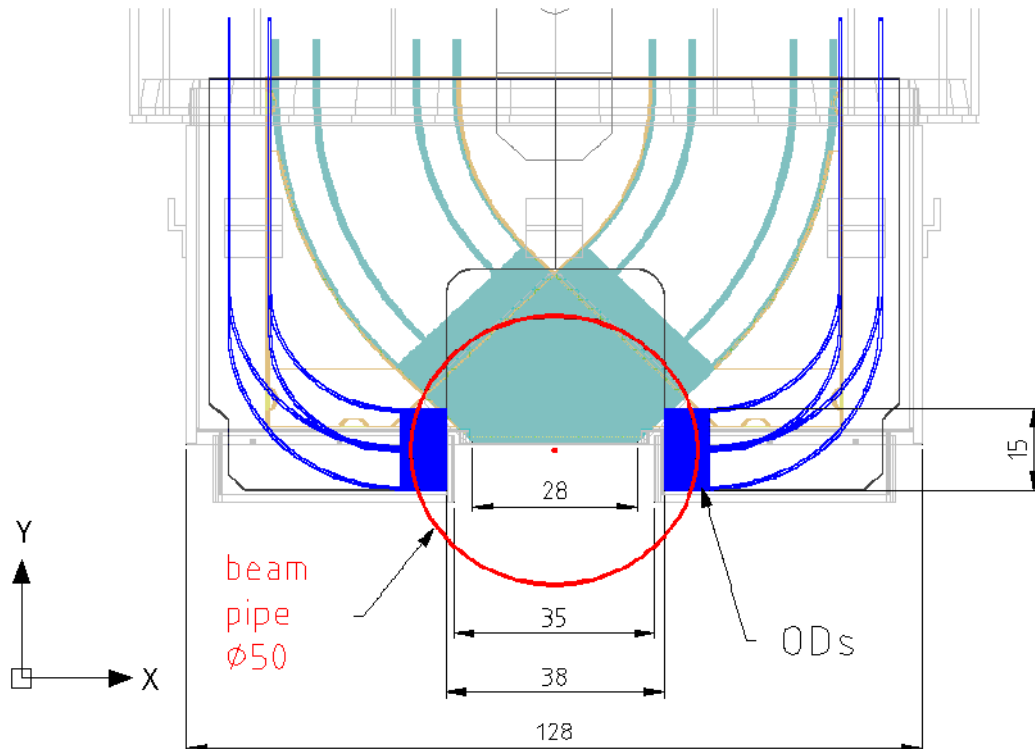


Figure 5-5 Front view of the full detector assembly with the overlap detectors. The spot and the circle in the centre represent the beam axis and the beam tube (diameter 50 mm). Not shown are the beam screens which have at the nearby quadrupole Q6 a horizontal free aperture of 44 mm.

The two ODs are mounted symmetrically on both sides of the main detector and are housed in two special extrusions of the Roman Pot envelope (see Figure 5-7). The design of the ODs is a compromise in order to satisfy the manifold physics and technical constraints. In the horizontal plane the distance between OD edge and the beam axis is 19 mm which means that about $2/3$ of the active surface is inside the beam tube radius of 25 mm. The longitudinal distance between the two OD sets is 43 mm. The ODs start to overlap when the two pots have a distance of 8.5 mm from the beam axis. The maximum vertical overlap is 15 mm.

5.2.4 Trigger scintillators

Both the ALFA main detectors and the overlap detectors are equipped with dedicated trigger counters which define the active area. As the fibres are also sensitive in the part which is only used as light guide, the trigger counters avoid false hits in this part which can be generated by beam halo particles. A conven-

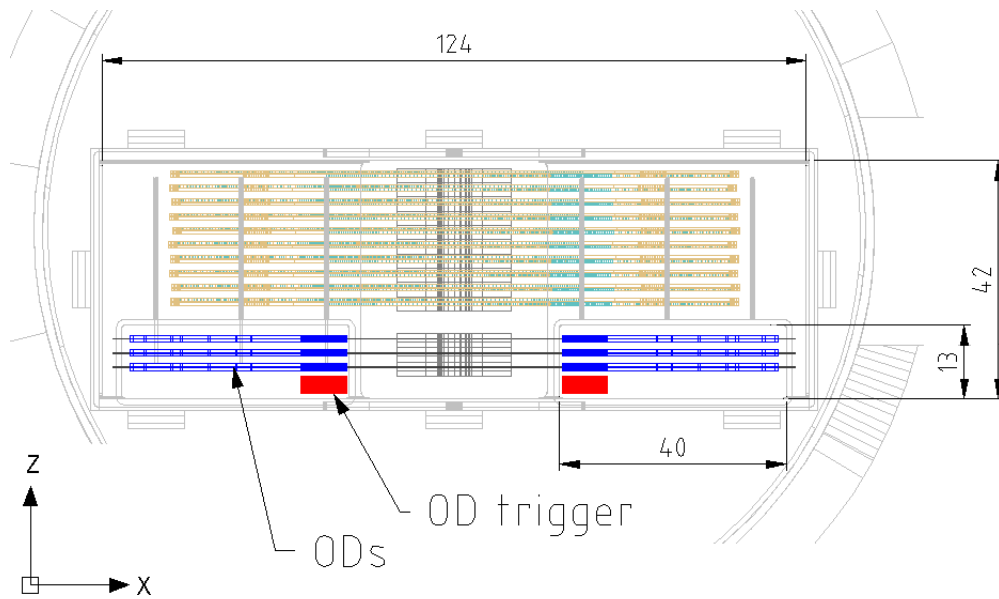


Figure 5-6 Top view of the detector assembly. The first three planes (from the bottom) belong to the overlap detectors. The overlap triggers are also shown (without support plane).

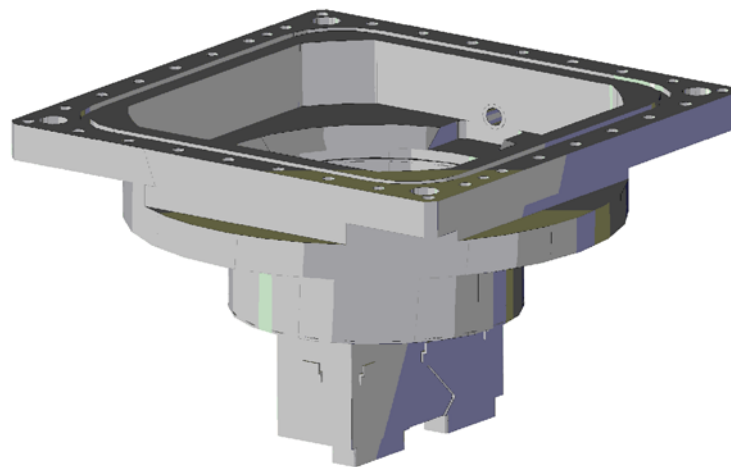


Figure 5-7 Roman Pot with extrusions for the overlap detectors.

tional fast plastic scintillator tile (e.g. Bicron BC-408 or similar) of 3 mm thickness, whose shape matches the overlap area of the U and V fibres and which is mounted directly in front of the 10 planes, generates a local trigger signal. Similarly, rectangular scintillator tiles of 15×6 mm are mounted in front of the two active zones of the overlap detectors. Uniform response is a key requirement to the trigger counters. Any position dependence would lead to distortions in the measured t -distribution or, in case of the overlap detectors, to false position reconstruction. Consequently, efficient light coupling and guiding is required. Tests with compact and flexible wavelength shifter bar readout schemes revealed a marginal number of detected photons (<10) and consequently the risk of efficiency variations. We opted for fish tail type light guides, specifically shaped to cope with the space constraints (see Figure 5-8). The scintillation light is collected and guided to small single channel photomultipliers (Hamamatsu R1635, 8 mm \varnothing) which, for sim-

plicity, are located on the vacuum side of the connector flange. The yield, measured with a Sr-90 source, was of the order 40 detected photons, which promises 100% detection efficiency over the full surface.

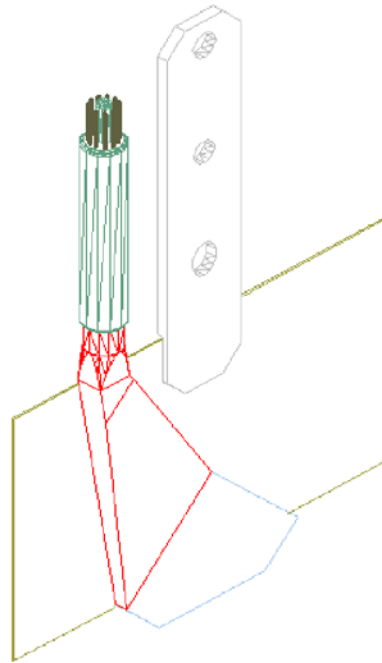


Figure 5-8 Design of the trigger counter. The light guide is designed to maintain a maximum cross section from scintillator to PMT.

5.2.5 Detector Integration in the Roman Pots

Our design foresees 64 fibres per layer. This brings the total number of fibres per Roman Pot module to 1280. In addition there are 3×60 fibres of the overlap detectors, requiring a total of 23 MAPMTs per pot plus three single channel PMTs for the readout of the trigger counters.

The 23 MAPMTs are arranged in a 5×5 grid defined by molded epoxy frame which includes a mu-metal structure as magnetic shield. The effectiveness of the shield up to a field strength of 30 G has been demonstrated by simulations [5-18] with the finite element code MAFIA [5-19]. The central position of the matrix does not house a PMT. At this location the support arm which carries the fibre detector is fixed to the connector flange. The second unused position is used for passing the signal and HV cables of the trigger PMTs through the connector flange. The non-conductive epoxy frame also ensures the electrical insulation of the MAPMT body which is on the same potential as the photocathode, i.e. typically -900 to -1000 V.

The MAPMT input mask which defines the dynode channels and hence its pixel structure is not perfectly aligned with the MAPMT external body. The pixels need however to be aligned with the fibre matrix of the connector to a precision of 0.1 mm in order to minimize cross talk between adjacent pixels. The problem is solved by gluing plastic spacers of individually chosen thickness (typically 2 mm) on the 4 MAPMT side walls. The thickness of the spacers is derived from a measurement of the positions of optical markers on the MAPMT input mask relative to their external body. Once the MAPMT is shimmed with

the spacers, its new ‘universal’ outside envelope is centred w.r.t. its input mask and it can be mounted in any position of the grid.

Attached to the epoxy frame are small clamps which slightly push down the MAPMT in order to ensure mechanical contact to the connector. Optical grease or contact pads are not foreseen.

Positioning and referencing the detectors in the pots

The positioning and precise referencing of the detectors in the pots are crucial for the final performance of the ALFA system. We summarize the main requirements:

- The detectors must be mounted inside the pot with a small but controlled distance of the order 100 - 200 μm between the active detector edge and the lower pot window.
- The tilt and rotation angles (around the axis transverse to the beam) have to be smaller than 2 mrad for optimum spatial resolution.
- The lower active detector edge should be aligned horizontally with the beam coordinate system with a precision higher than 1 mrad. If this is not the case, it is sufficient to be able to measure it and correct for it.

The fact that the location of the beam axis may change from fill to fill by millimeters makes the knowledge of the absolute horizontal and vertical positions of the detectors obsolete. Only their relative position to the beam is relevant. Horizontal rel. displacements of the two detector halves as well as vertical asymmetric displacements can be identified in the scattering angular distributions and corrected offline. The vertical distance of the two halves is measured and adjusted by means of the overlap detectors.

Two positioning and referencing schemes of the detectors relative to the Roman Pots have been considered:

1. Suspending the detector rigidly from the connector flange. The position of the detector inside the pot is derived from fiducials on the air side of the connector flange which are accessible at any time for metrological measurements.
2. Suspending the detector in a flexible way from the connector flange. The detector slides in the pot and is positioned by means of a set of spring loaded blades relative to the pot walls. The position of the detector is determined by the geometry of the pot itself which has been measured before relative to fiducials on the flange of the pot which is accessible from outside.

We favour the first scheme as it is conceptually simpler, mechanically more solid and more reliable. The second scheme is expected to minimize the distance between detector edge and vacuum window in a straight forward way. However, one needs to rely on the correct and reliable positioning of the detectors in the pot, a step which in the presence of friction and gravitation may give unpredictable results.

The positioning and referencing sequence for the first scheme is as follows:

1. The pots are fabricated inside tight geometrical tolerances. The pot is closed with the connector flange, still without detector. A set of precision pins with moderate play ensure alignment of the connector flange and the vacuum flange of the pot. Two pairs of fiducials are fixed on two adjacent sides of the connector flange. They remain accessible also after the final assembly. The four fiducials define a local cartesian coordinate system. The geometry of the pot, in particular the position of the window are determined by a metrological measurement relative to this coordinate system.
2. The connector flange is removed and the detector is fixed by a static mount. The detector length and its alignment to the flange are measured in the above defined coordinate system. If any of the detector edges lies outside the limits given by the measured pot geometry, this is corrected by adapting the detector mount.

3. The flange with the detector is then inserted in the pot and bolted. The precision pins ensure that the detector slides into the pot without risk of touching the pot walls.

The approach has the advantage that the position of the detectors can be redetermined via the 4 external fiducials at any moment, in particular once the pots are evacuated and moved into beam position.

5.3 Performance estimates

A sufficiently high light or photoelectric yield is a key requirement for good detection efficiency and finally spatial resolution. The expected photoelectric yield

$$N_{pe} = N_{scint} \cdot \varepsilon_{acc} \cdot \varepsilon_{transp} \cdot \varepsilon_{refl} \cdot \varepsilon_{gap} \cdot \varepsilon_{Q_{eff}} \quad 5-1$$

can be estimated with $N_{scint} = 1660mm^{-1} \cdot 0,48mm = 797$ being the number of generated scintillation photons for a traversing m.i.p.¹, $\varepsilon_{acc} = 0.042$ being the geometrical acceptance factor of a rectangular fibre, $\varepsilon_{transp} = \exp(-30/70) = 0.65$ being the transport efficiency due to optical absorption, $\varepsilon_{refl} = 1.58$ (90° cut) or 1.42 (45° cut) being the gain due to reflection from the opposite fibre end, $\varepsilon_{gap} = 0.9$ being the transmission at the fibre / air / glass interface without any grease, and $\varepsilon_{Q_{eff}} = 0.14$ being the effective quantum efficiency of the MAPMT². The equation leads to $N_{p.e.} = 4.3$ for fibers with a 90° cut and 3.9 for fibers with a 45° end cut.

A photoelectric yield of 4 promises an excellent single fibre detection efficiency. An optimistic estimate can be derived from $\varepsilon_{det} = 1 - P(0, \mu)$ where $P(0, \mu) = e^{-\mu}$ corresponds to the Poissonian probability to have zero photoelectrons when the average number is μ . From $\mu = 4$ follows a single fiber efficiency $\varepsilon_{det} = 98.2\%$. This simple estimate ignores geometrical inefficiencies (cladding, glue between fibres) and assumes that a single photoelectron can be detected by the DAQ system with 100% efficiency.

The space point resolution of the ALFA detector is driven by three main factors:

1. the fibre dimensions and the effective pitch determined by the plane-to-plane staggering
2. the accuracy of the fibre positioning and the knowledge of the actual fibre positions
3. the beam and operational parameters.

Studies were first performed with geometrical Monte-Carlo codes which indicated that our design was able to reach a spatial resolution $\sigma_x = \sigma_y \sim 20-25 \mu m$. Cross-talk which potentially can deteriorate the spatial resolution was not included in this initial study.

The aluminization of the fibres suppresses efficiently propagation of the primary scintillation light between fibres. Apart from coupling effects in the electronics chain there remain two further sources of cross-talk:

1. Optical cross-talk at the level of the MAPMT input window and electron-optical cross-talk in the MAPMT itself are expected to be of the order of a few percent. The signals produced by this kind

1. We assume an energy loss in polystyrene of 0.2 MeV/mm and a scintillation yield of 8300 photons/MeV.
2. $\varepsilon_{Q_{eff}}$ is the product of quantum efficiency at 450 nm (~0.2) and photoelectron collection efficiency. The latter has not been measured explicitly. We took the value of 0.7 which was communicated by M. Metzger, Hamamatsu Photonics, Switzerland, for the R7600-00-M64 MAPMT.

of cross-talk have low amplitude (normally single photoelectrons) and can as such be suppressed by an appropriate threshold setting.

2. Physics phenomena, like delta electron and shower formation in upstream detector or structural material can also produce cross-talk phenomena like signals in adjacent fibres. In this case the signal amplitude is expected to be of the same size as the actual signal and a discrimination is not possible.

A GEANT4 Monte-Carlo study [5-20] addressed these effects in a detailed way and investigated in particular their energy dependence. It used the true measured geometry of the detector *ALFA 10_2_16*¹ which was used in the DESY test beam in autumn 2005 (see Section 8.1). The study revealed the expected $1/E$ -dependence of the resolution function at low energies and reproduced the resolution of 36 μm which was experimentally determined in the test beam (see Figure 5-9). At TeV energies the above mentioned phenomena become negligible and the resolution tends to about 20 μm .

5.4 Detector construction and metrology

The full ALFA system comprises 8 Roman Pot detectors. Table 5-1 gives an overview of the involved components.

5.4.1 Fabrication and assembly sequence

In the following we describe the fabrication sequence and the metrological survey of 10 different prototype detectors which were used in beam tests at DESY in October 2005 and at CERN in 2006 (see Chapter 8). The sequence can, with minor adaptations, be applied to a full scale series production.

The detector construction was a multi-step process which to a large part took place in a clean room (class 10.000). Whenever possible components were standardized. The detectors *ALFA 10_2_6* and *ALFA 10_2_16* consisted for example of 10 identical UV planes. The staggering of the planes in steps of $n \times 70.7 \mu\text{m}$ ($0 \leq n \leq 9$) was only introduced when the steel blades (see below) were glued to the planes.

We used simple but precise 3-point alignment tools which were specifically designed and fabricated on a CNC machine to a precision of better than 10 μm . Optical survey^{2,3} with an accuracy of about 3 μm was performed at three stages of the fabrication process. The results of the 2006 metrology campaign are described in [5-21].

The sequence of steps was:

1. LASER cutting in industry of the central and stiffener plates from Al_2O_3 ceramic sheets at a modest precision of about $\pm 30 \mu\text{m}$.
2. Survey of the plates' geometry and selection of the best matching sets.

-
1. Our detectors are named according to the following scheme: *ALFA P_L_F*, where *P* is the number of detector planes, *L* the number of layers per plane (usually 1 U and 1 V layer, i.e. 2 in total), and *F* is the number of fibres per layer.
 2. CERN metrology service, 3D optical coordinate measurement machine MAHR OMS-600.
 3. PH Departmental Silicon Facility, 3D optical coordinate measurement machine OGP Smartscope CNC 250.

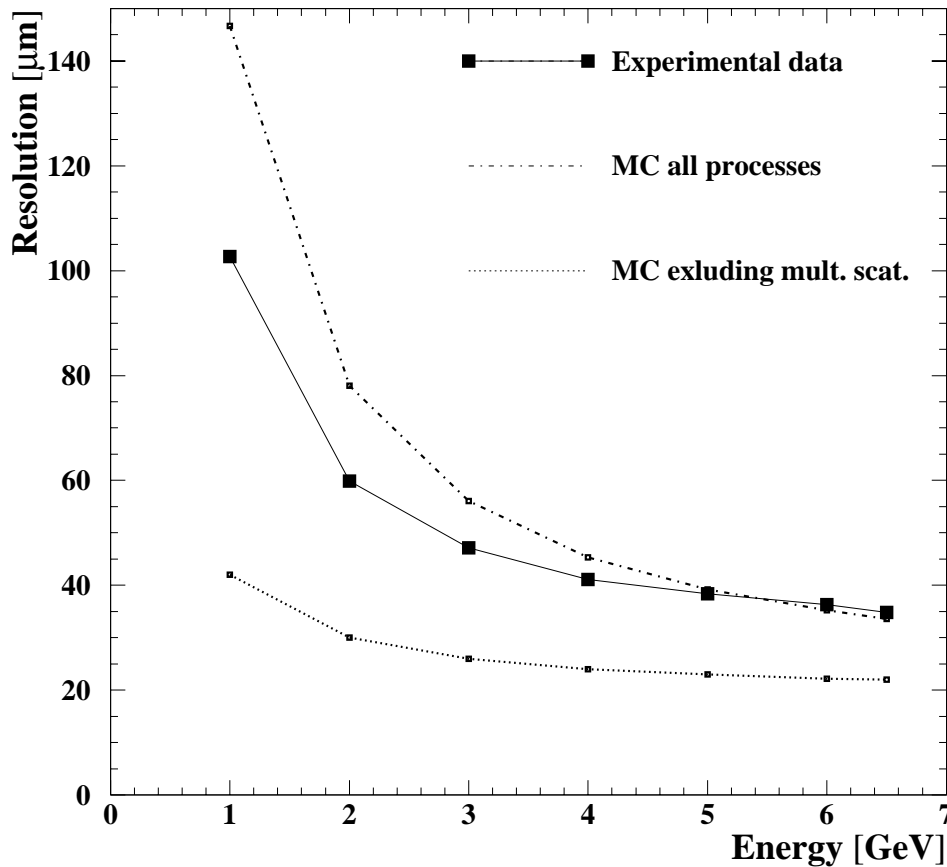


Figure 5-9 Contribution of different processes to the position resolution vs. electrons energy. The resolution scales in very good approximation like $1/E$ and tends to about $20 \mu\text{m}$ for infinite electron energy. The experimental data from the test beam at DESY (see Section 8.1) are also included.

Table 5-1 Component count for one Roman Pot detector and for the full ALFA system.

Roman Pot detectors	Fibres (main detector)	Fibres (overlap detectors)	Trigger scintillators (main+overlap)	MAPMT R7600	PMT R1635
1	1280	180	3	23	3
8	10240	1440	24	184	24

3. Gluing of left stiffener plates on front and rear side. Alignment via lateral and bottom edges.
4. Survey for control and determination of reference points.
5. Positioning and glueing of the Al coated fibres, one side after the other. The fibres were aligned with the 45° edge of the left stiffener plate and gently compressed by the right plate. 'Optical cement' Bicon BC-600 was used to glue both fibres and ceramic components. The ends of the fibres with a 90° cut had been machined and Al-coated before. The fibres with the uncoated 45° cut were left a few mm longer than needed.

6. Machining (single point diamond tool) of the fibre ends (45° cut) to final length and surface quality.
7. Glueing of the support blade made of hardened steel. The position of the blade was chosen to produce the desired staggering. This step was done by means of an alignment plate which provided a specific position for each displacement and allowed also to (partly) correct for small geometrical errors accumulated in the sequence up to this point.
8. Survey of fibre positions and angles relative to the precision holes of the steel blade.
9. Assembly of the planes on a support arm through two precision pins.
10. Threading of the fibres into the connector and subsequent glueing. A system has been adopted which avoids that adjacent fibres on the detector are not connected to adjacent channels on the MAPMT.
11. Machining (diamond tool) of the protruding fibre ends on the connector.

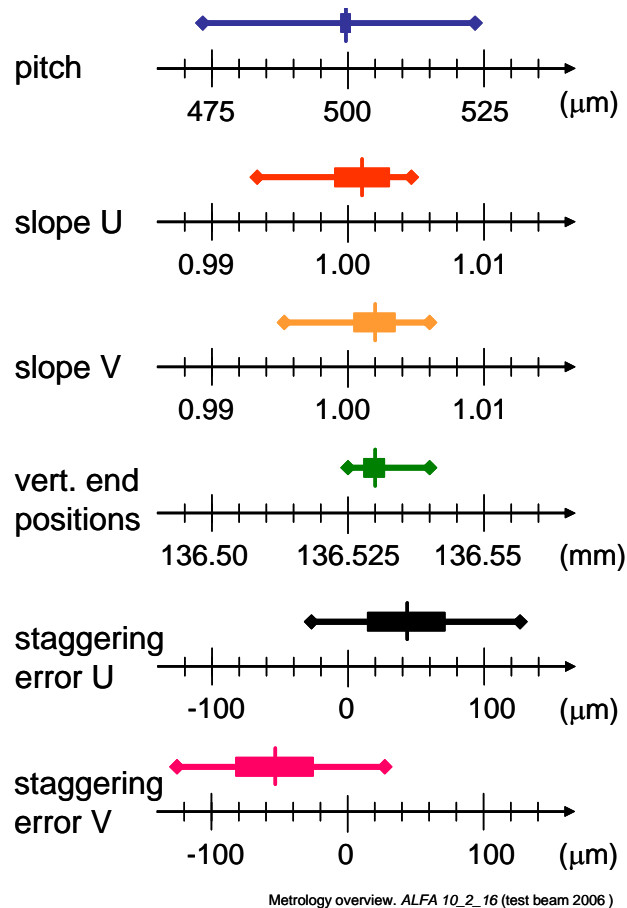


Figure 5-10 Results of the final metrology of detector *ALFA 10_2_16*. The vertical lines in the centre correspond to the average values, the broad bands to the RMS deviations and the lines with endpoints to the minimum and maximum values of the measurements.

The results of the final survey of the detectors *ALFA 10_2_16* which was used for the spatial resolution measurements are shown in Fig. 5-10. The geometrical data of all detectors like the positions of the first fibre (x,y,z) of each layer, the average fibre pitches and angles of each layer were recorded in *geometry files* and later used in the space point reconstruction.

The detector *ALFA 2_2_64* shows significantly larger deviations from the ideal geometry. Cumulative effects in the slope parameters and, even more expressed, in the staggering are observed. The vector field plots [5-21] show similar patterns as for *ALFA 10_2_16*, however the distortions are typically a factor 2 larger. Despite these substantial distortions, a geometrical Monte-Carlo code indicates that a hypothetical detector *ALFA 10_2_64* of comparable quality would have a resolution just below 30 μm [5-21].

5.4.2 Consideration on an improved detector concept

The geometrical distortion patterns observed in *ALFA 2_2_64* reveal a weakness of the fibre gluing procedure applied up to now. The fibres positions in the central part, far away from the spacers, are subject to cumulative effects (glue excess, fibre diameter, fibre deformation) which are difficult to control. Experience shows that the viscosity increase of the glue during the time the fibres are placed and positioned is of particular relevance for the final accuracy. The currently applied procedure relies on the dexterity and swiftness of the operator.

Improvements of the assembly and gluing method are being studied with the aim to reduce the distortions and to give additional safety margin for the spatial resolution. A promising concept currently under test is to place the fibres on a precisely fabricated Ti support plate first without glue. The fibres can freely move and are expected to position themselves with a constant pitch. The position of the fibres can be verified and, if required, be corrected. The glue is applied in a second step without changing the position of the fibres. Driven by the capillary effect the glue fills the gaps between the fibres and the structured substrate plate. If successful, this new method will already be applied in the fabrication of the first full size module in 2007 (see Section 8.3).

5.4.3 Quality Assurance

As in every series production of a high precision product, comprehensive quality assurance is a key ingredient for success. All phases of the project have to be coherently included, from the components (fibres, mechanical structures, photodetectors) over the production sequence to the final testing procedure. We summarize the main quality assurance steps:

- Fibres
 - a. Batch qualification after reception on statistical basis: light yield, light attenuation length, geometry (total and cladding thickness, shape, uniformity), bending characteristics
 - b. Aluminium side coating: adhesion, optical opacity, geometrical changes due to thermal load
 - c. Aluminium end coating: adhesion, optical reflectivity
- MAPMT
 - a. Quantum efficiency
 - b. Charge gain and gain uniformity over the 64 channels
 - c. Cross-talk
- Structural components
 - a. Geometrical parameters, tolerances
 - b. Machining and surface quality
 - c. Cleanliness

- Detector assembly
 - a. Various metrological controls as described in previous section
 - b. Temperature cycling of final module by ± 10 K around operational temperature
- Final lab test
 - a. Exposure to radioactive source (Sr-90) and comparison of light yield with reference detector (previously calibrated in test beam)
 - b. Integration test. Verification of fibre connectors and mechanical mounting

All tests are documented and the results stored in a database which allows to keep track of all fabrication and testing steps.

5.5 References

- 5-1 N. Mokhov, private communications.
- 5-2 UA4 Collaboration, R. Battiston et al., “*The Roman Pot Spectrometer and the Vertex Detector of Experiment UA4 at the CERN SPS Collider*”, Nucl. Instr. and Meth. A 238 (1985) 35-44.
- 5-3 C. Augier, “*Mesure de la partie réelle de l’amplitude de diffusion élastique proton-antiproton vers l’avant, à l’énergie dans le référentiel du centre de masse de 541 GeV*”, Thesis, Université Paris-Sud, no d’ordre 2609 (1993).
- 5-4 D0 Collaboration, V.M. Abazov et al., “*The upgraded DØ detector*”, Nucl. Instr. and Meth. A 565 (2006) 463-537.
- 5-5 A. Braem, C. Joram and P. Wertelaers, “*ATLAS Luminosity Detector - Simplified computations on thermo-mechanical straining of the fibre planes*”, ATLAS Note, ATL-LUM-PUB-2006-002 (2006).
- 5-6 Z. Ajaltouni et al., “*Study of Multianode Photomultipliers for the Electromagnetic Calorimeter Preshower read out of the LHCb Experiment*”, Nucl. Instr. and Meth. A 504 (2003) 9-13.
- 5-7 D. Renker, “*Geiger-mode avalanche photodiodes, history, properties and problems*”, Nucl. Instr. and Meth. A 567, 2006, 48-56 (2006).
- 5-8 A. Braem, A. Folley, C. Joram, L. Kottelat, “*Characterization studies on scintillating fibres*”, ATLAS Note, ATL-LUM-PUB-2006-004 (2006).
- 5-9 A. Braem and C. Joram, “*Fibre tests for the ALFA detector with a lab set-up using a Sr-90 source*”, ATLAS Note, CERN-ATL-LUM-PUB-2006-003 (2006).
- 5-10 J. Santos, J.G. Saraiva, Y. Nunes, A. Wemans, A. Maio, M.J.P. Maneira, “*Aluminization of Scintillating Fibers for the Luminosity Detector of ATLAS*”, ATL-COM-LUM-2007-001 (2007).
- 5-11 J.G. Saraiva, A. Wemans, M.J.P. Maneira, A. Maio, J. Patriarca, “*The aluminization of 600 k WLS fibers for the TileCal/ATLAS/LHC*”, IEEE Trans. Nucl. Sci. 51 1235-1241 (2004).
- 5-12 E. C. Aschenauer et al., “*Testrun results from prototype fiber detectors for high rate particle tracking*”, Nucl. Instr. and Meth. A 424 (1999) 459-469.
- 5-13 E. C. Aschenauer et al., “*Measurements of the radiation hardness of selected scintillating and light guide fiber materials*”, physics/9907018, DESY-99-078 (1999).
- 5-14 M. Glaser et al., “*New irradiation zones at CERN-PS*”, Nucl. Instr. and Meth. A 426, 72-77 (1999).

- 5-15 A. Mapelli et al., “*Development of a detector (ALFA) to measure the absolute LHC luminosity at ATLAS*”, presented at the 10th International Conference on Advanced Detector and Particle Physics, Como, Italia, 2007.
- 5-16 C. Joram, H. Stenzel, A. Braem, “*Basic Considerations on the Overlap Detectors of the ATLAS ALFA system*”, ATLAS Note, ATL-COM-LUM-2006-009 (2006).
- 5-17 A. Braem, C. David, A. Folley, C. Joram, L. Kottelat, A. Mapelli, M. v. Stenis, H. Stenzel, and M. Szauter, “*Design, Construction and Metrology of Prototype Overlap Detectors for the ALFA System*”, ATLAS Note, ATL-COM-LUM-2006-008 (2006).
- 5-18 A. Mapelli, “*Magnetic shielding studies for the ALFA MAPMTs*”, ATLAS Note, ATL-COM-LUM-2007-007 (2007).
- 5-19 MAFIA, CST Ltd., Darmstadt, Germany (www.cst.de).
- 5-20 V. Vorobel, H. Stenzel, “*GEANT4 simulation of the testbeam set-up for the ALFA detector*”, ATLAS Note, ATL-COM-LUM-2006-006 (2006).
- 5-21 A. Braem, C. Joram, A. Mapelli, A. Kocnar, J. Pospichal, “*Metrology results of the ALFA 2006 prototype detectors*”, ATLAS Note, ATL-LUM-PUB-2006-007 (2006).

6 The ALFA read-out electronics

6.1 Introduction

The average detected signal amplitude for a proton traversing 0.5 mm scintillating fibre will be in our case of the order of 4 photoelectrons (see Section 5.3 and Figure 8-1). The Hamamatsu MAPMT photo-detector R7600 has a typical charge gain of $0.5 \cdot 10^6$ leading therefore to signals at the input of the amplifier of 0.3-0.6 pC. The R7600 has 64 practically independent channels outputs. The metal channel dynode technology used leads to limited gain uniformity. The gain ratio between the strongest and weakest channel is typically 3 to 1. In addition, the average gain between two MAPMTs can also vary within a factor of 2. The inter-channel cross-talk at the output of the MAPMT, including optical effects in fibre detector itself, is below 3%.

An analogue readout scheme, as used during the test beam at DESY (see Section 8.1), has a number of clear advantages compared to a binary readout. The channel-to-channel gain variations could be compensated by off-line threshold cuts. The same holds for the gain differences between MAPMTs. The cuts can be carefully tuned in order to achieve an optimum balance between detection efficiency and noise related effects. On the other hand, an analogue scheme leads to more complexity, data volume and required bandwidth and finally to higher cost.

However, for the reconstruction of the tracks in the fibre detector, the knowledge of the fibre hit is sufficient, as long as the fraction of cross-talk and the induced noise are maintained small. The results from the test beams show that those conditions are fulfilled. We have therefore chosen a binary readout system.

Taking into account the above and the fact that we have limited space and difficult access conditions, the main requirements of the ALFA read-out electronics are determined by:

- Channel-by-channel adjustable amplifier gain to compensate for the MAPMT gain spread.
- High speed: it must be possible to associate signals unambiguously with a LHC bunch crossing.
- Adjustable threshold with a minimum setting of < 0.5 p.e. in order to guarantee high detection efficiency. A common threshold for 64 channels is acceptable if the gains can be adjusted (see above).
- Negligible cross-talk between channels: $< 3\%$.
- Compliance with standard ATLAS read-out scheme.
- Integration and Compactness: the restricted space in the Roman Pot environment requires to design a front-end electronics which is highly integrated, i.e. which deals with the 64 channels of one MAPMT, and which can be mounted directly on the back of the MAPMT, respecting the 40 mm grid of the MAPMT arrangement on the pot.
- Reliability and robustness: the Roman Pot detectors are located in the LHC tunnel, about 240 m from the ATLAS cavern, making interventions extremely difficult. The electronics moves together with the Roman Pots between beam and 'garage' position. Although these motions are foreseen to be smooth and slow, the mechanics and connectivity of the read-out system must be designed such that a reliable and robust operation can be guaranteed over extended periods.
- Radiation tolerance: the radiation environment during the specific luminosity runs is not expected to pose serious problems for the electronics. In normal physics runs, once the LHC machine is operated at close to nominal luminosity, the scintillating fibres would soon suffer from radiation damage, and, at a lower degree, the electronics could be degraded as well. It is therefore foreseen to

dismantle and remove the detectors and the electronics parts from the pots. The connectivity of the system must allow for a rapid removal/installation of the system.

6.2 System description

The first part of the readout system is schematically shown in Figure 6-1. This part of the electronics readout is located on a stack of printed circuit boards (PCB) located atop of each PMT tube. The assembly of the PMT with the PCB, connectors and all components is named PMF. Inside a PMF, each PMT anode is connected to the input of one channel of the 64 channel readout chip MAROC (see Section 6.4). The PMT signal is amplified and shaped. The signal amplitude is compared to a threshold. If the amplitude is higher than the threshold, the output of the channel is set to a logical “one”, otherwise the output stays to logical “zero”.

The 64 outputs of MAROC are connected to an FPGA type readout chip, named ALFA-R. The simplified block diagram of ALFA-R is also shown in Figure 6-1. ALFA-R samples at 40 MHz the outputs from MAROC, stores the logical states for about the L1 latency delay, then drops the data if there is no positive trigger signal at the L1 delay, or pushes the data onto the readout buffer if there is a positive trigger signal at the L1 delay. The data of the readout buffer is transmitted serially out to the motherboard under the control of a couple of handshake signals with the receiving MotherBoard.

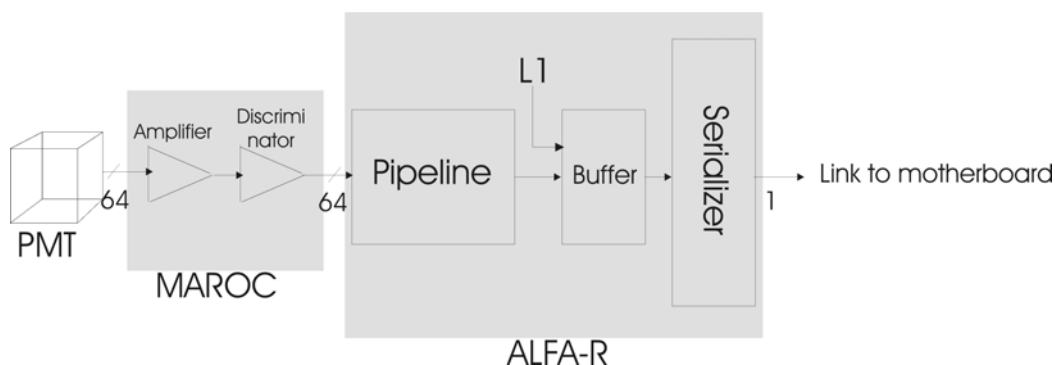


Figure 6-1 Generic description of the readout scheme of the PMT tube.

The second part of the readout system is the MotherBoard, whose block diagram is presented on Figure 6-2. The MotherBoard (one per Roman Pot) is able to receive the serialized data from 23 PMF units, reading out 1460 channels. The data is stored in registers and rearranged in the ALFA-M FPGA to provide parallel 32-bits words which are transmitted to a fast serializer. The data is sent off the Roman Pot through an optical link running at 1.28 Gbits/s. The readout time for all PMTs channels is less than 1.5 μ s, well below the minimum delay between consecutive triggers.

The MotherBoard is synchronized to the central ATLAS TTC processor. The bunch crossing clock and L1 trigger signals are received through an optical link. The control of the Motherboard and of readout chips on the PMF is done through an ELMB [6-1] unit controlled by DCS software. The Motherboard also provides the amplification and adaptation circuits for transmission of the three trigger counters signals.

The third part of the readout system is made of the elements located in the USA15 cavern. They are standard to the ATLAS equipment. A TTC access point, dedicated ReadOut Driver cards (ROD), connexion to the central trigger processor (CTP), control through the DCS system, are the main elements (see Chapter 7). The high voltage power supplies for the PMT elements will be located in USA15. The low

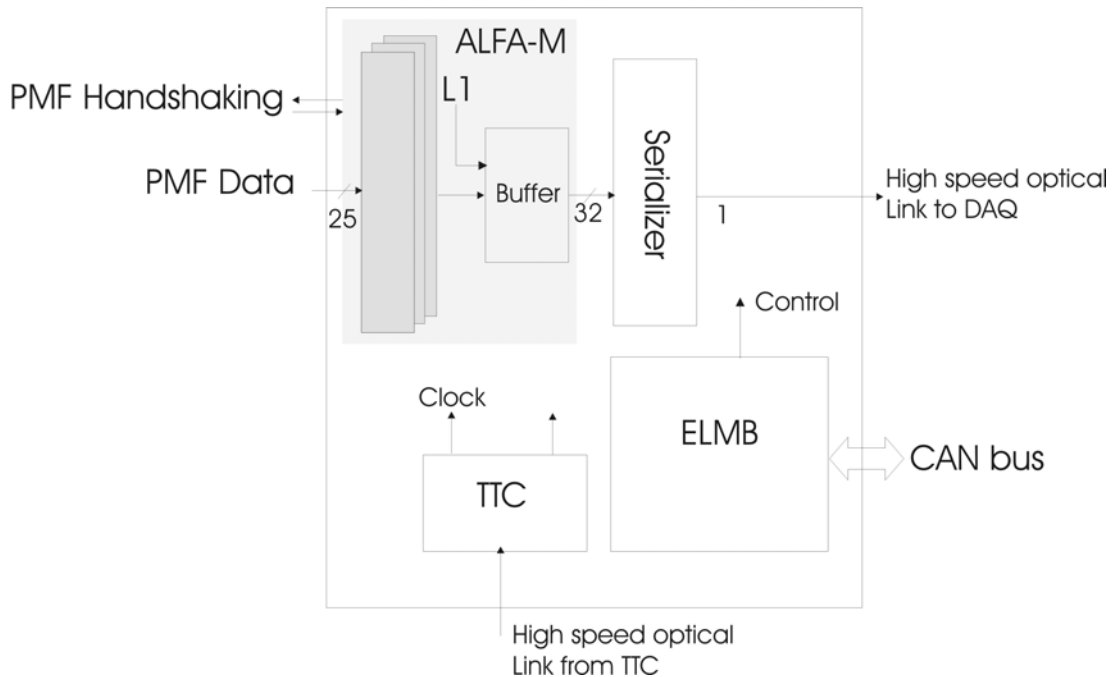


Figure 6-2 Simplified function diagram of the motherboard.

voltage power supplies for the powering of the electronics will be located in the nearby alcove inside the LHC tunnel, within 30 m of the Roman Pot stations.

6.3 Roman Pot station overview

Figures 6-3 and 6-4 show how the MAPMT's and the PMFs will be arranged on the top of the upper pot. There are 25 identical locations organized in a 5 x 5 matrix structure. In each structure there is room for a PMF (3 cm x 3 cm x 6 cm) consisting of one MAPMT, 3 PCB's and a connector. Totally there will be 1280 channels per pot for the main detector and 180 for the overlap detector. The total number of channels can be covered by 23 PMF's. One of the remaining slots in the 5 x 5 array will be used for the feedthrough connections for the 3 single channel small PMT used to read the trigger counters (see Section 5.2.4).

The Motherboard (MB) is sitting close to the PMF array. It collects the data stream out of the 23 PMFs and concatenates all the data before sending through a high speed optical serial link. Other functions of the MB are described in more details in the Section 6.6.

The electronics in the Roman Pot is designed to minimize the number of services. The connectivity to the outside will be limited to the high voltage inputs (one per PMT), the power supply cables (5 V and 12 V), two optical links for data transmission, a specific air core cable and two standard cables for the trigger counters signals and a low speed CAN bus for communication with the ELMB [6-1] controlling the front-end electronics setup.

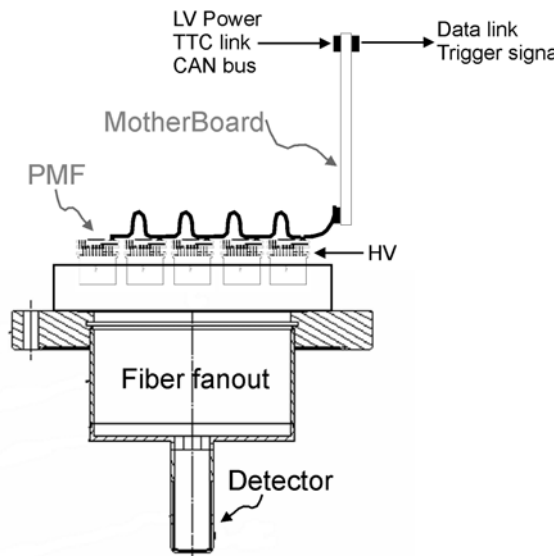


Figure 6-3 Electronics parts in the Roman Pot station.



Figure 6-4 View of the distributed PMF elements on the pot structure.

6.4 MAROC Front-End chip

MAROC, for Multi Anode ReadOut Chip, is the readout chip designed for the ALFA detector [6-3]. This ASIC is an evolution of the OPERA_ROC ASIC [6-2] developed and used in the OPERA experiment to auto-trigger and readout 32 channels Hamamatsu MAPMTs. The first beam tests of the ALFA detector using this chip were carried out at DESY in 2005 and are summarized in Section 8.1. The MAROC chip is expected to discriminate the 64 channels of the MAPMT and to produce 64 corresponding trigger outputs. The chip will also be used for other applications (the LUCID detector and medical imaging applications) that in addition request a charge measurement. For test purposes this could also be useful for our application.

The MAROC chip is required to have a detector efficiency of 100% for signals larger than $1/3$ photoelectron. This corresponds to a charge of 50 fC for a PMT functioning at a gain of 10^6 . The noise is expected to be less than 2 fC. The crosstalk between neighbouring channels should be better than 1%. Additionally the charge measurement should be feasible up to a signal of 30 photoelectrons with a linearity of 2%.

The final version of MAROC is expected to be the third iteration of this ASIC. The first version (MAROC 1) was respectively submitted and received in June and October 2005. It was thoroughly tested in order to check its performances [6-3]. This version of the chip was used during beam tests in autumn 2006 at CERN. A detailed description of it is given in the Section 8.2. Few problems were discovered and are cured in the second version (MAROC 2). This second version was submitted in March and received in July 2006. It incorporates some extra features which are used for the other applications. The rest of this section will be dedicated to the description of MAROC 2 which is close to the final version [6-4]. Some test results will also be presented.

MAROC 2 has been designed using the AMS SiGe 0.35 μm technology. The package used is CQFP240. The area of the chip is 15.6 mm^2 (4 mm x 3.9 mm).

Figure 6-5 represents the block diagram of the ASIC. The chip has 64 “super common base” inputs, 64 trigger outputs, an analog and a digital multiplexed charge output. Each channel is made of a variable

gain preamplifier with low input tunable impedance (50-100 Ω), a low offset and a low bias current (20 μA) in order to minimize the cross talk. This variable gain allows to compensate for the PM gain dispersion up to a factor 4 to an accuracy of 6% with 6 bits digital control. The amplified current feeds then two paths:

1. A slow shaper path which consists in a CRRC² shaper and two Sample and Hold Widlar differential buffers. These two S&H (1 and 2) blocks can measure and then store the baseline and the charge in a 2 pF capacitor. Finally an analog multiplexed charge measurement is delivered with a 5 MHz readout speed. The option of reading out the analogue amplitude of signals through this multiplexer is maintained for the commissioning of the detector. This feature is not used during normal operation. Figure 6-6 shows slow shaper waveforms obtained for a fixed preamplifier gain of 16 and an injected input signal varying from 50 fC to 2 pC.

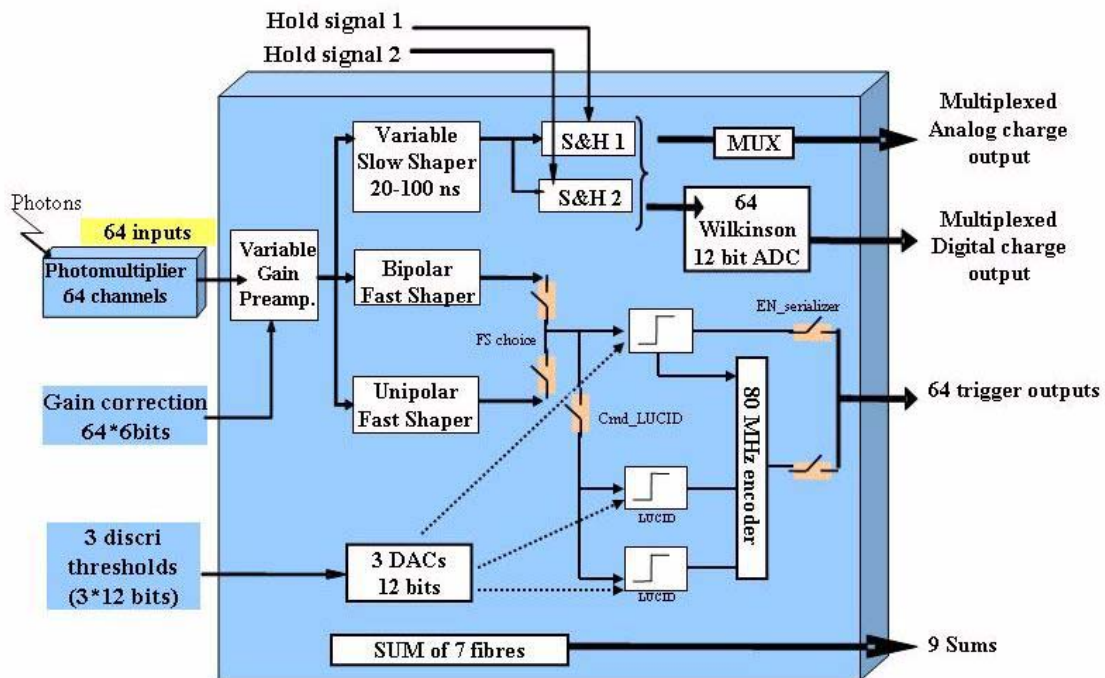


Figure 6-5 Block diagram of MAROC 2.

2. A fast (15 ns) shaper path with two possible fast shapers selected by the register FS_choice and followed by one discriminator (low offset comparator) that delivers the trigger output. The threshold is set by an internal 10 bit DACs composed by a 4 bits thermometer DAC allowing coarse tuning (200 mV per step) and a 6 bits mirror DAC used for fine tuning (3 mV per step). Figure 6-7 represents the trigger efficiency as a function of the injected charge (S-curve) obtained with the unipolar fast shaper for 32 channels all set at gain 1. The threshold was the same for each channel. As required, the 100% trigger efficiency is reached for an injected charge of 50 fC. It can even go down to approximately 20 fC. The dispersion of the 50% trigger efficiency point is equal to 2.5 fC rms.

On the block diagram of Figure 6-5 are also shown other blocks (a 12 bit Wilkinson ADC, additional discriminators, summing circuitry) which are not used in the ALFA detector.

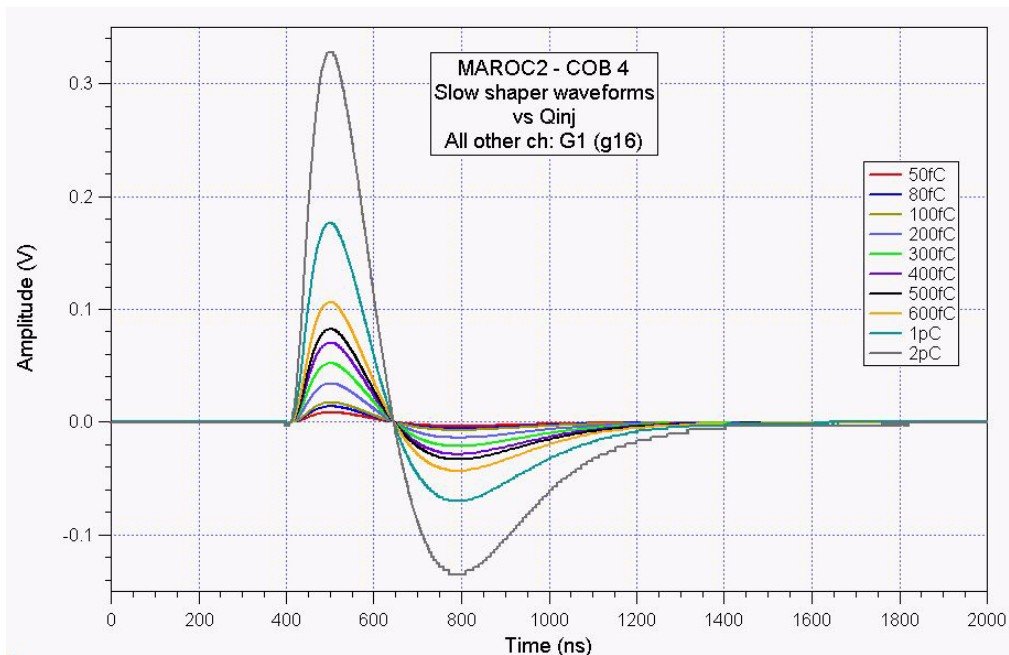


Figure 6-6 Slow shaper waveforms obtained for a variable injected charge (50 fC to 2 pC) and a fixed preamplifier gain.

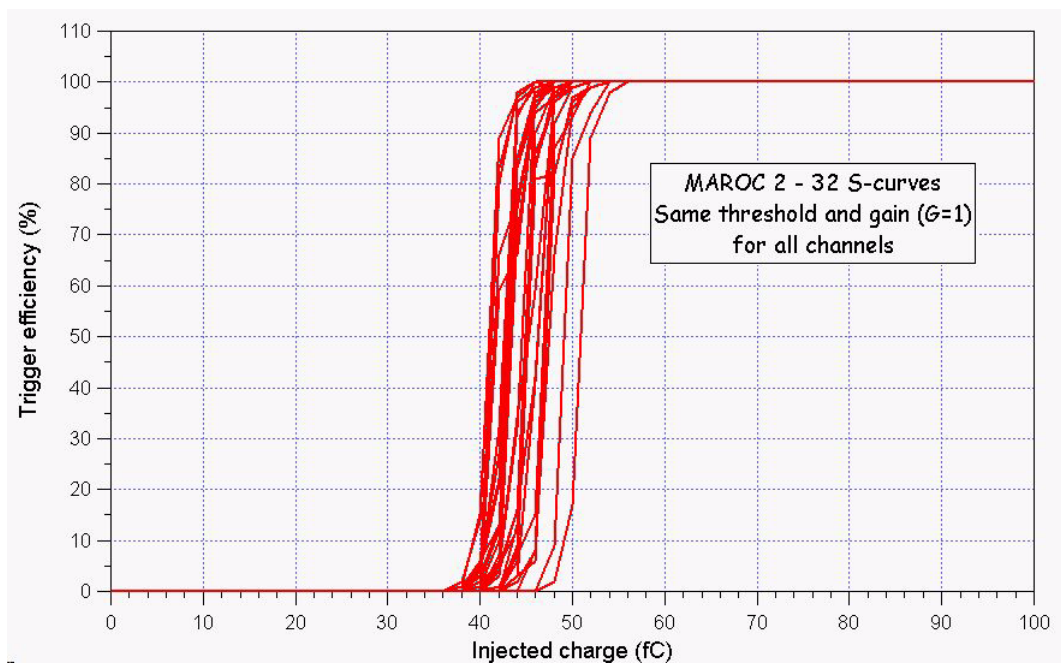


Figure 6-7 Trigger efficiency as a function of the injected charge (S-curve) for 32 channels of a MAROC 2 ASIC.

6.5 PMF

The PhotoMultiplier Front-End board, PMF is made of three sandwiched printed circuit boards with a side of $30 \times 30 \text{ mm}^2$ (Fig. 6-8). All three boards also contain a $3.5 \times 6 \text{ mm}^2$ hole to sustain the vacuum glass pipe from the PMT

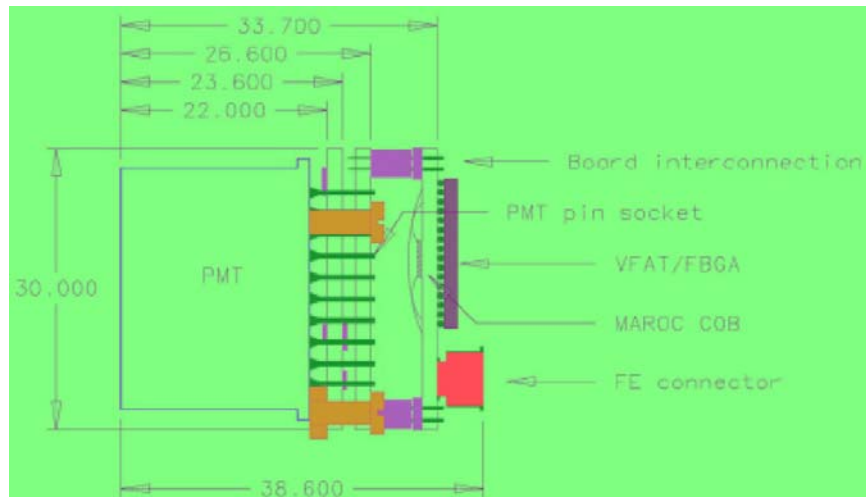


Figure 6-8 The PMF stack : the PMT case and the three PCB.

The board which is seated closest to the PMT case contains the voltage divider for the Hamamatsu R7600 Photomultiplier tube (HV dynode board). The board is equipped with pin feed-through sockets allowing the board to be pushed up along the PMT pin and allow continued access to all PMT pins.

Since the footprint for the PMT more or less covers the entire base, an adaptor-board is necessary to free up the space below the pins to be able to use it for the electronics. Only the 64 signal pins of the PMT are connected to this board. The dynode pins are fedthrough unplated drill-holes alternatively cut off just below the HV-dynode board in order to reduce the risk of flash-over. The same sockets as for the HV-dynode board is used to avoid thermal stress on the PMT while soldering and to simplify service.

The third board (PMF active board) on top of the PMF stack holds the active readout components MAROC and the ALFA-R readout chip (Figure 6-9 shows the top layer of this active board). The MAROC chip is realized as a chip-on-board die with the die size of $3.5 \times 3.9 \text{ mm}^2$ containing 240 bond-pads. The ALFA-R chip is realized as custom software in a Lattice ispXPLD5768 non-volatile FPGA in a 256-pad/1mm pitch $17 \times 17 \text{ mm}$ FBGA. All input or output communications with the Motherboard are made with differential LVDS signals. The interface between ALFA-R and MAROC is based on the low voltage single ended GTL signal definition.

The PMF is built as a set of detachable parts to allow the easy placement of individual PCB or PMT elements during the assembly phase. Figure 6-10 shows the picture of one PMF used for the autumn 2006 test beam, where the electronics stack is visible on the left. The PMT casing is seen at the right of the picture. The MAROC chip is directly bonded on the hidden side of the PCB which also holds the FPGA package.

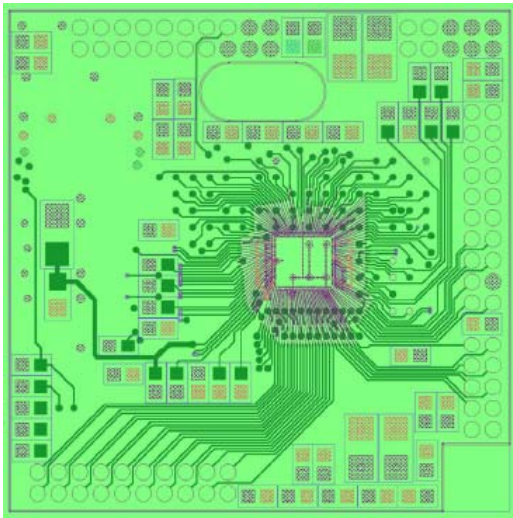


Figure 6-9 View of the active board layer with the MAROC chip printout.

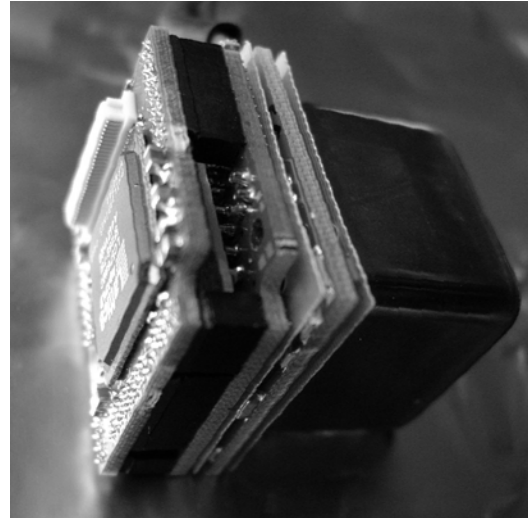


Figure 6-10 Picture of the actual PMF, with the electronics stack (left) and the PMT tube (right).

6.6 Roman Pot motherboard

6.6.1 Motherboard functionality

The Motherboard, as shown in Figure 6-11, provides :

- local power circuitry for the RP electronics
- Clock and L1 Trigger signal distribution through an optical connector, a pin diode and the TTCRx chip
- buffering of data received from 25 ALFA-R chips organised in 5 rows of 5 chips. The data are received at each L1 Trigger Accept (L1A), with a maximum rate of 100 kHz
- fast serialization of the data at each L1A signal using the GOL chip, a VCSEL driver, and the transmission through an optical link at 1.28 Gb/s
- slow communication channel using the ELMB unit to process the following operations :
 - Write Configuration data for the FPGAs (both ALFA-R and ALFA-M)
 - Write Control data for the electronics settings (like threshold value in MAROC chip)
 - Read back of Control data for the electronics settings and status registers.
 - Read monitored values like Power supplies, HV voltages etc...
- Fast Trigger counter signals shaping and buffering circuitry
- monitoring of MAROC slow shaper analogue outputs

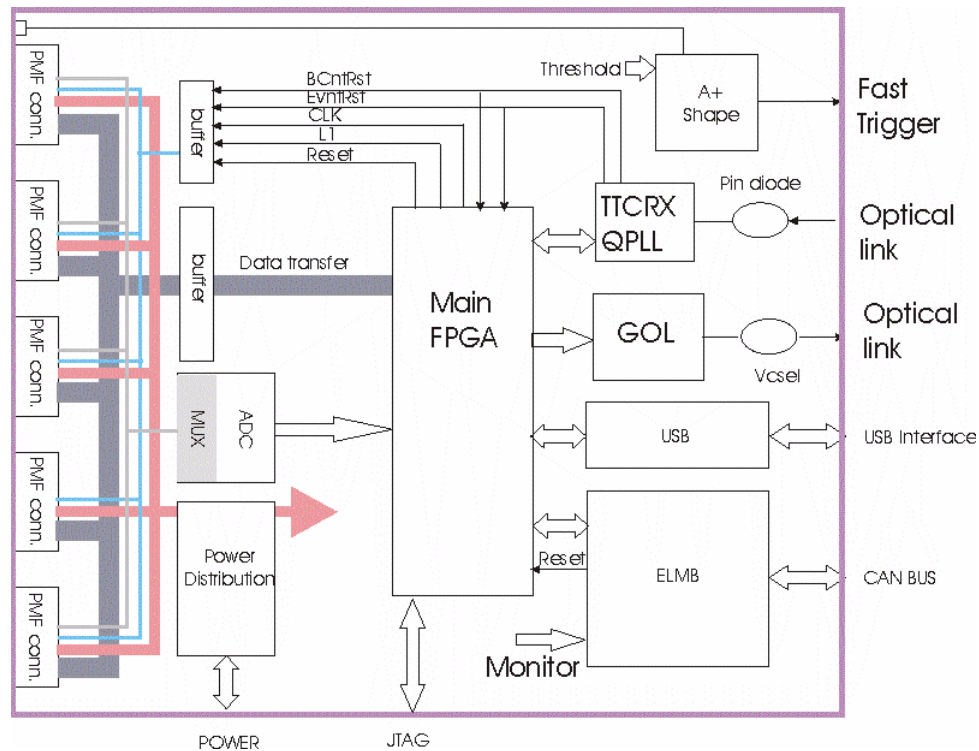


Figure 6-11 ALFA Motherboard main functional blocks.

6.6.2 Clock and L1 signals

The TTC signal with the encoded clock and trigger signals is received by a TTR-1B43 pin diode, followed by the TTCRx circuit, which provides the global clock and trigger signals to the board and PMF.

6.6.3 Data transfer

On reception of a L1 (positive trigger) signal, the data entered into the ALFA-R pipeline are transferred into a local buffer and at the same time each ALFA-R sends a signal (DataReady) to the FPGA ALFA-M on the Motherboard to mark that data is valid. Each ALFA-R waits an acknowledgement (DataReq) from ALFA-M and then sends serially a 40 Mbits/s flow made of a preamble with a BC counter and a L1 counter values, and then the content of the 64 channels data. The ALFA-M chip is able to accept in parallel the data from up to 25 PMF. The processing in ALFA-M is to store in registers the 25 PMF data stream, to check the preamble content, and then to rearrange the registers content into words of 32 parallel bits available at 25 ns rate on a bus outputs. These bits are transmitted to the GOL Gigabit link serializer [6-5] which has then the function to serialize 32 bits per 25 ns time slot (1.28 Gb/s) and control a VCSEL optical driver.

The data transfer durations from reception of one L1A signal are shown on Table 6-1. To compute the total data transmission time the processing time in each of the ASICs (MAROC, ALFA-R, ALFA-M) and the transmission delay time through the fibre length should be added. The target is to complete a full read-out sequence in less than 10 μ s, which corresponds to the average L1 rate in ATLAS.

Table 6-1 Data rate and transmission time for one event.

		Transmission rate	Transmission time
Number of bits from each PMF	73	40 Mb/s	1.825 μ s
Number of bits to transmit at L1A	23x64 + N overhead	1.28 Gb/s	1.149 μ s + Nx781 ps

6.6.4 Slow control

The other operation performed by the Motherboard is the electronics circuits settings and monitoring functions. For this purpose an ELMB [6-1] board is mounted as a piggy back component on the Motherboard. The ELMB is communicating with the distant DCS system through a CAN-bus interface. The communication is done with the appropriate cable and transmission rate to accommodate the long distance between the pots location and the USA15 control room. The ELMB is powered from the DCS box through the CAN cable, therefore the configuration and monitoring functions with the ELMB is possible independently from the status of the other electronics components. The local ELMB interface to the Motherboard is done through optoisolators, to prevent potential ground interference issues between the distant ELMB ground level and the local detector ground. The ELMB communicates with the standard DCS system, using routines developed in the common PVSS tools. On the board the ELMB is able to communicate with ALFA-M using a SPI interface. The ELMB can address registers in the ALFA-M or ALFA-R chips and send register content. In the other direction it is possible to read registers from these chips and upload the value to the control room. The setting of individual MAROC chip registers (threshold and gain settings) are also done through the ELMB.

The ELMB has one on-board ADC (Analogue-to-Digital Converter) which is used to monitor current and voltages on the Motherboard.

In addition to the above, the motherboard also provides the amplification of the signals from the trigger counters. Fast analogue amplification and line drivers are provided both for the fast trigger signals and for the overlap triggers (see Section 5.2.4).

6.7 Low voltage and high voltage power sources

The power consumption of one PMF unit with the active MAROC chip and the ALFA-R FPGA is estimated to 1 W maximum. The power consumption per pot, including the Motherboard and trigger counter drivers is calculated as 30 W. The main power is delivered to each pot by a 12 V and 5 V sources located nearby in the RR alcove. The Motherboard contains 10 LV4913 radiation tolerant voltage regulators to provide the 3.3 V and 1.8 V delivered to the 5 rows of PMF. Four additional regulators are used on board for powering the Motherboard components. High voltages for the photomultipliers are provided by standard high voltage sources located in USA15.

6.8 Radiation level

The ionizing dose at the radius where the electronics components are placed should be three order of magnitude less than what is quoted for the scintillating fibers (i.e. 10^2 - 10^3 Gy/year at a luminosity of 10^{34} cm^2s^{-1} and a distance of 20 cm). Scaling down this number with the effective luminosity for the ALFA tracker (10^{27} cm^2s^{-1}), the effective dose reduces to less than a milliGray. The commercial electronics components are well able to survive this environment. However, it is mandatory to remove the electronics of the roman pots when the machine running at high luminosity.

To take into account that the detector is operating in a radioactive zone, some key components of the electronics system are made with the available components which were specifically developed for the high radiation environment of the LHC experiments: the on-board voltage regulators, the TTC clock receiving circuit and the GOL data transmitters are all radiation tolerant. Furthermore some error detection or error correction circuitry will be implemented wherever possible in the FPGA parts of the PMF and Motherboard. The ELMB unit used to control and monitor the Roman Pot electronics is also qualified for the expected radiation levels.

The low voltage power supply units, located inside the tunnel, are of the type qualified for radiation levels up to 140 Gy and 10^{12} 1 MeV neutrons (this power units will stay in place during high luminosity runs).

6.9 References

- 6-1 B. Hallgren, H. Boterenbrood, H.J. Burckhart and H. Kvedalen, "The *Embedded Local Monitor Board (ELMB) in the LHC Front-end I/O Control System*", presented at the 7th Workshop on Electronics for LHC Experiments, Stockholm, Sweden, 10 to 14 September, 2001.
- 6-2 A. Lucotte et al., "A *front-end read out chip for the OPERA scintillator tracker*", Nucl. Instr. and Meth. A 521 (2004) 378-392.
- 6-3 P. Barrillon, S. Blin, M. Bouchel, T. Caceres, C. de La Taille, G. Martin-Chassard, P. Puzo, and N. Seguin-Moreau, "MAROC: *Multi-Anode ReadOut Chip for MaPMTs*", proceedings IEEE 2006.
- 6-4 P. Barrillon, S. Blin, T. Caceres, C. de La Taille, B. Lavigne, N. Seguin-Moreau, "MAROC 2 *datasheet*".
- 6-5 P. Moreira et al., "A *Radiation Tolerant Gigabit Serializer for LHC Data Transmission*", Proceedings of the 7th LEB workshop on Electronics for LHC Experiments, LEB 2001 Stockholm, Sweden , 10 - 14 Sep 2001 - pages 145-149.

7 The ALFA trigger and read-out

The main luminosity monitor of ATLAS will be the LUCID detector (LUMinosity measurement using a Cerenkov Integrating Detector [7-1]). The minimum requirement on the ALFA trigger and read out is thus that the ALFA detector and LUCID can operate together during the high β^* calibration runs. There are clear advantages from going beyond this and instead reading the whole ATLAS detector for events triggered by ALFA. It would allow flexibility in vetoing events with activity in the main detector and it would also allow to calibrate any other potential luminosity monitor.

In this chapter we consider both the possibility to integrate ALFA in the standard ATLAS TDAQ system and the minimum solution of reading only ALFA and LUCID. The first option is by far the most attractive and we will concentrate on this solution. The only reason that we also consider the minimal stand-alone solution is that we are at the limit of the trigger latency for the integrated solution.

7.1 Trigger and read-out overview

A general overview of the Roman Pot trigger and read-out path is illustrated in figure 7-1.

For the trigger formation a scintillator plate, located in each pot, will be used together with a dedicated PMT. The scintillator provides a fast trigger signal, with a typical rise time of a few ns, allowing at the same time an independent cross check of the detector efficiency and acceptance. The PMT output signal is fed into a wide band amplifier and is then sent through a fast trigger cable to the ATLAS CTP [7-2].

The Central Trigger Processor (CTP) will receive one trigger input signal per Roman Pot, giving a total of 8 inputs, which only carries the information if the trigger was active or not. The trigger logic using the Roman Pot trigger signals corresponds to coincidence combinations, which will be formed by the CTP. The main triggers for elastic events will be of the type, upper (lower) pot in left stations in coincidence with lower (upper) pot in right stations. In addition triggers with only upper (lower) pots in coincidence will be used to study background. In the scenario of an integrated operation mode also triggers including veto from other ATLAS systems could be formed in the CTP. Beside the luminosity measurement based on elastic scattering, the Roman Pots are also foreseen to be used for other studies at low luminosity. In this case the Roman Pot signals could be used in coincidence with other systems to form various triggers, like for example together with LUCID to trigger on single diffractive events etc.

The trigger and read-out system of the ALFA tracker is synchronized to the 40 MHz LHC clock according to the standard ATLAS TDAQ scheme. Whenever the signal in one MAPMT channel exceeds the de-

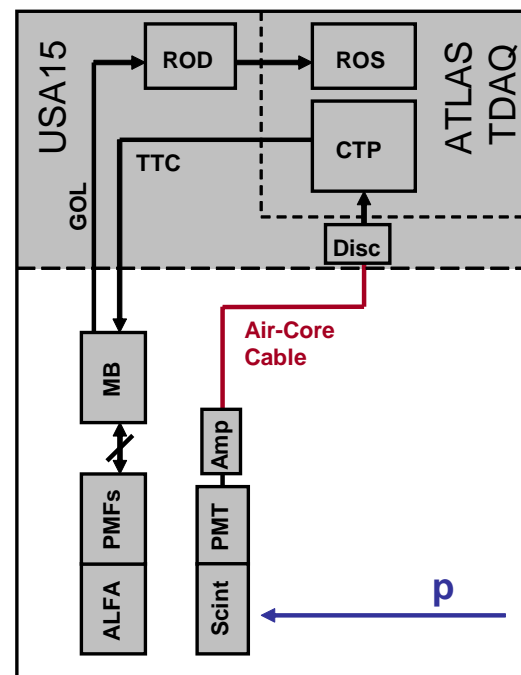


Figure 7-1 Trigger and read-out organisation of a single pot.

finer threshold of the discriminators in the MAROC chip, the channel is stored in the pipeline of the ALFA-R chip in the PMF. Upon receipt of a L1A signal, through the Timing, Trigger and Control system (TTC), the MB fan-out the signal to all the PMFs and the stored data from the corresponding bunch crossing is read and sent to the MB. After the data from all PMFs is collected the MB sends it through the Gigabit Optical Links (GOL) to the Roman Pot ROD (MROD type) which is the interface to the common ATLAS read-out system (ROS) [7-3]. The low multiplicity of the elastic events, where about 20 fibers (channels) per pot will be fired per event, combined with the low frequency of elastic interactions implies a low required bandwidth.

As described previously, the front-end electronics are located at the top (bottom) of the pot in order to keep the fiber length as short as possible. For the electronics located in this region, standard components can be used due to the low radiation level during the special runs and no cooling will be required.

7.2 Trigger infrastructure and integration with ATLAS

Due to the 240 m distance between the Roman Pots and the ATLAS Interaction Point, the trigger latency is very critical. In order to be in time with the ATLAS level-1 latency restrictions the analog signals from the trigger scintillators are foreseen to be sent, after amplification, directly to the counting room (USA15) where a fan-out unit will provide the signals both to the CTP and the back-end rack. The Roman Pot signals will both be used for local monitoring and be distributed to the LHC control room where the movement of the pots will be controlled.

7.2.1 The trigger scintillator for the ALFA tracker

The trigger for the ATLAS Roman Pot detectors will be based on a scintillator which is located inside the Roman Pot. The details of the trigger scintillator design and performances are described in Section 5.2.4. Figure 5-8 illustrates the available space inside the Roman Pot. It can be seen that the space for the trigger is very limited and for this reason the scintillator is restricted to a thickness of 3 mm. Since the sensitive area of the detector is large compared to the thickness of the trigger scintillator, the trigger detector design has to ensure an efficient light collection from the scintillator in order to obtain a high and uniform trigger efficiency over the whole area. The trigger scintillator is constructed by a diamond scintillator with exactly the same shape as the sensitive area of the tracker (see figure 5-8) and the light produced in the scintillator is collected by a light guide which is read-out by a small photomultiplier tube. The PMT will have to be located inside the secondary vacuum of the Roman Pot. It will be inserted through one of the unused fiber connector slots in the vacuum flange and neither the space nor the environment indicates any problems for this arrangement. The light guide solution gives less mechanical flexibility than an arrangement using wave length shifting fibers, but was on the other hand proven to provide a factor 5-10 more light to the PMT. That should hence be well above the critical level for a high and uniform trigger efficiency.

7.2.2 The trigger signal

The trigger pulse is produced by a photomultiplier tube from Hamamatsu model R1635. The PMT is operated at a gain of 10^6 from a bias of 1250V. The proposed arrangement gives an average photoelectric yield of 50 photoelectrons per pulse, and a trigger signal with an amplitude of 60 mV at 50 Ω and a full width at half maximum of about 4 ns. Before it is transmitted over the fast coaxial trigger cable, this pulse is shaped to reduce its bandwidth such that its amplitude gets proportional to the integrated charge delivered by the photomultiplier tube. The shaped pulse is also amplified to minimize the loss of signal to

noise ratio when driven on the 295 meter long trigger cable. The trigger signal will have a variable amplitude depending on the photons produced in the scintillators. To preserve the linearity of the shaped signal for this variable amplitude, a passive shaper will be implemented followed by a clamping amplifier able to drive the 50 Ω input impedance of the fast coaxial trigger cable, but also capable of fast recovery from saturated input pulses.

7.2.3 Trigger cable

The trigger signal transmission from the location of the Roman Pots to USA15 is the main contribution to the latency. Even at a signal transmission at the speed of light, the time margin with respect to the level-1 latency restriction is small and it is for this reason crucial that no unnecessary delays are introduced in order to arrive in time. The choice of trigger cable is therefore a fast foam dielectric coaxial cable rated for signal transmission velocity close to the speed of light [7-4]. The main characteristics of the trigger cable are summarized in Table 7-1 and a simulation was made of the effect from the cable on the trigger signal.

Table 7-1 Characteristics of trigger cable (AVA5-50, 7/8", HELIAX Coaxial Cable).

Characteristics	Values
Velocity (c)	0.91
Impedance (Z)	50 Ω
Capacitance (C)	73.2 pF/m
Inductance (L)	0.2 μ H/m
Resistance of Conductor (R)	1.35 m Ω /m
Conductance between signal and return wire (G)	10 pS/m

The trigger cable is a low-loss transmission line and has a wide frequency band (from 0.5 to 4900 MHz as given by the producer). The effect on the signal from propagation through the cable was studied using a Fast-Fourier Transform including the signal attenuation as a function of the frequency (given by the producer) and the signal dispersion approximated by

$$\beta \approx \omega \sqrt{LC} \left[1 - \frac{RG}{4\omega^4 LC} + \frac{G^2}{8\omega^2 C^2} + \frac{R^2}{8\omega^2 L^2} \right] \quad 7-1$$

Here ω is the angular frequency and the other quantities are given in Table 7-1. The study was made for a 295 m long cable using typical signal pulse shapes produced by the PMT and as expected the dispersion showed no significant effect. The effect was hence dominated by the signal attenuation and for a typical PMT signal with rise and fall times in a few ns the study indicated that the amplitude should be reduced to about 40% of the original value.

The possibility of having the analog trigger signal available in the ATLAS counting room is favoured since it contains information about the light yield of the trigger scintillator, but due to the relatively strong attenuation the PMT signal will be amplified, as described in the previous section, before transmitted through the trigger cable to USA15.

7.2.4 Interface to the CTP and the back-end electronics

The eight trigger signals from the Roman Pots will be provided to the CTP through the so-called CTP_CAL board. The CTP_CAL board allows for trigger signals, other than the main level-1 signals from the muon chambers and the calorimeters, to be connected to the CTP by standard LEMO cables. The CTP_CAL board requires 25 ns wide NIM signals as input and for this reason the shaped trigger signals, received through the trigger cables, have to be discriminated before being fed into the CTP_CAL module. To minimize the latency it is foreseen to discriminate and convert the Roman Pot trigger signals in the vicinity of the CTP.

Two discrimination methods are under study:

1. The shaped pulses are directly discriminated with respect to a threshold. A NIM pulse, 25 ns wide, is directly driven into the CTP_CAL. Because the amplitude of the input pulse is variable but the threshold is fixed, this can lead to some jitter in the NIM trigger pulse. This scheme can be implemented with off-the-shelf discriminator modules.
2. The shaped pulses are fed into a trigger preprocessor where they are sampled by a sample and hold circuit synchronously with the LHC bunch crossing rate. The sampled levels are synchronously discriminated with a fast comparator. The trigger NIM logic signals are synchronous with the LHC clock and are fed into the CTP_CAL module without jitter. In this scheme, a custom trigger preprocessor is required.

In both cases, the shaped trigger signals will be split before discrimination, allowing for monitoring or light yield measurements at the back-end electronics. The trigger NIM-logic signals will also be duplicated before they enter the CTP_CAL, and sent further to the CCC where the movement of the pots is controlled.

7.2.5 Trigger latency

To trigger the ATLAS detectors, the signal from the Roman Pots has to arrive to the ATLAS Central Trigger Processor (CTP) within 1.8 μ s in order to respect the overall latency (including L1A signal distribution to sub-detectors) of 2.5 μ s. Considering the trigger cable properties of Table 7-1 and a length of 295 meters for the installed trigger cable, our estimate for the Roman Pot trigger latency, is shown in Table 7-2.

Table 7-2 Estimated trigger latency.

Item		Time (ns)
Particle path from IP to RP	240(m) x 3.3357 (ns/m)	800
Signal treatment in local electronics	Shaper peaking time and driver	40
Signal transmission from RP to CTP	295 (m) x 3.666 (91% c) (ns/m)	1081
Signal treatment in USA15	Discrimination	20
	Total	1941

As expected, the main cause for the trigger latency is the signal transmission from the Roman Pot location to USA15. Included in the latency is a delay of 40 ns for the signal treatment in the local electronics and 20 ns delay for the signal treatment in the ATLAS counting room. As seen in the table, the trigger latency is about 1.9 μ s, which is just outside the value allowed by the L1 trigger system. However, the present L1

hardware is technically able to accommodate these extra 100 ns, since the interaction rate at the high β^* runs is much smaller than during normal high luminosity runs, and the available buffer space in the sub-systems exceeds the design requirements by a sufficient safety margin.

7.2.6 Trigger for the overlap detectors

The trigger arrangement for the ALFA overlap detectors is very similar to the one for the tracker. The trigger scintillators for the overlap detectors will also be read out by R1635 Hamamatsu PMTs and the signal will be driven to the ATLAS counting room as described above. Since the alignment procedure using the overlap detectors will be done independently of the other ATLAS systems it can be done in stand-alone mode and does not have to respect the L1 trigger latency. For this reason the main difference between the overlap detector and ALFA trigger schemes is that the overlap detector triggers are transmitted by conventional cables from the Roman Pots to USA15.

7.3 Timing, Trigger and Control

The Timing, Trigger and Control system (TTC) drives the clock and trigger signals to the Roman Pots front-end electronics. It is built with ATLAS standard modules and sits in the same electronics crate as the ROD.

The Roman Pots data is transmitted by the front-end to the RODs with gigabit optical links (GOLs) that impose some constraints for what concerns the clock stability. Because of this, a dedicated TTC clock generator (TTCclockgen) is used to produce the LHC clock with a jitter that is low enough to insure a reliable and error free GOL link.

The stabilised LHC clock drives the TTC controller module (TTCvi). This module receives also the L1A trigger signal from the CTP. The TTCvi formats two data frames, namely the channel A that embeds the L1A information, and the channel B that is used to transmit configuration parameters and commands to the front-end TTC receiver chips (TTCrx). To avoid instabilities in the clock received by the TTCrx chips, the channel B is not used in the Roman Pots. Therefore, the TTC optical fiber that is sent to the front end carry only the stabilised LHC clock together with the L1A signal.

The optical signal is produced by the TTCex module. It receives the A and B channels from the TTCvi and broadcasts the corresponding optical signal to eight output fibers.

7.4 Read-Out Drivers

The Read-Out Drivers (ROD) are in charge of collecting the data transmitted by each Roman Pot and of formatting standard ATLAS events that are passed to the ATLAS Read-Out System (ROS). Because there is only one data link per Roman Pot (eight in total), a currently existing ROD design will be used for the implementation of the Roman Pots ROD. The Roman Pot RODs must provide four GOL optical inputs running at 1.6 Gbps. The data format is based on 32 bits words, arranged in framed data packets. The collected data is binary without zero suppression. The ROD must be capable of collecting the framed packets from the four inputs for each L1A trigger, merge the data into a ROS compatible format and to transmit it over one S-link output running also at 1.6 Gbps. The ROD must also be implemented with programmable logic devices (FPGAs) allowing to reconfigure the firmware to suit the Roman Pot data format.

The MROD-X boards [7-5] developed for the ATLAS Muons Spectrometer were selected for this purpose because of its compatibility with the GOL transmission links and because of the possibility to customize the FPGA source code to fit the Roman Pots data format.

The MROD-X are 9U full depth VME boards, equipped with 6 GOL inputs each. For the Roman Pots ROD crate, two boards are used, each one servicing a group of four front-end links. The MROD-X is driven by the TTC clock over a custom made J3 backplane. This special backplane is driven by a Timing Interface Module (TIM) developed for the ATLAS Silicon Tracker (SCT) and already adopted by the ATLAS Muons Spectrometer. The processing of the data is handled by Xilinx FPGAs, and the status of the board is monitored and controlled by on-board DSPs. The formatted ATLAS events are then passed to an output S-Link interface that sits in the back of the crate. Two optical S-Link fibers are needed to interface the RODs with the Read-Out System (ROS).

7.5 Read-Out System

The ROS is a part of the ATLAS Dataflow system which receives data from the detector RODs, stores the data and make it available to the Level 2 Trigger (L2). When the ROS receives a L2 accept, it makes the data available for the Even Builder (EB), while it deletes the data not accepted by L2. The ROS is implemented using a collection of standard PCs (ROS units) housing a set of custom built PCI cards (ROBINs) that buffer the input data and multi-port Gigabit Ethernet cards that interface the ROS with both the L2 and the EB. On the software side the ROS consists of a multi-threaded object-oriented framework with a system of plugins. These ROS plugins are used for the interface with the trigger, the input and output data [7-3]. Each ALFA ROD will send, through its S-link connection to one ROBIN input of a ROS unit, a data fragment of 4928 bytes per event, including ROD header and trailer [7-6].

7.6 Detector Control System

The monitoring, configuration and control of the Roman Pots front-end is implemented by the ATLAS Detector Control System (DCS) and uses the Embedded Local Monitor Board (ELMB) [7-7] as front-end interface. This interface allows the monitoring and the configuration of all the front-end systems even in case of loss of the TTC clock. It is therefore possible to recover easily from unknown states with a DCS controlled reset signal and without cycling the power.

The DCS system allows resetting the front-end chips (FPGAs, TTCrx, GOL) using the ELMB digital outputs. The ELMB digital outputs are interfaced with the front-end motherboard using optocouplers.

The configuration of the front-end electronics and in particular of the PMFs is transmitted over CANbus to the ELMB that relays the data stream to the motherboard FPGA using the Serial Peripheral Interface (SPI) of the ELMB. The configuration and control commands contain an address field, which is decoded by the motherboard FPGA (ALFA-M). The data stream is transmitted by the ALFA-M to the corresponding PMFs if appropriate. If the data stream is addressed to the ALFA-M, it is processed on the motherboard and it is not relayed to any PMF. The Canbus link allows to read back important status flags and to verify some of the downloaded configuration parameters.

The ELMB is also used to monitor some electrical parameters of the front-end electronics such as:

- the HV levels distributed to the photomultipliers.
- the LV levels and currents as they are produced on the front-end motherboard.

- the temperature and vacuum status parameters for the secondary vacuum inside the pots

For these three points we intend to use equipment and software already developed for other sub detectors in ATLAS.

7.7 Alternative read-out modes

As mentioned above, two major operation modes are foreseen: standalone and integrated. The main features of the stand alone mode is described below. A backup scenario for the integrated solution, in case of problems with the L1 latency, is also discussed.

7.7.1 Stand-alone mode

For a trigger provided by the Roman Pots the read-out includes the Roman Pot detectors and LUCID. The trigger latency is not an issue as the pipelines for the luminosity detectors will be made deep enough.

An interesting variant of this mode would be to include the calorimeter trigger tower read-out as a whole or for some pre-defined configurations, i.e. few phi/eta locations. Again the trigger latency is not an issue since the L1 system has a pipeline buffer of $3.2 \mu\text{s}$ [7-2] which is within the Roman Pot trigger latency as explained in Table 7-2.

The stand-alone mode allows for calibrating the LUCID detector and the calorimeter towers during the special high beta runs.

7.7.2 Alternative integrated mode

An alternative integrated mode would be to have the CTP self (software) triggered and running at its maximum capacity of 75 kHz, respecting the dead time of the experiment and the filling scheme of the machine. Running in this way with 43 bunches in the machine implies omitting 6 out of 7 bunches and thus losing statistics. The method does not imply any hardware modifications. However, it is much less efficient than the standard integrated running mode.

7.8 References

- 7-1 ATLAS Collaboration, “*ATLAS Forward Detectors for Luminosity Measurement and Monitoring*”, Letter of Intend, CERN-LHCC/2004-010 (2004).
- 7-2 ATLAS Collaboration, “*Level-1 Trigger*”, Technical Design Report, CERN-LHCC/98-14 (1998).
- 7-3 ATLAS Collaboration, “*High-Level Trigger Data Acquisition and Controls*”, Technical Design Report, CERN-LHCC/03-22 (2003).
- 7-4 Andrew Corporation, AVA5-50, 7/8”, HELIAX Coaxial Cable.
- 7-5 MROD-X, <http://www.nikhef.nl/pub/experiments/atlas/daq/mrod/mrodpr>, <http://www.nikhef.nl/~peterj/MROD-X/MROD-X.html>.
- 7-6 ATLAS event format (see for instance <https://edms.cern.ch/document/445840/3.1>).

- 7-7 B. Hallgren, H. Boterenbrood, H.J. Burckhart and H. Kvedalen, “*The Embedded Local Monitor Board (ELMB) in the LHC Front-end I/O Control System*”, presented at the 7th Workshop on Electronics for LHC Experiments, Stockholm, Sweden, 10 to 14 September, 2001.

8 Test beam results and future activities

Two test beam experiments have been performed so far. The main goals of the 2005 test beam in the T22 area at DESY, Hamburg, were to prove the validity of the detector concept and to study the main detector characteristics. The 2006 test beam at CERN aimed at confirming the DESY results with larger fibre detectors and, in particular, with close-to-final readout electronics.

In the two performed test beam experiments, the available number of read-out channels (in 2005 we had 2 MAPMTs available = 128 channels, in 2006 5 MAPMTs = 320 channels) set limits for the prototype detector configurations which could be tested. Two detectors consisting of 10 staggered planes with 2×6 fibres (*ALFA 10_2_6*, 2005) and 10 staggered planes with 2×16 fibres (*ALFA 10_2_16*, 2006), respectively, were intended for spatial resolution studies. Larger detectors with 2 planes of 2×32 (*ALFA 2_2_32*, 2005) and 2×64 fibres (*ALFA 2_2_64*, 2006) were useful to study cross-talk between fibres and between adjacent channels on the MAPMT. In particular the last detector with 64 fibres per layer, whose design represents the current baseline, allowed to explore production and metrology methods. All of the above mentioned detectors were equipped with the baseline fibres. We also built several detectors with Bi-con single and double cladded fibres as well as 1×1 mm² fibres from Kuraray.

8.1 Prototype test at DESY

The focus of the DESY test beam was on characterising the key parameters of the detector concept like light yield (more precisely the photoelectric yield) of the fibres, cross-talk effects on various levels, detection efficiency, track reconstruction efficiency, spatial resolution and edge sensitivity. As a very detailed description of the set-up, analysis and results can be found in reference [8-1], we summarize just the main points.

The DESY T22 zone provides a low intensity electron (or positron) beam ($f \leq 1 \text{ kHz}$) of up to 7 GeV energy. The beam is collimated to a spot of about 1 cm² and has low divergence $\sigma_x \sim \sigma_y \sim 1$ mrad. A beam telescope consisting of three silicon microstrip detector stations (1 station before, 2 stations behind the detector under test) was used to predict the trajectory of the incident electrons. Its spatial resolution was in the range of 20 - 30 μm , depending on the amount of additional material in the beam. The MAPMTs of the ALFA detectors were read out in two different ways. High gain operation ($G \sim 5 \cdot 10^6$ at HV = 950 V) allowed to feed the analogue signals via a twisted pair cable directly into VME based charge sensitive ADC. Alternatively the signals were amplified, shaped and eventually discriminated by the OPERA front-end chip [8-2][8-3], a predecessor of the MAROC circuit which was used in the CERN test beam the year after (see below). The MAPMTs were then operated at typically half the above gain value. Custom designed readout cards housing two OPERA chips (32 channels/chip) were plugged directly on the output pins of the MAPMTs. The discriminated signals were handled by a FPGA mounted also on the cards and sent via USB link to a PC. The data taking rate was limited by analogue readout electronics of the Si-telescope (conversion time of the ADCs) to about 70 Hz.

8.1.1 Results

In the following we summarize the key results which were obtained with the 0.5 mm thick square shaped baseline fibres Kuraray SCSF-78. The photoelectric yield was extracted from charge amplitude measurements of the MAPMTs. The charge amplitude spectra were fitted by a Poisson distribution convoluted with a Gauss function.

$$Q(x, \mu) = A \cdot \sum_{0 \leq i \leq n} P(i, \mu) \cdot e^{-\frac{(x-x_i)^2}{2\sigma_i^2}} \quad 8-1$$

The response to single photons was previously determined for all MAPMT channels individually by exposing the photodetector to very low light levels from a pulsed blue LED. Apart from the trivial normalization A this provided the parameters x_I and σ_I , i.e. the position and width of the single photoelectron peak (in units ‘ADC counts’). The charge spectra obtained with the scintillating fibres (see Figure 8-1) were then fitted using $x_i = i \cdot x_I$ and $\sigma_i^2 = \sigma_0^2 + i \cdot \sigma_I^2$ with σ_0 being the width of the pedestal peak. Again, apart from the overall normalization, the photoelectric yield μ was the only free fit parameter. The spectra showed a small non-Poissonian excess of primarily single and very few double photoelectrons which could be attributed to cross-talk from adjacent MAPMT channels. This contribution could be quantified by simply adding a second Poissonian distribution with a small μ_{CT} cross-talk parameter $Q'(x, \mu) = Q(x, \mu) + Q_{CT}(x, \mu_{CT})$. The detected number of photoelectrons for our baseline fibre was 3.93 ± 0.18 (for fibres with a 45° cut) and 4.45 ± 0.50 (for fibres with a 90° cut). The agreement with the expected values is better than 5%. The relative cross-talk contribution $\mu_{CT} / (\mu + \mu_{CT})$ was $3.4 \pm 1.3\%$. It should be noted that this number represents the cross-talk which a given fibre receives from its 8 neighbours on the MAPMT, i.e. it depends also on the probabilities with which the 8 adjacent channels were hit. The actual cross-talk probabilities were extracted from this data and found to be 1.3% for direct and 0.4% for diagonal neighbours. Physics phenomena like δ -electrons and shower formation in upstream material led to a another cross-talk phenomenon which manifested itself in signals in adjacent fibres whose amplitude is comparable to the one in the leading fibre. Its contribution reached 3.7% for the direct neighbours, rapidly decreasing with the distance. The single fibre detection efficiency, from the p.e. yield, is expected to be above 98% (for an amplitude cut at 0 p.e.). It was studied independently using the Si-telescope to exclude events in the region $50 \mu\text{m}$ from the fibre edges. The observed efficiency confirmed the expectation for a cut of zero p.e. and dropped to about 92% for a cut of 0.9 p.e., which has been applied for the reconstruction studies.

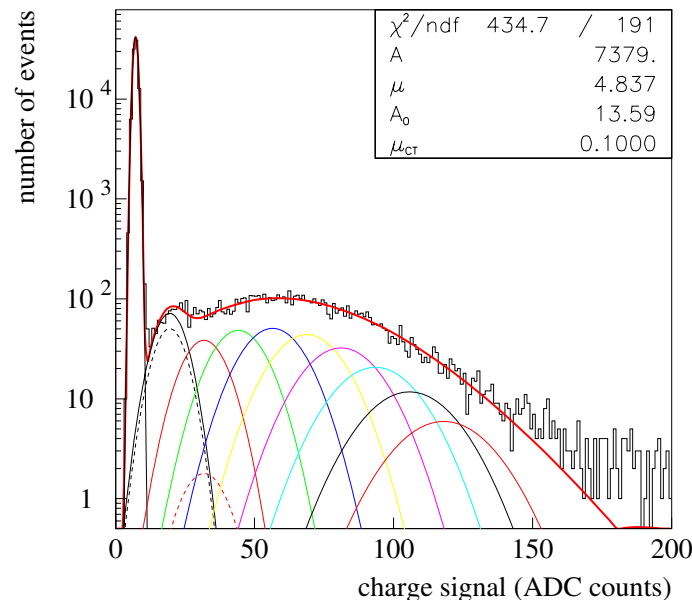


Figure 8-1 Photoelectron spectra from a 0.5 mm fibre (45° cut) obtained at 950 V. The average number of photoelectrons is 4.8, the cross talk term contributes additional 0.1 photoelectrons. The Gauss curves represent the $i = 1 \dots 9$ photoelectrons contributions. The dashed Gauss curves show the cross-talk term.

In order to investigate potential efficiency losses near the fibre edges, which could originate from insensitive cladding and glue remnants between fibres, a horizontal position scan was performed accumulating data in slices of 50 μm width. The efficiency was then evaluated in each of the slices, both for an entire plane consisting of six fibres and for individual fibres. The result for a fixed cut at 0.9 p.e. is shown in Figure 8-2.

For the impact point reconstruction an iterative algorithm based on the minimal overlap of the hit fibres in the U and V layers was developed which was also able to deal with layers with more than one hit. The algorithm relied on the actual position of every fibre, determined by metrology (see Section 5.4). Events in the detector *ALFA 10_2_16* produced on average 20.44 hits in 18.03 layers. As explained in Figure 8-3, the spatial resolution, after deconvoluting the resolution of the Si-telescope of 30 μm , was found to be 36 μm , both in x and y direction. As described in Section 5.3, this value is in excellent agreement with the GEANT4 studies. The reconstruction efficiency was 99%. Also the detector *ALFA 2_2_32* was used for resolution studies, in this case the MAPMTs were read out with the OPERA electronics [8-3]. A resolution of 73.8 μm could be measured, to be compared with $250 \mu\text{m} / \sqrt{12} = 72 \mu\text{m}$, expected from the effective detector pitch.

The sensitivity of the fibre detector at the fibre edge was studied by means of an additional small scintillator which touched the fibres from below and which was used to define the physical edge of the fibre ends. From the tracks passing either through the fibre detector or through the small scintillator histograms were produced of their vertical coordinate using again the Si-telescope information. As illustrated in Figure 8-4, the histograms were fitted by ‘smeared edge’ functions consisting of a Heavyside function convoluted with a Gaussian. Analysis of the edge positions revealed the absence of any non-active edge zone. The smearing of the edges was compatible with the spatial resolution of the Si-telescope.

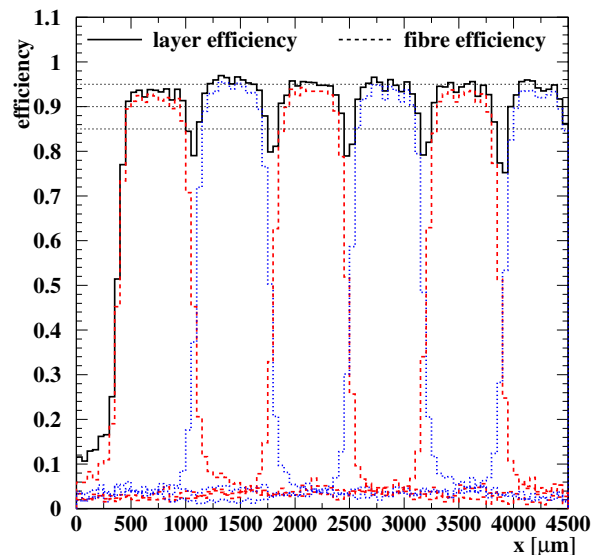


Figure 8-2 Layer efficiency (solid line) and fibre efficiency (dashed line) for a fixed cut of 0.9 p.e as function of the horizontal beam position.

The results of the DESY beam test clearly validated the detector concept, the construction method and the choice of the single cladded 0.5 mm square baseline fibre Kuraray SCSF-78. The applied fibre machining and coating techniques were found to be adequate for the required surface quality and reflectivity as was the geometrical precision obtained with the relatively simple tooling. All measured performance parameters match well the ATLAS requirements.

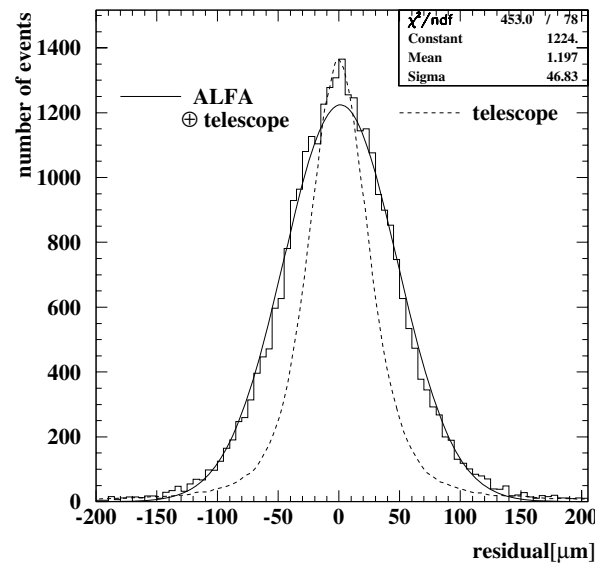


Figure 8-3 Detector *ALFA 10_2_6*. The residuals $x_{ALFA} - x_{telescope}$ (solid line) compared to the intrinsic resolution of the telescope (dashed line)

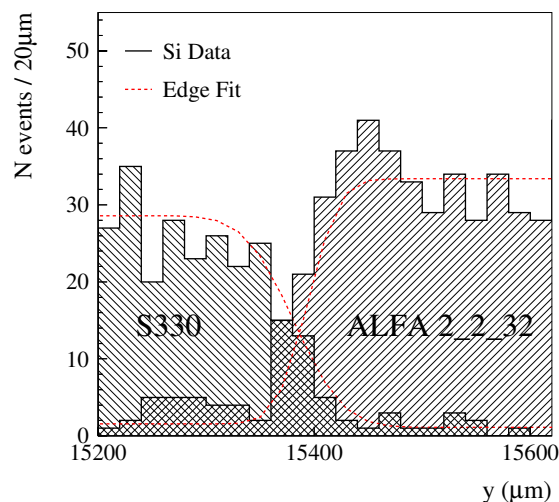


Figure 8-4 Comparison between the edges of the detector *ALFA 2_2_32* and the small trigger counter (*S330*). The histograms corresponds to the y -coordinate distribution of tracks measured by the Si-telescope. The dashed lines represent the smeared edge functions fitted to the histograms.

8.2 Prototype test at CERN

In October of 2006 the second ALFA beam test was performed at CERN in the North Area H8 beam line. Its main purpose was to validate the fibre tracker together with the proposed front-end electronics and readout system, as close as possible of the final implementation. For this test two new ALFA prototypes [8-4] were built with an increased number of fibres compared to the DESY testbeam. The first detector, called *ALFA 2_2_64*, included two planes which contained the full set of 64 fibres per layer. Since this detector had the full size of the final ALFA tracker it could be tested with a prototype of the final trigger

scintillator which will be accompanying the tracker in the Roman Pot. The challenge related to this trigger counter is the requirement of a very uniform trigger efficiency in order not to bias the measurement combined with stringent space limitations in the pot. The second ALFA tracker included all 10 planes with 16 fibres per layer (*ALFA 10_2_16*) and would hence allow for resolution studies. The H8 beamline delivers high momentum hadron beams (e.g. pions at 230 GeV/c) such that multiple scattering becomes marginal. In addition to the two ALFA trackers two overlap prototype detectors were built (see Section 5.2.3). They consisted of two staggered layers with 30 fibres each. Both detectors were placed in the beam and their relative position could be mechanically controlled to about 10 μm .

8.2.1 The electronics setup

A first model of the electronics system proposed for the ALFA detector has been installed and tested during a test beam period in October 2006. Figure 8-5 shows the diagram of the electronics system setup in the beam area.

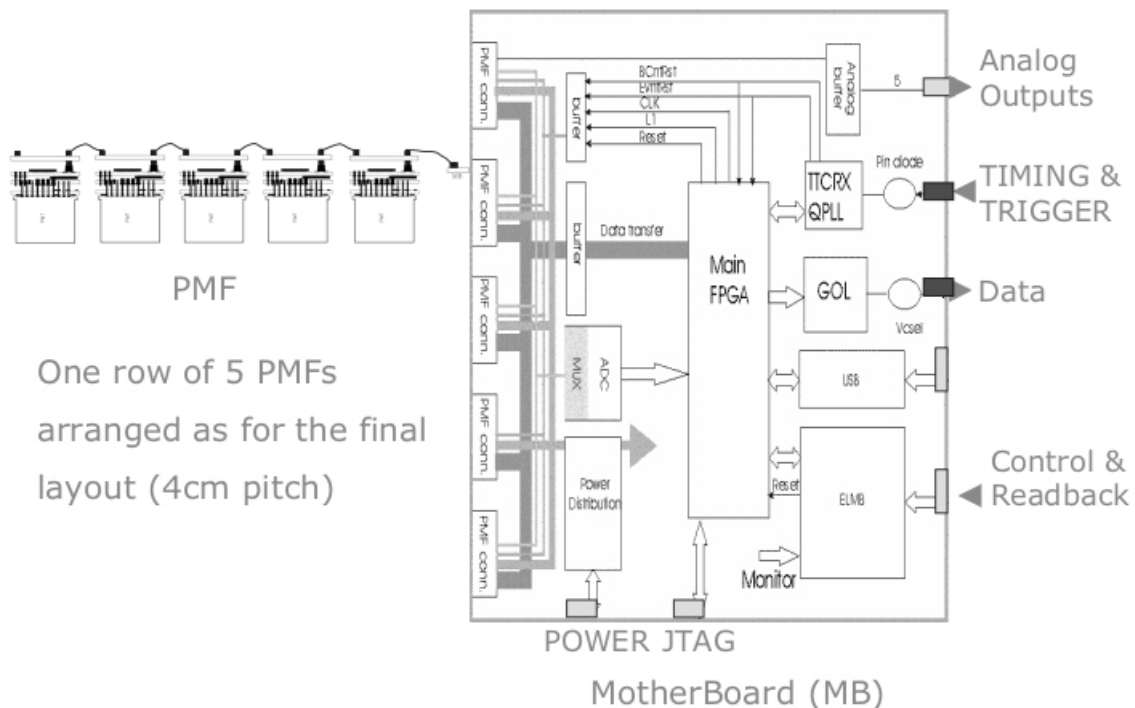


Figure 8-5 Electronics installed in the test beam zone.

The setup was made of 5 PMFs distributed in a row (as it is expected for the final implementation), and an initial version of the Motherboard, which contains all functions of the MotherBoard as described in Section 6.6.1, except the trigger counter signal circuits.

Figure 8-6 shows a photography of the setup, with the Motherboard in front and the cabling structure to distribute signals to the 5 PMFs. It should be noted that the interconnection between the Motherboard and the PMF will later on be made with light Kapton cables, to replace the large flat cable and adapters seen on this picture.

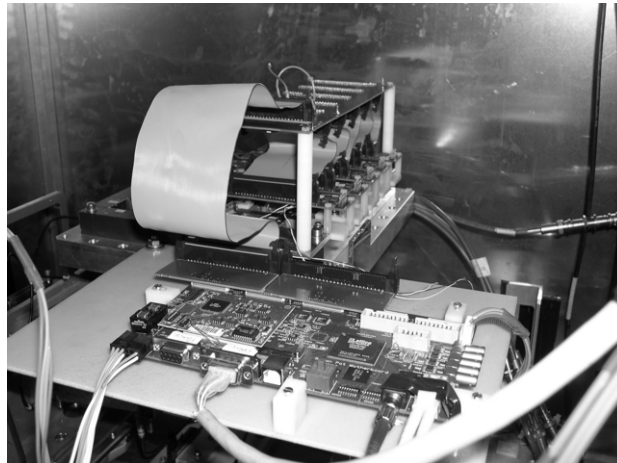


Figure 8-6 Front view of the test beam setup.

Figure 8-7 shows the setup from the side where the top of the PMFs are visible, with the connectivity arrangement for configuring and reading 5 PMFs. The PMTs are precisely placed inside the structure made to position them on the optical connectors receiving the ends of the detector fibers.

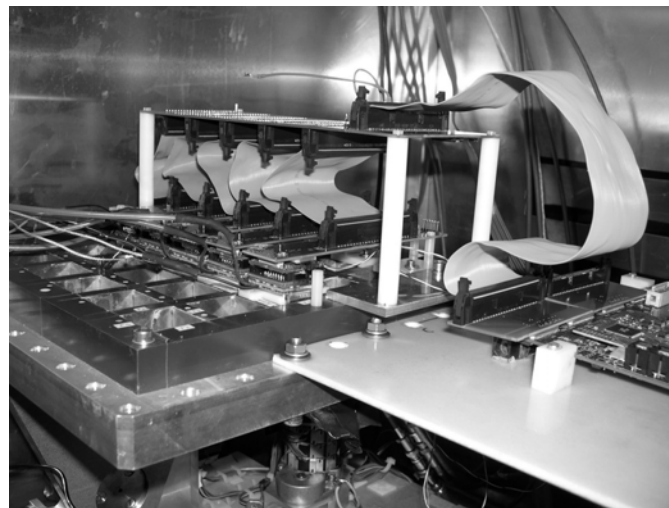


Figure 8-7 Side view of the test beam setup.

The readout arrangement in the counting room is presented in Figure 8-8. One computer with PVSS is used to configure the electronics installation in the test beam area, through a CAN bus. The readout PC is equipped with a FILAR [8-5] card to read data from the high speed optical link connected to the GOL chip on the Motherboard. The TTC signals are generated with the standard units of the TTC system for experiments and sent through an optical fiber to the Motherboard. It should be noted that the communication cables between the counting room and the setup in the beam area are one CAN-bus cable and two optical fibers, which is the exact arrangement proposed for the final installation of the ALFA detectors. These communication media are already adapted for the distance of about 300 m between the Roman Pot position in the LHC tunnel and the control and readout equipment in USA15. The other required hard-

ware between these two locations will be the high voltage supply cable bundle and the 3 trigger counter cables.

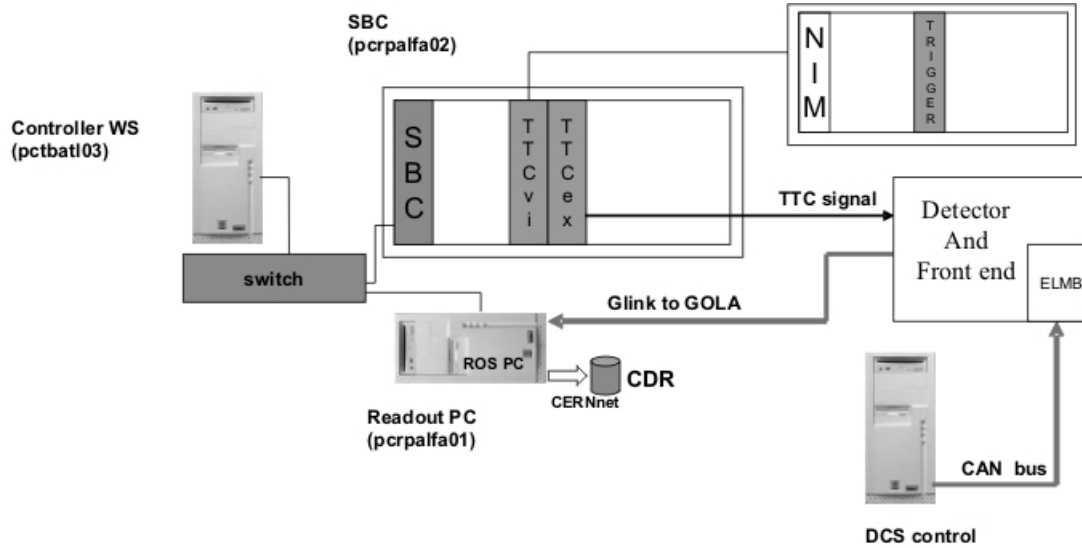


Figure 8-8 Diagram of the setup in the counting room.

8.2.2 Results

8.2.2.1 MAROC 1

The first version of the MAROC ASIC (see Section 6.4) was used in the PMF. The chip was submitted in June 2005 and received four months later. Its block diagram (see Figure 8-9) is simpler than the second version. It comprises a variable gain preamplifier, which is used to equalize the PMT gains, a variable slow shaper associated to a track and hold system that produces a multiplexed output charge and a bipolar fast shaper associated to 10 bits DAC discriminator that produces 64 trigger outputs.

Many tests were performed in the laboratory to check the performance of the MAROC chip before the decision was taken to use it in the beam test. These test are summarized in Figures 8-10, 8-11 and 8-12. Figure 8-10 shows how the gain was equalized and in Figure 8-11 the 100% efficiency for an injected charge of 50 fC is demonstrated. Moreover the cross talk was found smaller than 1%, as proven on Figure 8-12 which represents the S-curves of three channels. Only the central one was fed with signal. To trigger the side channels, one needs two orders of magnitude higher signal in the central channel.

8.2.2.2 Front-end electronics and readout

The system as shown in Figure 8-8 was fully operational during the beam period. As already mentioned, the readout PC was equipped with a FILAR card to read the data. The data was received from the detector and front end system through an optical link running at the target rate of 1.28 Gbits/sec. The data was framed with a rudimentary protocol to recognize pattern. For the final system, it is for seen to use a

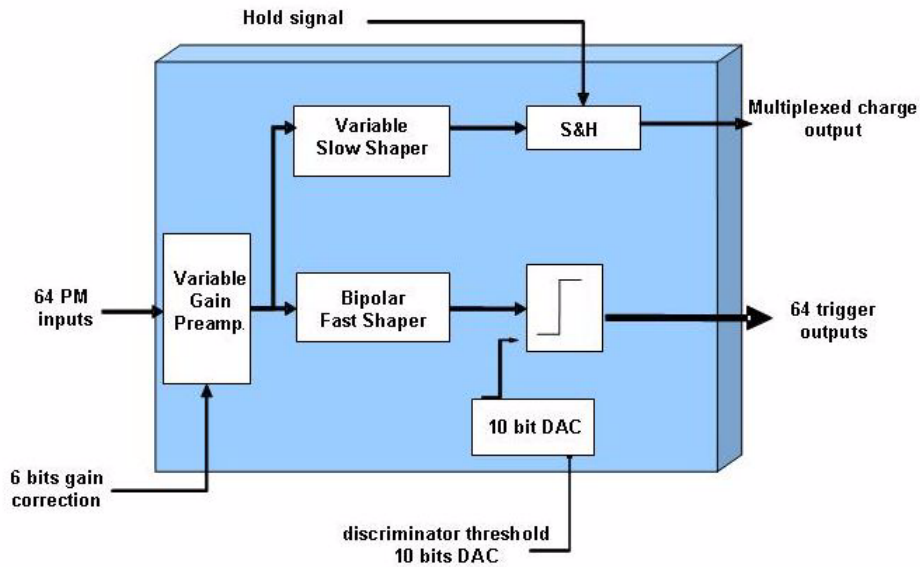


Figure 8-9 Simplified block diagram of MAROC 1.

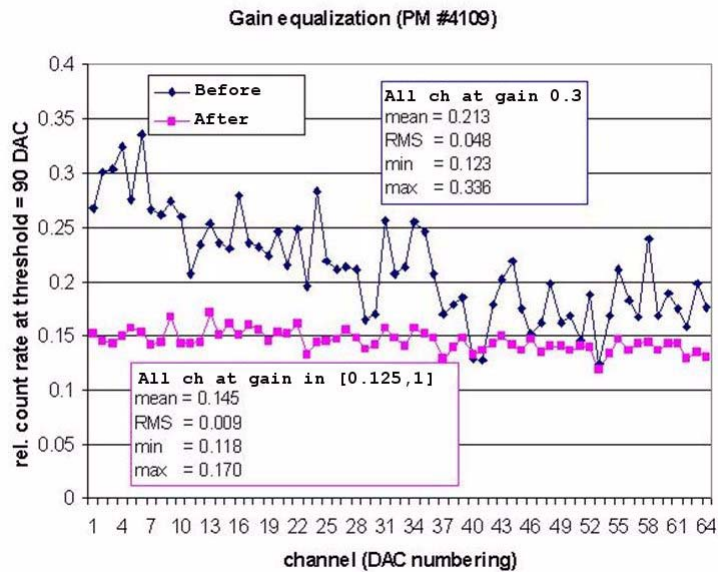


Figure 8-10 Relative counting rate before (blue diamonds) and after (pink squares) the PMT gain equalization. The PMT was exposed to the light of a LED. Horizontal scale in channel numbering.

MROD-X card (see Chapter 7) instead of the FILAR card. The MROD-X was not available at the time of the test beam. However the readout with the FILAR card was working fully satisfactorily.

The interface to the ELMB through the DCS computer running PVSS was used in this test beam to monitor the functionality of front-end electronics and to setup the values of threshold and gain for the MAROC chip in each PMF. It was also used to mask noisy channels. The operation of the interface was fully adequate. It will be kept very similar in the final detector implementation. The expected changes will be to add the monitoring of power voltages, currents, and temperature of the Motherboard.

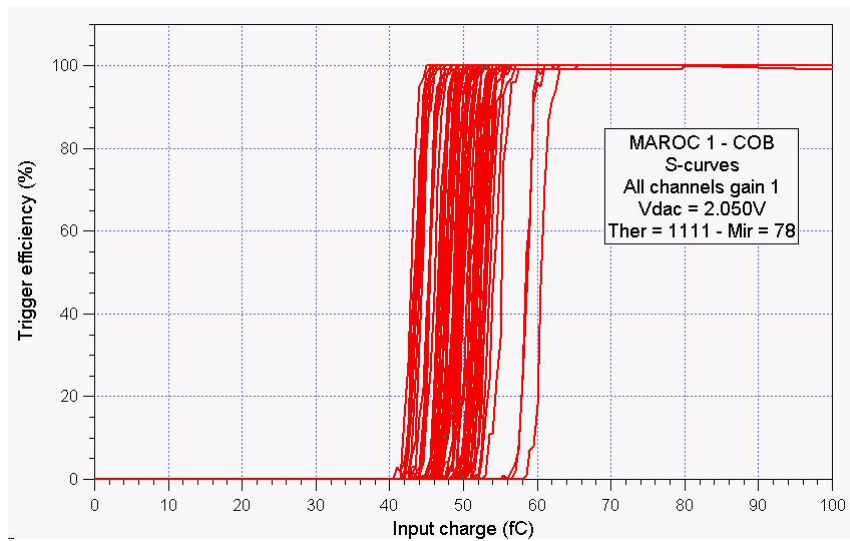


Figure 8-11 Trigger efficiency as a function of the input charge for the 64 channels of a MAROC 1 ASIC.

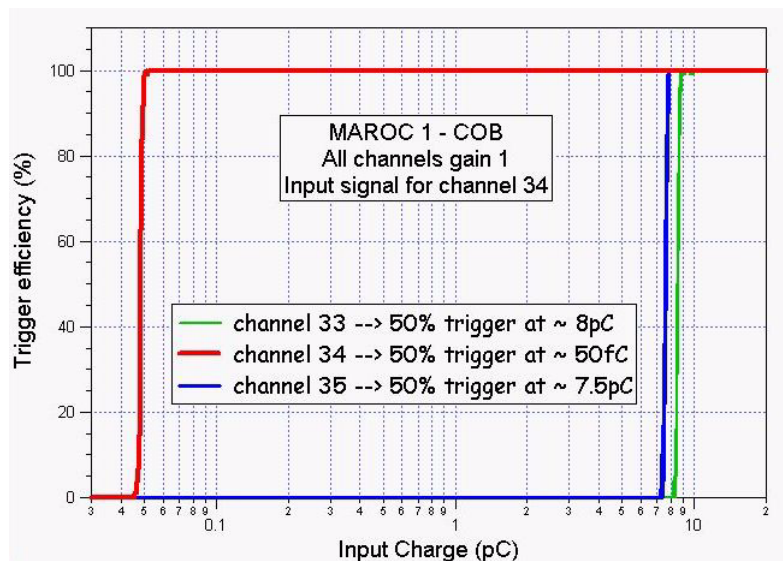


Figure 8-12 Trigger efficiency as a function of the input charge (log scale) for three neighbouring channels of a MAROC 1 ASIC. The central channel was the only one fed with signal.

The ELMB communicates with the DCS computer via the CAN (Controller Area Network) field bus, using a high level protocol, CANopen. The CAN interface card that has been chosen (Kvaser card), gives the possibility to have 4 different CAN buses connected and readout simultaneously by one PC slot. This implementation of the CAN interface is already proven to work for the distance between the ALFA detector in the LHC tunnel and USA15, the location of back-end computers.

The main problem encountered during the beam period was varying noise levels that were not completely understood. However, we identified a number of points on which to improve. The connections between the PMFs to the motherboards were far from optimal. Some limitations in the physical placements of the signals along the cables were creating direct interference between adjacent signals. The most critical was the one affecting the clock and we strongly suspect digital cross talk on the cable. The main change here

will be to adopt a new kapton flex cable. The signal will be differential and distributed as to isolate each pair from adjacent ones with ground lines. The use of kapton will also allow placing a shielding layer beneath the wires. Moreover, the number of connectors as compared to the test beam implementation will be reduced. These changes are expected to improve significantly the signal integrity. In addition to the use of a different cable there are changes implemented in MAROC2 that will make the chip less sensitive to external noise as compared to the first version of the chip. On top of this we also intend to make general improvements to the grounding scheme.

8.2.2.3 Spatial resolution

Two methods were used to assess the spatial resolution of *ALFA 10_2_16* prototype. Firstly, in the absence of a high resolution beam telescope the detector was sub-divided in two halves each consisting of 5 U and 5 V planes. The resolution can then be estimated from a comparison of the two reconstructed track segments in the two half-detectors. Secondly, at the end of the testbeam a common run was organised with the RD42 collaboration which provided a silicon telescope. In this case the telescope, which was installed about 1 m upstream of *ALFA* was used to predict the track position at the location of *ALFA*.

Spatial Resolution from a stand alone method

The tracks were reconstructed by *ALFA* as two independent track segments, using planes 1-5 (layers 1-10 = *ALFA_{H1}*) and planes 6-10 (layers 11-20 = *ALFA_{H2}*) separately. In this way the *ALFA* resolution could be studied without an external tracking detector, however, with limited possibilities to estimate the efficiency. The study was made using testbeam data where the MAPMTs were operated at 950 V. Special alignment runs were performed in order to align the detector perpendicular to the beam by minimizing the obtained spatial resolution.

In the absence of a magnetic field the track segments were assumed to be well described by straight lines. The track reconstruction was done by first selecting the candidate hits and then fitting the track. For the candidate selection among the fiber hits, a seed track was obtained by a Hough transform method [8-6] [8-7]. The closest hit with respect to the seed track was selected in each layer within two fiber widths away from the seed track. A track was then obtained by using the selected hits with the previously employed minimum overlap algorithm (see Section 8.1.1), which returns a *x-y* coordinate in the plane parallel to the detector layers.

Events were only used if their *x-y* position in the plane parallel to the layers was within a 2 mm radius from the centre of *ALFA*. This ensured that the selected particles transversed a region of *ALFA* where all 20 layers physically overlap. Figure 8-13 shows the residuals of the two track segments reconstructed by the two halves of *ALFA*. A Gaussian fit gives $\sigma_{\text{res}} = 56 \mu\text{m}$. As both half detectors are practically identical the spatial resolution of each of them is expected to be $\sigma_{H1} = \sigma_{H2} = \sigma_{\text{res}}/\sqrt{2} \sim 40 \mu\text{m}$. Comparison with the output of the geometrical Monte-Carlo code (see Section 5.3) allows to interpret the measured value. The Monte-Carlo code, with the as-measured detector geometry as input, predicts a full detector resolution of 20 μm and a half detector reso-

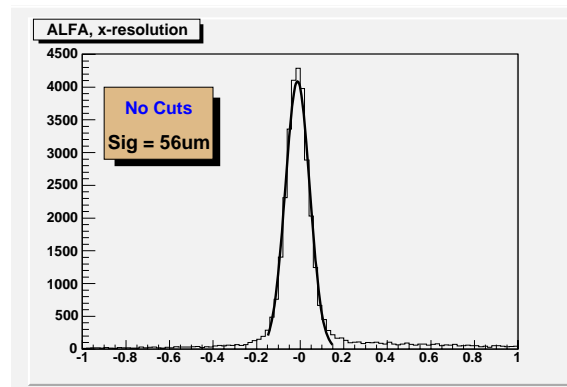


Figure 8-13 Residual of the two reconstructed track segments (mm).

lution of 30.5 μm . Based on this Monte-Carlo and some reasonable assumptions, the measured half detector resolution (40 μm) indicates a full detector resolution of $25 \pm 3 \mu\text{m}$.

Spatial Resolution determination with the beam telescope

During the regular ALFA testbeam period a reference tracking detector was not available but a few runs were taken afterwards together with the RD42 collaboration, which provided a high resolution silicon telescope. The telescope was mounted in front of the ALFA set-up and the tracks reconstructed by the telescope were extrapolated to the z-position of ALFA. After a software alignment of the telescope and ALFA coordinate systems the tracks positions of both systems could be directly compared. For ALFA the tracking algorithm outlined above is used calculate track positions both with the full detector and again with the two detector halves. In a first step the positions from the half-detectors are compared to telescope positions, and knowing the ALFA half resolution, the resolution of the telescope is determined. The distance between the telescope and ALFA is about 1 m and the intrinsic resolution of about 10 μm inside the telescope degrades to the observed telescope resolution of about 47 μm at the ALFA position. In a second step the tracks from the full ALFA detector are compared to the telescope prediction and from the residual distributions a spatial resolution for ALFA of $25 \pm 3 \mu\text{m}$ is extracted.

8.2.2.4 Overlap detectors

The prototype overlap detectors built for the test beam are described in [8-8]. They were made of two planes with 30 fibres each defining an active area of $15 \times 6 \text{ mm}^2$. A micrometer screw was used to move the upstream detector (OD2) with respect to the downstream detector (OD1)

In the data analysis, the vertical distance between the two detectors was reconstructed as the averaged difference between the positions of the fibres hit on each OD

$$y_{ODR} = \frac{1}{n} \sum_{i=1}^n \left[\frac{1}{2}(y_{OD2,1} + y_{OD2,2}) - \left(\frac{1}{2}(y_{OD1,1} + y_{OD1,2}) \right) \right] \quad 8-2$$

where $y_{ODk,l}$ is the position of the fibre hit in the layer l of the detector k and the sum is over the number of events. The n events were selected on the basis of the number of hit fibres. Only events with a total of 4 hits (one on each plane) were used for the reconstruction. Good correlation was found between the reconstructed and the set value y_{set} (see Figure 8-14). The difference between y_{ODR} and the straight line fit, plotted in Figure 8-15, is smaller than 20 μm . Most of the positions were independently measured for a second time. The two reconstructed positions are well compatible within the precision of the micrometric screw. The results obtained in this test beam validate the concept of the overlap detectors for the symmetric positioning of the ALFA detectors halves relative to the beam.

8.3 Plans for future prototype and test beam activities

The results obtained in the DESY (2005) and CERN (2006) test beam experiments validated the chosen detector concept, including the determination of the distance between the upper and the lower pot detector by means of the overlap detectors. Furthermore, the feasibility of a highly integrated and compact readout system based on the MAROC chip and FPGAs was demonstrated.

The natural next step is to build a full-size fibre detector consisting of 10 planes with 2×64 fibres and integrate it together with the overlap detectors and trigger scintillators in a Roman Pot. For the readout of

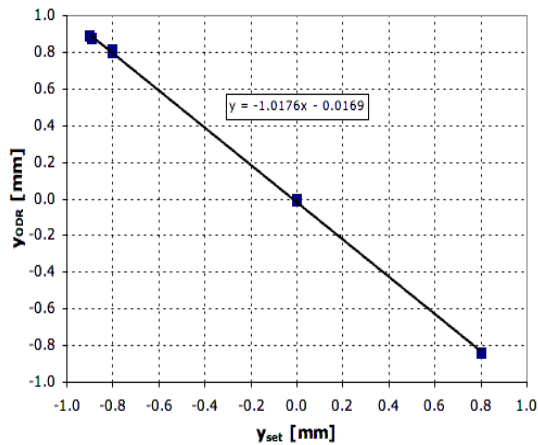


Figure 8-14 Reconstructed vertical distance y_{ODR} between the two detectors as a function of the mechanically set distance y_{set} . The straight line is a linear fit to the points.

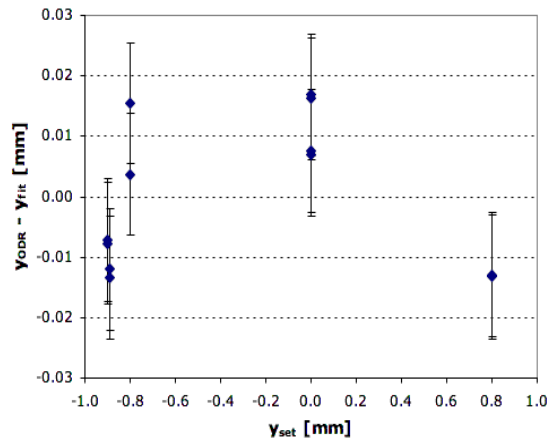


Figure 8-15 Difference between the reconstructed distance y_{ODR} and the fit for the same data. The error bars represent the quadratic sum of the errors from the reconstruction algorithm and the errors of the mechanical measurement.

the 1460 fibres 23 MAPMTs (Hamamatsu R7600) are required with the associated HV and readout cards, connected to the mother board. For the readout of the trigger scintillators (1 main detector + 2 overlap detectors) 3 conventional PMTs (Hamamatsu R1635) are needed.

We plan to complete this first full size Roman Pot module in spring 2008 and expect from it advances in the following areas:

- Test and optimization the various fabrication and integration techniques.
- Evaluation of the achievable mounting and alignment precision in the Roman Pot.
- Evaluation of the relative alignment precision between main and overlap detectors.

After this metrological analysis the module will undergo extensive lab testing which allows for

- Test and optimization of the readout system (MAPMT gain calibration and equalization), threshold optimization.
- Study and elimination of possible electronics noise sources.
- Software testing and debugging.

Finally, in spring 2008, tests in a high energy particle beam are planned which allow to assess the achievable performance under realistic conditions.

8.4 References

- 8-1 S. Ask, et al., “Luminosity Measurement at ATLAS - Development, Construction and Test of Scintillating Fibre Prototype Detectors”, Nucl. Instr. and Meth. A 568 (2006) 588-600.
- 8-2 A. Lucotte et al., “A front-end read out chip for the OPERA scintillator tracker”, Nucl. Instr. and Meth. A 521 (2004) 378-392.

- 8-3 P. Barrillon et al., “*Test of Scintillating Fibres Prototype Detectors using the OPERA front-end read out chip*”, ATLAS Note, ATL-COM-LUM-2006-005 (2006).
- 8-4 A. Braem, C. Joram, A. Mapelli, A. Kocnar, J. Pospichal, “*Metrology results of the ALFA 2006 prototype detectors*”, ATLAS Note, ATL-LUM-PUB-2006-007 (2006).
- 8-5 W. Iwanski, S. Haas and M. Joss, “*A PCI Interface with four 2 Gbit/s serial optical links*”, IEEE Trans. Nucl. Sci. **52** (2005) 2861
- 8-6 P. Hough, “*Method and Means for Recognizing Complex Patterns*”, U.S. Patent 3,069,654, 1962.
- 8-7 Duda, R. O. and P. E. Hart, “*Use of the Hough Transformation to Detect Lines and Curves in Pictures*”, Comm. ACM, Vol. 15, pp. 11–15 (January, 1972).
- 8-8 A. Braem, C. David, A. Folley, C. Joram, L. Kottelat, A. Mapelli, M. v. Stenis, H. Stenzel, and M. Szauter, “*Design, Construction and Metrology of Prototype Overlap Detectors for the ALFA System*”, ATLAS Note, ATL-COM-LUM-2006-008.

9 Performance estimations

9.1 Measurement method

The absolute luminosity calibration is obtained from a measurement of the t -spectrum of elastically scattered protons extending into the Coulomb Interference region at micro-radian sized scattering angles. The reach of this regime is a challenging task, since detectors have to approach the circulating beams at 1-2 mm distance, which requires well collimated beam spots obtained with a special beam optics. The dedicated optics for this experiment with $\beta^* = 2625$ m and a phase advance of the betatron function of 90° between the Interaction Point and the detectors in the vertical plane yields a parallel-to-point focusing, i.e. a linear relationship between the vertical impact position in the transversal detector plane and the vertical scattering angle at the Interaction Point. As discussed in Section 3.1, the 90° phase advance is not needed in the horizontal plane. Due to the left-right symmetry, the horizontal scattering angle can be calculated from the difference in the horizontal reconstructed position in the two arms.

In this section the experimental conditions for the luminosity calibration are discussed and the experimental systematic uncertainties are estimated. A detailed description of all experimental aspects is provided in [9-1].

9.2 Simulation setup

The performance estimation is based on a Monte-Carlo simulation of elastic pp-scattering supplemented by a beam transport program performing the tracking of particles through the lattice to the location of the Roman Pots. The response of the scintillating fibre detector is simulated and the impact positions (x, y) of tracks in each station are reconstructed. From each left-right pair $i = 1, 2$ of stations, a t -value is reconstructed according to:

$$-t_{i=1,2} = p^2 (\theta_{x,i}^{*2} + \theta_{y,i}^{*2}) \quad 9-1$$

The scattering angles are obtained by taking the difference of the position measurements at the left and right side, whereby the term from the vertex position at the Interaction Point cancels:

$$\theta_{u,i}^* = \frac{u_L - u_R}{2L_{eff,u,i}}, \quad L_{eff,u,i} = \sqrt{\beta_{u,i} \beta_u^*} \sin \psi_{u,i} \quad 9-2$$

The effective lever arm is determined by the betatron function and the phase advance ψ . The final value of t is obtained from the station average $t = (t_1 + t_2)/2$. The current simulation set-up uses a modified version of PYTHIA6.4 [9-2] [9-3], which was modified to include the Coulomb-term and the real part of nuclear amplitude for the elastic scattering process according to:

$$\frac{dN}{dt} = L \left(\frac{4\pi\alpha^2}{|t|^2} - \frac{\alpha\rho\sigma_{tot}e^{-\frac{b|t|}{2}}}{|t|} + \frac{\sigma_{tot}^2(1+\rho^2)e^{-b|t|}}{16\pi} \right) \quad 9-3$$

For the simulation $b = 18 \text{ GeV}^{-2}$, $\sigma_{\text{tot}} = 101.511 \text{ mb}$ and $\rho = 0.15$ were used, according to recent estimates [9-4]. Events were generated according to (9-3) in the t -range $5 \times 10^{-5} \leq t \leq 0.5 \text{ GeV}^2$ and the effective elastic cross section obtained by integrating (9-3) in this range is 34.3 mb . The properties of the beam at the Interaction Point are taken into account by smearing the incident angles and momenta of the incoming protons by the beam divergence $\sigma^* = 0.226 \mu\text{rad}$ for the angles in both planes and by the intrinsic energy uncertainty $\Delta p/p \approx 10^{-4}$ for the momenta. Crossing angle and vertical beam offset, present under collision optics for low β^* , are set to zero for the high β^* running. A normalised emittance of $\varepsilon_N = 1 \mu\text{m rad}$ is assumed. The vertex of the outgoing protons was smeared by the expected size of the beam spot $\sigma^* = 593 \mu\text{m}$. It should be noted that the divergence of the beam, although being small for the high β^* optics compared to the nominal collision optics, is still the limiting element in the t resolution. The outgoing protons are fed into the beam transport program MADX [9-5] for the tracking from the ATLAS Interaction Point to the Roman Pots. The apertures of beam screens, collimators and other beam defining elements are incorporated in the MADX setup. The particle positions and momenta are recorded by MADX at the longitudinal centre of each ALFA detector. The track coordinates (x, y) are smeared by a Gaussian distribution with a rms of $21 \mu\text{m}$, according to the expected tracking performance [9-6], confirmed by testbeam measurements at lower energy [9-7], as outlined in Section 8.1.

The basic event selection procedure requires a left-right coincidence and a reconstructed track in each of the four stations. With this selection the hit distribution observed in an ALFA detector is shown in Figure 9-1

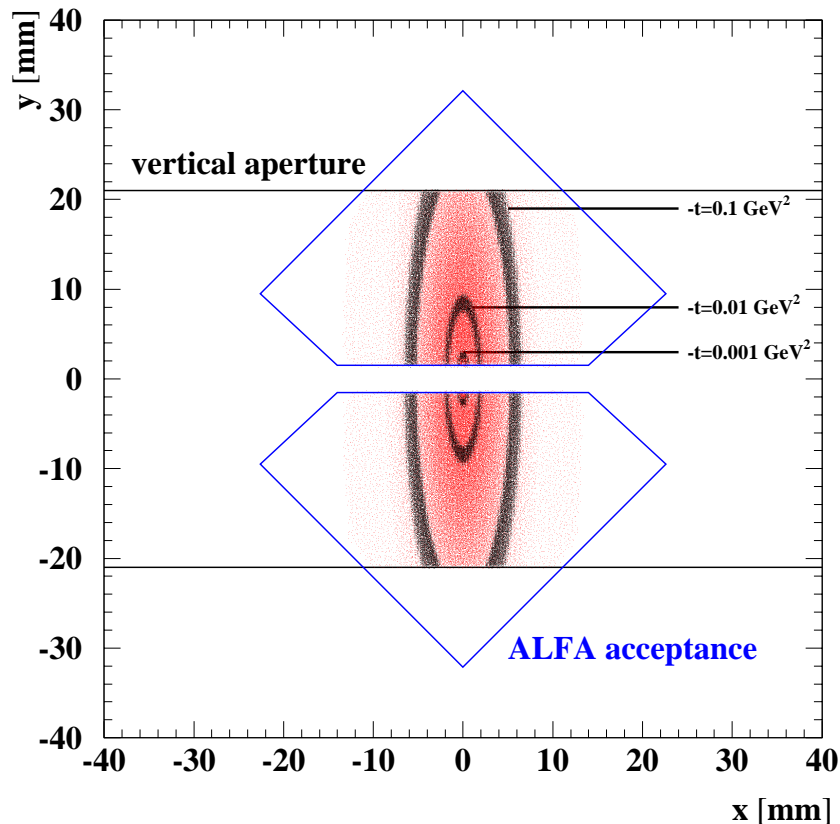


Figure 9-1 The distribution of impact points in an ALFA detector. The underlying hit pattern corresponds to 1 M events generated in the range $5 \cdot 10^{-5} \leq -t \leq 0.2 \text{ GeV}^2$, the highlighted bands are for selected t -ranges with $\pm 20\%$ width. The observed vertical aperture resulting from upstream beam elements is indicated.

9.3 Expected performance

For the purpose the performance evaluation a sample of 10 M elastic events in the specified t -range $[0,5 \times 10^{-5}, 0,5] \text{ GeV}^2$ were generated and passed through the simulation and reconstruction chain as outlined above. Accepted events are requested to fulfil the left-right trigger coincidence and to have space points reconstructed in 4 detectors

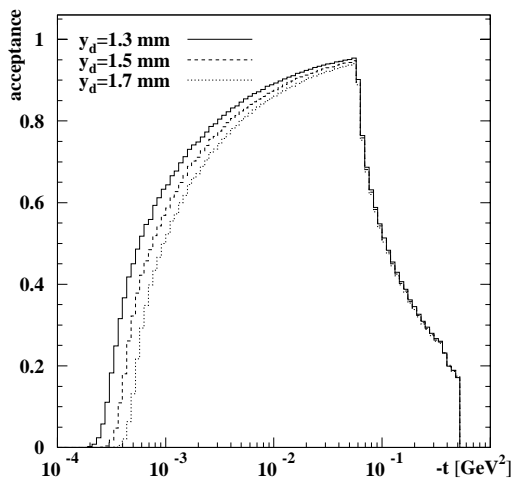


Figure 9-2 The geometrical acceptance as function of $-t$ for three distances to the beam.

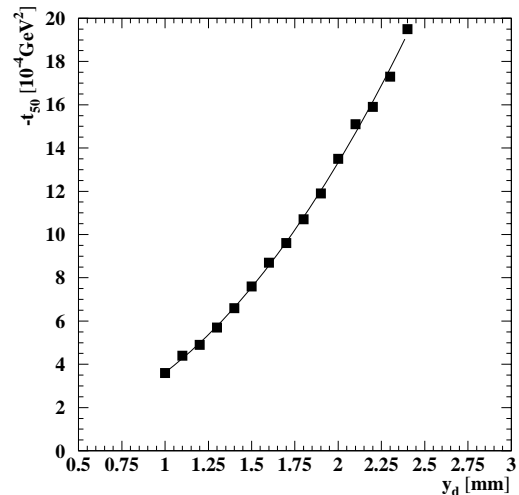


Figure 9-3 The reach in t_{min} for an acceptance above 50% as function of y_d

9.3.1 Acceptance

The geometrical acceptance of the detector is shown in Figure 9-2 as function of $-t$. The size of the beam spot at the ALFA detectors is about $130 \mu\text{m}$ in the vertical direction and the distance of closest approach of the detector to the beam centre will be between 10 and $20 \sigma_{\text{beam}}$, depending on the halo conditions. The acceptance for low t and subsequently the reach in sensitivity to the luminosity depend substantially on the distance to the beam, as shown in Figure 9-2 for three typical values for the distance of minimal approach between the orbit and the detector y_d . Integrated over all t and for a distance to the beam $y_d = 1.5 \text{ mm}$ about 67% of the 10 M events generated in the specified t -range are accepted. For the physics analysis of the t -spectrum we request a minimal differential acceptance of 50% in any bin of t in order to keep the associated corrections and their systematic uncertainties at a reasonable level. The reach in the minimal value of t , t_{min} , with an acceptance above 50% is shown in Figure 9-3 as function of y_d . It can be concluded that in order to reach the Coulomb Interference region defined by $|f_C| = |f_N|$ resulting in a value of $t_{min} \approx \frac{8\pi\alpha}{\sigma_{tot}} \approx 6 \times 10^{-4} \text{ GeV}^2$ with an acceptance of 50% the detector has to be placed at $y_d = 1.5 \text{ mm}$.

9.3.2 Resolution

The t -resolution depends on the angular beam divergence, the vertex smearing at the Interaction Point and the intrinsic detector resolution. On top of this a potential mis-alignment of the detectors with respect to the beam or an average non-zero crossing angle at the Interaction Point would entail a systematic shift of the t -scale. Furthermore, a precise measurement of the optical functions, in particular of the values of β^* , β and Ψ entering in L_{eff} will be mandatory to prevent systematic effects in the t -determination. The expected resolution including beam smearing but assuming perfect alignment and ideal optics is shown in Figure 9-4. At small t the resolution is dominated by the beam divergence and is about 10%. It follows an evolution scaling with $1/\sqrt{t}$ to larger t . The detector with an individual spatial resolution of 21 μm contributes only marginally to the total resolution. The impact of the spatial resolution is furthermore reduced by the fact that measurements from subsequent stations are averaged.

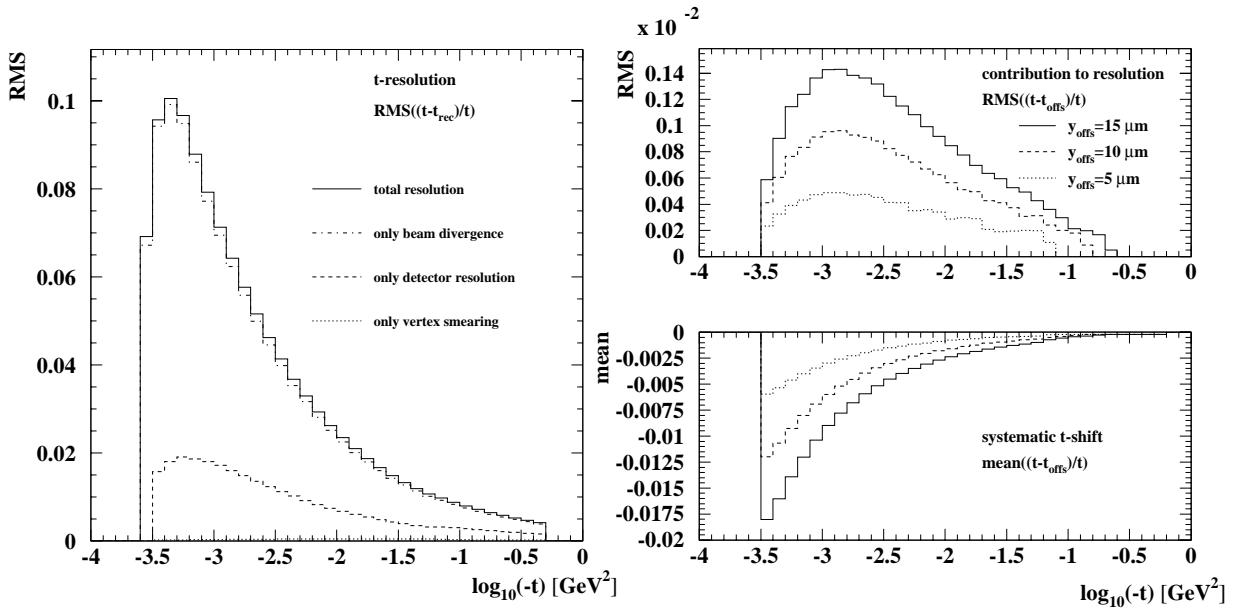


Figure 9-4 The width of the distribution of $(t - t_{rec})/t$ as a measure for t -resolution, for different effects contributing to the resolution.

Figure 9-5 Contribution from a vertical mis-alignment to the resolution and the systematic shift in the t -scale.

The alignment procedure discussed in Section 5.2.3 and Section 8.2.2.4 will yield a relative vertical positioning accuracy of about 10 μm . In Figure 9-5 the effect of a mis-alignment inducing a shift of the t -scale is illustrated.

9.3.3 Vertex reconstruction

With two stations separated by 4.14 m the difference of recorded space coordinates can be turned into a measurement of the local trajectory slope. Neglecting the dispersive term and using measurements of the track positions and angles at the Roman Pots the transport equation (3-1) can be inverted:

$$\vec{u}^* = \vec{u}M^{-1}, \vec{u} = \begin{bmatrix} u \\ \theta_u \end{bmatrix} \quad 9-4$$

This procedure allows to determine the transversal vertex at the Interaction Point with a modest resolution, shown in Figure 9-6. The vertex reconstruction receives contributions from the local slope, meas-

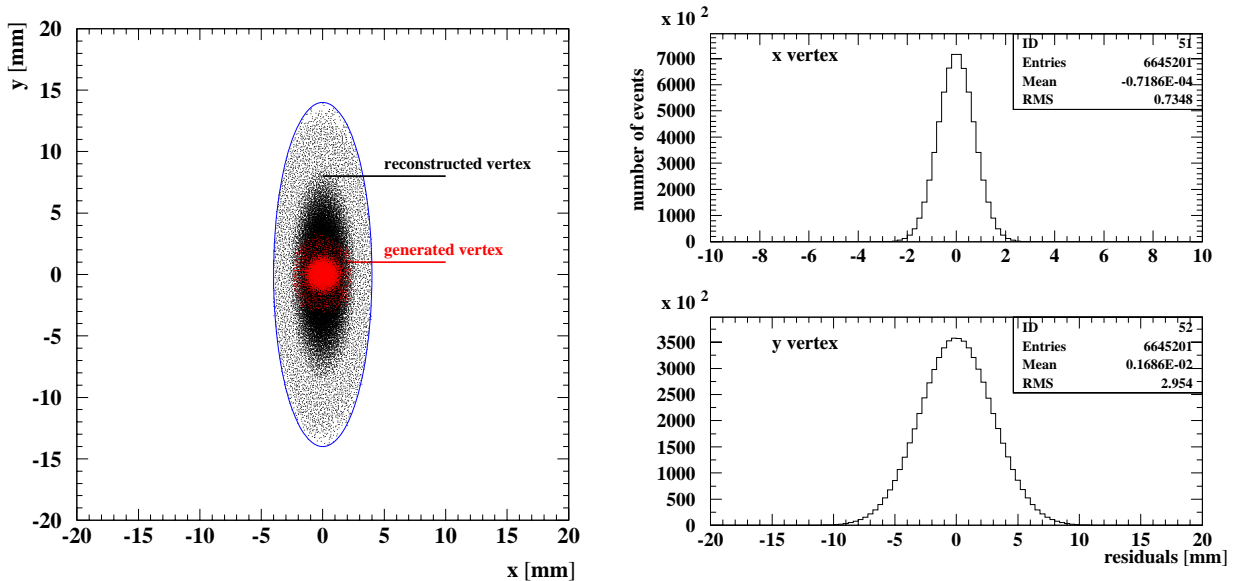


Figure 9-6 The reconstructed vertex position (black dots) compared to the true vertex (red dots), where the blue ellipse indicates the rejection cut (left). The vertex resolution in x and y (right).

ured with poor resolution, and to some extent from the high-precision local position measurement. The resolution is rather poor in y as a consequence of the parallel-to-point focusing, but in x a resolution of about 1 mm is obtained. The objective of the vertex reconstruction becomes clear in the context of the background rejection.

9.3.4 Background rejection

Two classes of background sources are considered: background originating from non-elastic interactions at the Interaction Point and background from accidental coincidences of halo events. Single diffraction processes are taken into account as source for non-elastic background. Double diffraction, minimum bias and deep-inelastic processes can either be excluded as background from their cross section or topology. The simulation for beam halo background contains distant quasi-elastic beam-gas interactions and protons surviving Betatron- and Momentum-cleaning collimation, as explained in Section 3.5.

9.3.4.1 Single diffraction background

A simple model [9-8] for single diffraction (SD) is implemented in PYTHIA with a cross section for $pp \rightarrow p + X$ of 14.3 mb, to be compared with the effective elastic cross section of 34.3 mb. While the scattered proton has kinematics similar to the elastic case and will often leave a signature in the ALFA detector, the particles generated by the diffractively dissociated proton are mostly absorbed by beam elements. Only a small fraction of these events will produce a particle at high energy and small scattering angle able to travel through the lattice. The background simulation proceeds along the same lines as for the elastic signal. According to the predicted SD cross section 4.2 M SD events are generated corresponding to 10 M signal events. Already at generator level an energy cut is imposed on the leading particle from the diffractive system. Only events where a proton originating from the diffractive system with an energy above

5 TeV is generated are passed through the lattice simulation. About 9% of the single diffraction events survive this cut. Particles with smaller energy are considered to be absorbed in the beam elements between the IP and the Roman Pots. The remaining events are passed through MADX. Out of these only 70% of the scattered protons and 17% of the protons from the diffractive system arrive to the level of the Roman Pots. A good fraction of these events is also outside the ALFA acceptance and only finally 0.33% of the events from the Interaction Point are seen by the detector. The remaining events are already at a negligible level and can further be reduced by acollinearity and vertex cuts.

The vertex cut is tuned to preserve the elastic signal and rejects events outside an elliptical area with half-axes 4 mm and 14 mm, as shown in Figure 9-6.

The acollinearity angles are defined by:

$$\phi_{A,u} = \left| \overline{\theta}_u^R + \overline{\theta}_u^L \right|, \quad \overline{\theta}_u = \frac{(\theta_{u,1} + \theta_{u,2})}{2}, \quad \theta_{u,i} \approx \frac{u_i}{L_{eff,u,i}} \quad 9-5$$

where the index $i = 1, 2$ refers to the two stations. In contrast to the t -reconstruction in (9-2), the acollinearity angle must be calculated individually from each arm, whereby the vertex contribution is neglected. Thus the resolution of the acollinearity is different in the two planes x and y , since the parallel-to-point focusing is only realised in the vertical plane, and therefore also different cuts are applied: $\phi_{A,y} < 1 \mu\text{rad}$ and $\phi_{A,x} < 5 \mu\text{rad}$, which preserve 99.7% of the elastic signal. In Figure 9-7 the acollinearity distributions for the elastic signal and the SD and halo background (see below) are shown. After applying the cuts the

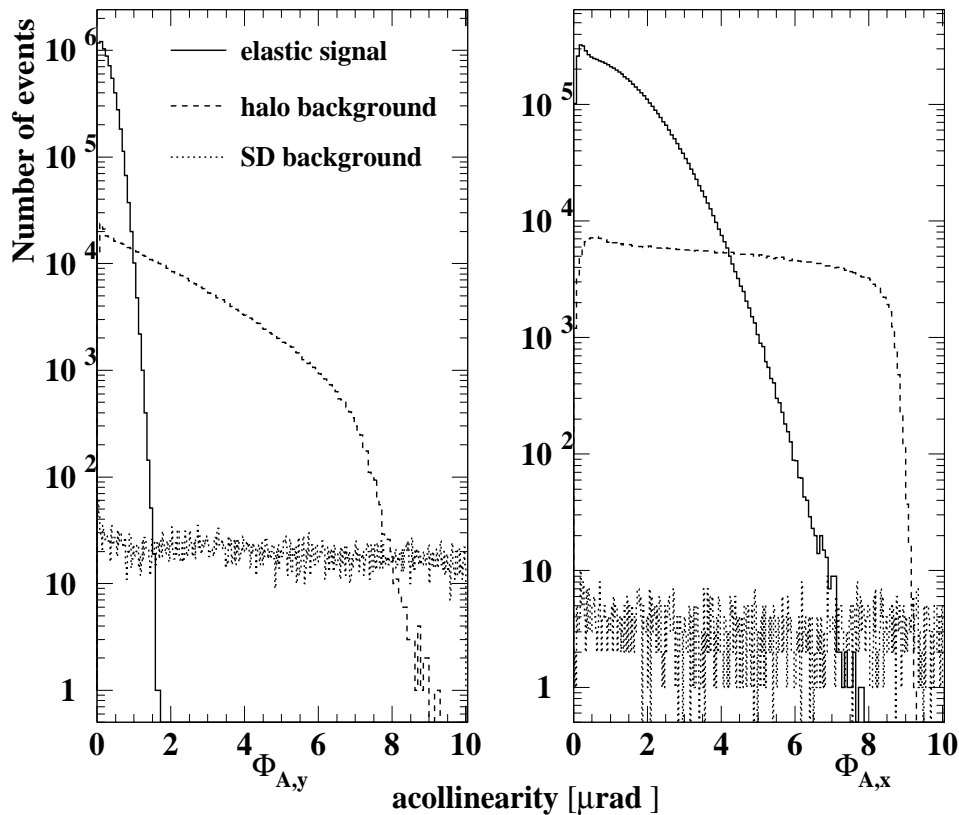


Figure 9-7 Distributions of the acollinearity angles in y (left) and x (right).

SD sample is reduced to 166 events, corresponding to 3×10^{-3} % of accepted elastic signal. At this stage no background subtraction is considered and also an eventual systematic uncertainty for the luminosity is neglected.

9.3.4.2 Halo background

The beam halo calculation outlined in Section 3.5.2 is used as input for the background simulation. The halo background events for the three processes of distant beam-gas scattering, momentum- and betatron cleaning are generated in proportion to their rates and overlaid to the elastic signal. Starting from the single rates for each background source, the accidental coincidence rate is calculated according to:

$$R_{acc} = R_{sngl}^2 \times \Delta_{tbunch} \quad 9-6$$

where the bunch separation time Δ_{tbunch} is 2.021 μ s for 43 bunches in the machine. For a cut on the vertical impact point of 11σ the rates are about 7.8 Hz for beam gas, 0.9 Hz for betatron cleaning and 0.03 Hz for momentum cleaning. The total halo rate of 8.7 Hz has to be compared to the elastic signal rate of about 27.8 Hz running at $L = 1 \times 10^{27} \text{ cm}^{-2} \text{ s}^{-1}$. About 2.82 M beam-gas events and 331 k cleaning events corresponding to 10 M elastic events were simulated. The overall contribution from halo background is much more important than from SD background. After applying the vertex and acollinearity cuts, shown in Figure 9-7, still about 140 k events or 2.1% of the elastic signal survive. Since these events have predominantly small t -values they have to be subtracted. The t -distribution of the irreducible background is compared to the signal for luminosity-relevant small t region in Figure 9-8.

The numbers of signal and background events present at each stage of the generation and rejection procedure is summarised in Table 9-1.

9.3.4.3 Background subtraction

The irreducible halo background to be subtracted off the measured t -spectrum can be determined directly from the data. The topology of the elastic signal induces an asymmetric hit pattern in the detector, meaning hits are recorded in either top stations of the left arm and bottom stations of the right arm or bottom stations of the left arm and top stations of the right arm. In contrast, the background is recorded in both the asymmetric and the symmetric configurations. The asymmetric configuration represents the irreducible background, the symmetric configuration can in absence of any elastic signal be used to determine the irreducible background. To get the t -spectrum of the symmetric sample the y coordinates in one randomly chosen arm have to be inverted. As a result a good estimate of the t -distribution of the irreducible background is obtained, as shown in Figure 9-9. A procedure was developed [9-1] to correct for eventual asymmetries of the background which would result in a normalisation difference between the sym-

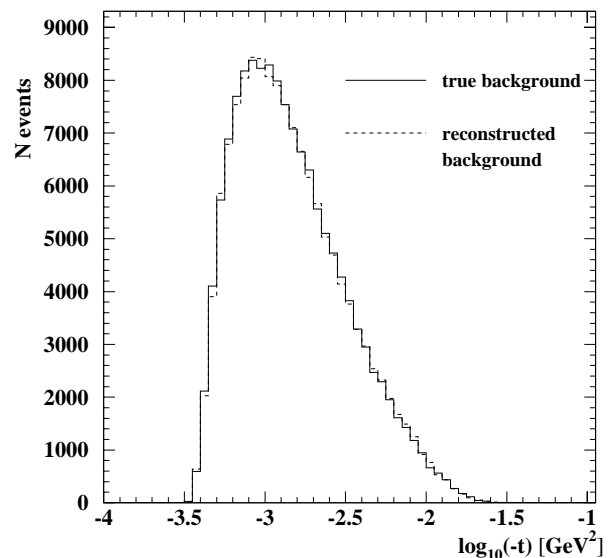


Figure 9-9 The true spectrum of irreducible halo background compared to the calculated spectrum using symmetric background events.

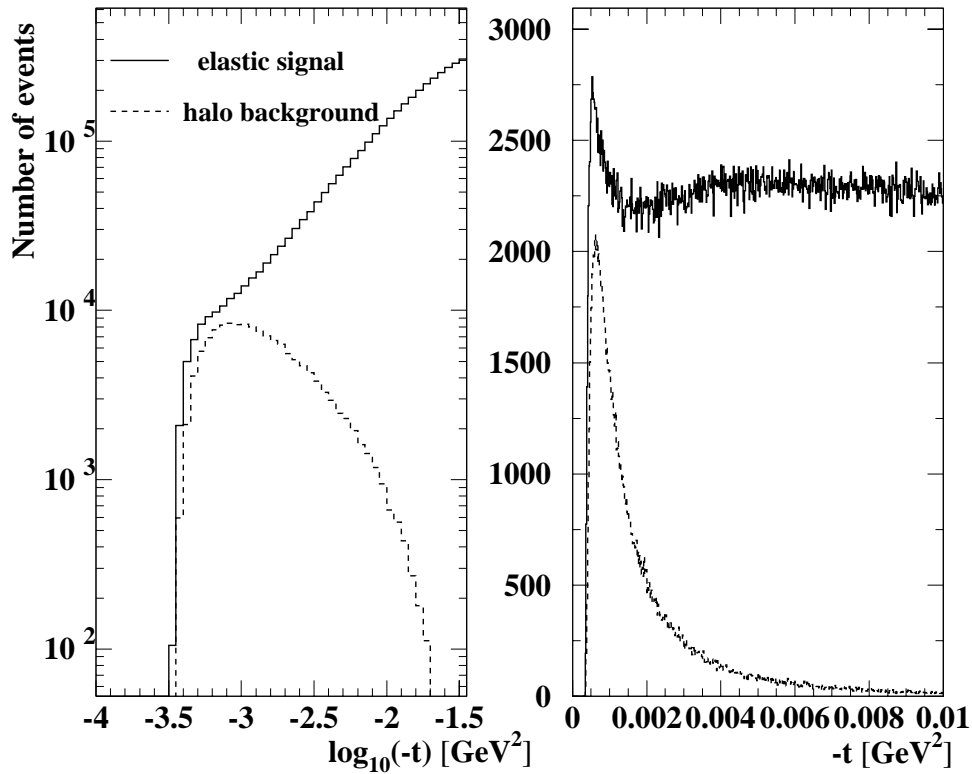


Figure 9-8 A zoom into the small t region in a logarithmic (left) and linear (right) representation of the distributions for the elastic signal and halo background.

Table 9-1 Summary of signal and background statistics in the rejection sequence.

	Elastic signal	SD background	Halo background
Cross section [mb]	34.3	14.3	-
Rate at $L = 1 \times 10^{27} \text{ cm}^{-2} \text{ s}^{-1}$ [Hz]	27.8	11.6	8.7
Number of generated events	10 M	4.2 M	3.2 M
Inside ALFA acceptance [%]	66.6	0.33	35.7
After vertex cut [%]	66.6	0.011	18.4
After acollinearity cut [%]	66.4	0.004	4.4
Final sample	6639285	166	139702

metric and asymmetric background. The advantage of this method is that it is free of any Monte-Carlo input and takes also background variations within the running period into account.

9.4 Luminosity and forward physics parameters

The absolute luminosity is determined from a fit of the elastic scattering formula (9-3) to the reconstructed and corrected t -spectrum. Together with the luminosity, entering as overall normalisation, the three physics parameters of the nuclear slope b , the total cross section σ_{tot} and the ratio of the real and imaginary nuclear scattering amplitude ρ are determined. The elastic cross section is about 34 mb, with large uncertainties, but in any case large enough to accumulate at low luminosity large statistics in a short period. In order to get a statistical precision in the luminosity of about 1.5% we need to accumulate 7 M events inside the fit range, corresponding roughly to a run of 100 hours at average luminosity of $L = 1.0 \times 10^{27} \text{ cm}^{-2}\text{s}^{-1}$.

9.4.1 Outline of the correction procedure

A number of corrections have to be applied to the raw reconstructed spectra before the fitting procedure can be launched. Denoting generically the t -distribution $D(t) = (dN)/(dt)$ the corrections can be organised as follows:

$$D^{\text{corr}}(t) = C^A(t) \cdot C^{\text{div}}(t) \cdot C^{\text{det}}(t) \cdot (D^{\text{meas}}(t) - D^{\text{bac}}(t)) \quad 9-7$$

where:

- $D^{\text{corr}}(t)$ is the resulting corrected t -spectrum
- $D^{\text{meas}}(t)$ is the measured raw spectrum
- $D^{\text{bac}}(t)$ is the calculated background to be subtracted
- $C^{\text{det}}(t)$ is the correction for detector resolution
- $C^{\text{div}}(t)$ is the correction for the beam divergence
- $C^A(t)$ is the correction for experimental acceptance

Each correction accounts for a specific effect, background subtraction, detector acceptance, beam divergence and detector resolution, the latter includes also reconstruction imperfections like the neglected contribution from the beam dispersion. Full details of the correction procedure are given in [9-1]. In the simplest case the corrections can be cast into bin-by-bin corrections. A transition matrix correction accounting for off-diagonal migrations can be considered for the divergence.

9.4.2 Luminosity fit

Out of the generated 10 M elastic events 6.6 M events were selected and used in the luminosity fit. The detectors are placed at a vertical distance of 1.5 mm from the beam, corresponding to 12σ . The fit range was set by requiring an acceptance above 50%. The t -spectrum was reconstructed in two representations, for t in a linear scale with 10000 equidistant bins and for a logarithmic variable $\tau = \log(-t)$ in 100 bins. The two representations of the t -distribution after all corrections are shown in Figure 9-10, together with the fit result.

The expression for the elastic spectrum given in (9-3) is fit to the spectra with four free parameters, the luminosity, the total cross section, the ρ -parameter and the nuclear slope. The nominal fit results are summarised in Table 9-2. The luminosity is determined with good accuracy and also a fair estimate of the

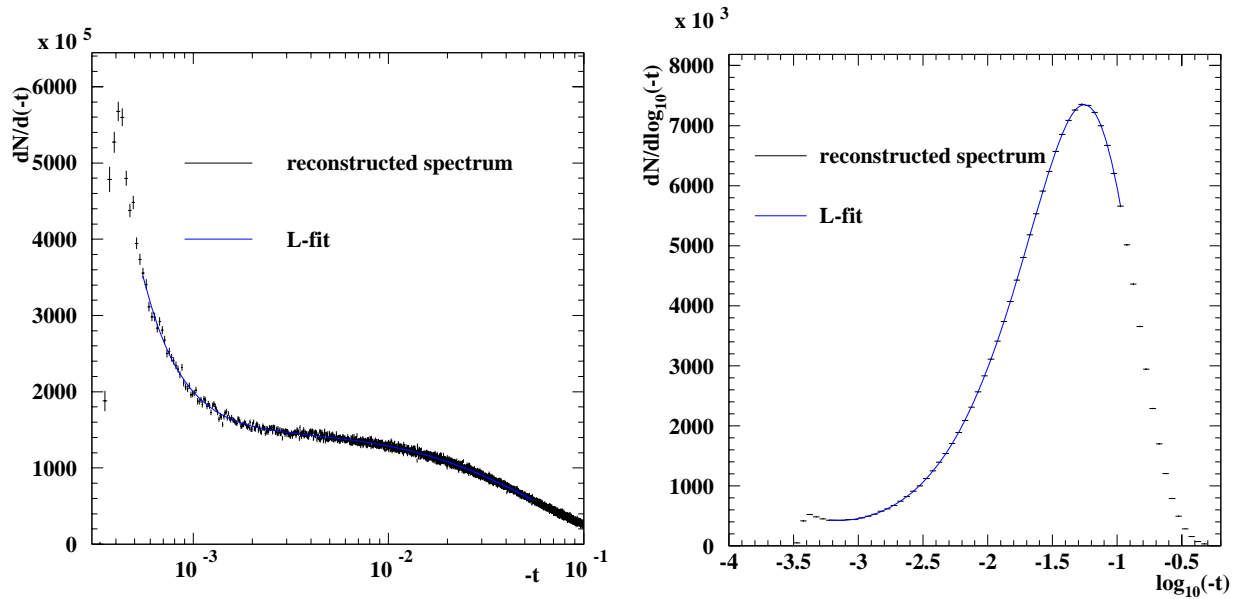


Figure 9-10 The reconstructed and corrected t -spectrum in two representations, linear(left) and logarithmic (right), together with the resulting luminosity fit.

Table 9-2 Fit results for the luminosity and forward physics parameters.

	Input	Linear fit	Error [%]	Log. fit	Error[%]
L [$10^{26} \text{ cm}^{-2} \text{ s}^{-1}$]	8.10	8.151	1.77	8.057	1.89
σ_{tot} [mb]	101.511	101.14	0.9	101.77	1.0
b [GeV^{-2}]	18	17.93	0.25	17.97	0.12
ρ	0.15	0.143	4.3	0.146	3.8
Fit range		$0.00055 < -t < 0.055$		$-3.2 < \tau < -1.0$	
Fit quality [χ^2/Ndof]		2845/2723		33.2/44	

forward physics parameters is obtained. There is however a large statistical correlation between the parameters, in particular between the luminosity and the total cross section. The correlation is different for the linear and logarithmic fit and depends on the fit range. As a consequence the parameter errors for the two fit options are slightly different.

9.4.3 Systematic uncertainties for the luminosity

Experimental systematic uncertainties arise from a limited precision of the knowledge of the properties of the beam, the background and the detector. For some aspects like the background the level of precision is currently not well known and assumptions have to be made.

9.4.3.1 Beam divergence and crossing angle

The divergence of the incoming proton beams at the ATLAS Interaction Point produces a systematic distortion, which has to be corrected by means of a Monte-Carlo correction. As input to the simulation the actual value of the divergence is needed. The beam divergence is expected to be known to $\pm 10\%$. The corrections were for systematic purposes re-calculated with a divergence value shifted by $\pm 10\%$ and used in conjunction with the nominal data set to determine the luminosity. The difference of the fit result with respect to the nominal luminosity is about 0.3% and assigned as systematic uncertainty. All experimental systematic uncertainties are summarised in Table 9-3. The crossing angle could in principle have a non-zero mean value, an upper limit can at least be estimated using special beam position monitors (see Section 3.7). For a mean crossing angle of $0.2 \mu\text{rad}$ and using the same procedure as for the divergence, a systematic uncertainty of about 0.2% is observed. As already explained in Section 3.7, this uncertainty can be somewhat increased without any significant impact on the total error.

9.4.3.2 Optical functions

The values of β and β^* are needed at the reconstruction step, the relevant term in the expression for the effective lever arm is $\sqrt{\beta\beta^*}$. As outlined in Chapter 3.7 β^* can be determined with a relative uncertainty of 1% and β with 2%, for $\sqrt{\beta\beta^*}$ an uncertainty of 2% is conservatively assumed. Changing the effective lever arm by this amount leads to a systematic error for the luminosity of about 0.7%.

The phase advance of the betatron function between the Interaction Point and the Roman Pots must also be controlled precisely. Its value $\sin\Psi$ is again needed for the t -reconstruction. It is assumed that the phase advance can be measured with an uncertainty of 0.5° . This level of precision is in particular necessary for the measurement of the horizontal component of the scattering angle, where the phase advance is about 180° and a small variation entails a large change in the luminosity. The resulting luminosity uncertainty of about 1-1.5% is actually dominated by the contribution from the horizontal plane.

9.4.3.3 Detector related systematics

The most important systematic uncertainty stemming from the detector is the vertical alignment. An asymmetric displacement of the detector halves leads to a shift of the t -scale and more important also changes the acceptance. Following the procedure detailed in Section 5.2.3, it is assumed that individual detectors (upper relative to lower) can be aligned to better than $10 \mu\text{m}$. To estimate the systematic effect each detector is displaced by $10 \mu\text{m}$, in either direction. It is further assumed that a potential mis-alignment is uncorrelated for different detectors and all possible configurations with 8 detectors being mis-aligned by $\pm 10 \mu\text{m}$ are considered and for each configuration the luminosity is fit. The final uncertainty is obtained by averaging all equally likely configurations, giving rise to an uncertainty of about 1%.

The nominal detection area, determining the detector acceptance correction, is also to be measured with high accuracy. The metrology measurements on the final prototype will be verified in a test beam with an accuracy of $\pm 10 \mu\text{m}$. Propagating this uncertainty into the luminosity yields a effect of about 0.5%.

Finally the detector resolution is studied. This parameter is less critical, assuming that the true spatial detector resolution is about $30 \mu\text{m}$ instead of $21 \mu\text{m}$ will induce a luminosity uncertainty of about 0.3%.

9.4.3.4 Background

With a background subtraction method based on the data without use of simulation the associated systematic error can be expected to be very small. In fact, the main effect is of statistical nature since the differ-

ence between the true background and the calculated background is only due to fluctuations in either of the samples. The procedure to estimate this effect is a generation of a series of background samples all with the nominal population which are in turn added (for the asymmetric part) and subtracted (for the symmetric part) to the signal sample, whereafter the luminosity is fit. The RMS of the obtained luminosity values is assigned as systematic uncertainty. The systematic error obtained in this way is between 1.1% for the linear fit and 1.5% for the logarithmic fit.

Table 9-3 Summary of experimental systematic uncertainties.

Systematic uncertainties [%]	Linear fit	Logarithmic fit
Nominal result for L	8.15	8.06
Statistical error	1.77	1.89
Beam divergence	0.31	0.30
Crossing angle	0.18	0.15
Optical functions	0.59	0.76
Phase advance	1.0	1.4
Detector alignment	1.3	0.9
Geometrical detector acceptance	0.52	0.43
Detector resolution	0.35	0.19
Background subtraction	1.10	1.51
Total experimental systematic uncertainty	2.20	2.57
Total uncertainty	2.82	3.19

9.4.4 Limitations and future improvements

The present analysis is the second iteration of simulation series started with the Letter of Intent [9-9]. It is obvious that a number of items have to be improved at a later stage:

- A full GEANT4 simulation of the entire set-up.
- Integration of simulation and reconstruction software in the ATLAS framework.
- Evaluation of theoretical uncertainties of the elastic scattering formula, including form factors and electromagnetic phase effects.

9.5 Summary

The simulation carried out to estimate the performance with the proposed optics and detector specifications indicates that the luminosity can be measured with the required 3% precision. The dominant systematic uncertainty is related to the optical functions, the detector alignment and the halo background.

9.6 References

- 9-1 H. Stenzel, “*Luminosity calibration from elastic scattering*”, ATLAS Note, ATL-COM-LUM-2006-010 (2006).
- 9-2 T. Sjostrand et al., “*High-Energy-Physics Event Generation with PYTHIA 6.1*”, Computer Physics Commun. (2001) 238.
- 9-3 T. Sjostrand et al., “*PYTHIA 6.4 physics and manual*”, JHEP05 026 (2006).
- 9-4 COMPETE Collaboration, J.R. Cudell et al., “*Benchmarks for the Forward Observables at RHIC, the Tevatron Run II and the LHC*”, Phys. Rev. Lett. 89 201801 (2002).
- 9-5 MADX homepage: <http://mad.web.cern.ch/mad>.
- 9-6 V. Vorobel and H. Stenzel, “*GEANT4 simulation of the testbeam set-up for the ALFA detector*”, ATL-LUM-PUB-2006-006 (2006).
- 9-7 S. Ask, et al., “*Luminosity Measurement at ATLAS - Development, Construction and Test of Scintillating Fibre Prototype Detectors*”, Nucl. Instr. and Meth. A 568 (2006) 588-600.
- 9-8 G.A. Schuler and T. Sjostrand, “*Hadronic diffractive cross-sections and the rise of the total cross-section*”, Phys. Rev. D 49 (1994) 2257-2267.
- 9-9 ATLAS Collaboration, “*ATLAS Forward Detectors for Luminosity Measurement and Monitoring*”, Letter of Intend, CERN-LHCC/2004-010 (2004).

10 Machine interface, commissioning and operation

10.1 Beam interlock, beam loss monitors and machine protection

Machine protection is of course an important issue for detectors working very close to the beam. Functional specification for how the Roman Pots have to be interlocked to the machine has been worked out by the TS/LEA and AB/OP groups in collaboration with the experiments [10-1]. In short, the Roman Pots can only move into their IN position when the status of the machine is set to STABLE BEAMS. As soon as the machine status turns to UNSTABLE BEAMS the Roman Pots have to automatically go to their OUT position. The OUT position will be defined by the end switches that are installed on all Roman Pot units. If the Roman Pots are not in the OUT position for any other mode of the machine, a beam dump request will automatically be generated.

Beam loss monitors will be installed close to the Roman Pots to monitor the effect of beam losses generated by the beam halo interacting with the Roman Pots and the Roman Pot detectors. The purpose of those monitors is not only to understand the impact of the continuous losses but they will also be part of the machine protection system. At the LHC, Beam Loss Monitors (BLM) will be installed close to all known potential loss locations and the Roman Pot BLMs will be part of this system. They will be linked to the Beam Interlock system so that the beam can be dumped in a timely manner. One could also envisage an intermediate alarm threshold, which would simply move out (or stop the movement) the Roman Pots and not dump the beam. The best location of the monitors for an adequate response and optimum sensitivity to the losses on the Roman Pot has been studied with Monte-Carlo simulations and will be the bases for the positioning of the BLMs [10-2].

Independently of the beam status, an unforeseen breaking of the secondary vacuum of the pot could of course occur. However this should not lead to a breaking of the pot window. The window has a capability to stand the atmospheric pressure with a safety factor of 1.5 and broke in an ultimate pressure test at 83 bar. A breaking of the secondary vacuum should thus only lead to a deformation of the window. Another scenario that has been studied [10-3] is the accidental loss of a bunch on the Roman Pot window. The study was performed for the case of a full nominal bunch hitting the window in the middle. During the high beta runs the bunch intensity will be typically well below $3 \cdot 10^{10}$ particles/bunch. Using the results in [10-3] and extrapolating to these lower bunch intensities, it is clear that the increase of temperature in the window is below the melting point of iron.

The motors of the Roman Pots may also fail. The mechanics of the unit has to be such that any failure of the motors or its power supplies leads to an automatic withdrawal of the pot. The mechanics is being studied for this.

10.2 Radiation environment

In order to avoid radiation damage to the detector, even when it is sitting in its garage position, we will carefully monitor the level of radiation. Radiation Monitors [10-4] will be installed close to the Roman Pots and if needed we will remove the detector with its electronics when the radiation levels become too high. This will be a straight forward procedure and will be done without breaking the primary vacuum. The pot will remain installed and the secondary vacuum in the pot will be re-established with a dummy flange.

Induced radioactivity is of course an issue for any interventions. Estimation of the activation levels indicates that the levels will be acceptable [10-5] but obviously the real levels have to be measured at the moment of the intervention. Detailed procedures for interventions have to be agreed upon with SC/RP specifying how many people enter in the tunnel and for how long.

10.3 Cables and other services

The cabling interferes in general with most of the work in the tunnel and should thus be planned at an early stage. Potentially, the cabling of the Roman Pots and its detectors could also interfere with the out baking of the vacuum chambers of the beam and with the installation of delicate alignment equipment in the so called geometers gallery. In order to avoid these possible sources of interference the cabling campaign had to be done already the summer 2006. The fast Flexwell cables for the trigger were installed as well as low voltage power cables for the detectors. Cables for motor control and limiting switches and position sensors have also been installed. Actually all cabling work, except the high voltages cables, is now finished. The cables will be connected to the Roman Pot units via a patch panel located close to the Roman Pot unit. The patch panel will feed both the lower and upper pot. The front end electronics and the mother board are attached to Roman Pot flanges as discussed in Section 4.2.2 and Section 6.3. In addition to the Roman Pot units, we also need to install the low voltage power supplies in the tunnel. The power supplies have the required level of radiation hardness and acceptable locations in the tunnel (RR alcoves) have been found and agreed upon. There will be no pump installed in the tunnel. We will instead use a mobile system which will be brought out after pumping the secondary vacuum.

10.4 Powering the high beta optics

The high beta optics can be powered with the same scheme as the standard low beta optics. However the fourth quadrupole (Q4) in the lattice of the long straight section has to work with a different polarity as compared to the standard optics (see Section 3.2).

The hardware to allow the change of polarity for Q4 has been prepared and installed in RR13 (RR17) by the AB/PO group. For the startup of the machine the cables will be connected using copper plates to the standard polarity. Later on for the luminosity runs these can be replaced by a switch (mechanical or remotely controlled) to allow fast changes between the two configurations.

10.5 Commissioning

The commissioning of the Roman Pot units (without detectors) is planned for the shut down 2008-2009. Our intentions are to test as much as possible of the movements system, the position reading system and the controls in the laboratory to minimize the necessary commissioning time in the tunnel. Once the Roman Pot unit will be installed in the tunnel with the movement system operational, it will be necessary to commission the interlock system and simulate alarm conditions.

The detectors are scheduled to be ready for installation some time during the first part of 2009. Once installed in the tunnel we will test the detector connectivity. If the expected level of luminosity allows it, we will keep the detectors inside the pots with the pots in their garage position during the normal low beta running in 2009. In this way we will be able to make a first detector commissioning using halo particles

and we will also be able to get some first ideas about the halo background. During the high beta runs time will be very limited and thus we have all interest to prepare as much as possible beforehand.

10.6 Operation

The Roman Pots will be part of the collimator control system. This is in line with the strategy for LHC operation that aims at providing a coherent approach to the operation of all movable objects in LHC. By having the Roman Pots controlled and operated by the collimator control system, it will be assured that the pots will always be in the shadow of the collimators and therefore protected towards a too high flux of beam or halo particles. The idea is to ensure that at no stage of operation the Roman Pots are positioned in a place that would compromise the safety of the machine and the safety of the Roman Pots themselves. Obviously all the collimators have to move into their positions before the Roman Pots will be allowed to start to move.

Also it is important to ensure that the Pots are in their parking positions during injection. All this points imply a scheme with the Pots being operated from the Main Control Room but of course in direct contact with the experiment. If at a later stage the experiments will get special access to the collimator control system it will only concern the Roman Pots and there will always be hardware system to prevent the pots getting closer to the beam than allowed by the collimator settings.

Each pot will move and approach the beam independently. During the motion there will be a constant feed back from the Beam Loss Monitors, from the Beam Position Monitors and also from the Roman Pot detectors themselves. As already mentioned above, the detector has to get as close as possible to the circulating beam, but without any sizeable perturbation. It is known that the background rate is varying slowly as a function of the distance to the beam down to about $10 \sigma_{\text{beam}}$ (see Figure 3-7). The approach to the beam will be done in several steps and will of course be discussed with the LHC operation group taking into account the experience gained in running in the collider. Each step is followed by a cross check with the expectations estimated by the beam optics calculations and the feed back from simultaneous beam orbit measurements.

As an example of a possible scenario, the strategy of approaching the beam as experienced in previous experiments is suggested below:

1. All detectors in outer position and measure the counting rate in all trigger counters. This will serve as reference measurement.
2. All detectors OFF in outer position, except the closest detector to the intersecting region and only on one side (top or bottom) of the circulating beam. Move the detector in steps of 0.2 mm down to 3 mm and record the rate in the trigger counter. Continue in steps of 0.1 mm. The pot is immediately retracted if a sudden background increase is seen in the rate measured in the trigger counters.
3. Get the detector used in step 2, to a position 0.5 mm further away from the beam that the limit reached previously and do the same procedure for the more downstream pot on the same side of the beam
4. Repeat the procedure for the two detectors on the other side of the circulating beam starting from 2). At that stage the position and width is known on one side of the crossing point and must be checked carefully with the expectations.
5. Repeat the same operation from 2) to 4) for the second arm. At that stage, beam position, width and angle will be known.

Depending on beam intensity and available time, a first data taking can take place. This will allow to measure precisely all beam parameters and make a detailed comparison with beam optics calculations. The beam approach procedure has to be repeated at each fill of the machine up to sufficient knowledge on its stability.

10.7 References

- 10-1 LHC Experiments Beam Interlocking , EDMS document 653932.
- 10-2 R.J Hall-Wilton, D. Macina and T. Talanov, “*Recommended Locations of Beam Loss Monitors for the ATLAS Roman Pots*”, CERN-TS-Note-2007-003 (2007).
- 10-3 E. Dimovasili and D. Macina, “*Energy deposition in the window of the TOTEM Romain Pot for the nominal TOTEM run*”, CERN-TS-Note-2005-051 (2005).
- 10-4 T. Wijnands, Radiation Monitoring for Equipment in the LHC tunnel, EDMS document 565013.
- 10-5 E. Dimovasili, TS/LEA note to be published.

11 Responsibilities, cost and schedule

11.1 Responsibilities

The following institutes are directly involved in this project: CERN, Charles University Prague, Institute of Physics Academy of Sciences of Czech Republic, Palacky University, DESY, Humboldt University Berlin, IFIC Valencia, Justus-Liebig-University Giessen, LAL Orsay, LIP Lisbon, Lund University, University of Manchester, Stony Brook University. A preliminary and approximate definition of the sharing of the different hardware responsibilities is given in Table 11-1 below. Observe that some of the institutes mentioned above have no direct hardware responsibility but participate in one way or another. The project has been broken up in four different categories: the ALFA detector, the electronics, the Roman Pots with its mechanics and movement system and finally the general infrastructure. In all the following tables, ATLAS stands for resources provided by the ATLAS Collaboration through its Common Fund and Technical Coordination.

Table 11-1 ALFA responsibilities.

Items	Responsibilities
ALFA Detector	CERN, DESY, Giessen, Humboldt, Lisbon, Prague
Electronics and Read out	CERN, Lund, Orsay
Roman Pots and their mechanics	ATLAS, CERN, DESY, Orsay, Prague
General infrastructure	ATLAS

11.2 Cost

The costs corresponding to each of the four categories are given below in somewhat detailed tables (Table 11-2 to Table 11-6). These tables also give a more complete idea of how the responsibilities among the different institutes are divided within each category.

Table 11-2 ALFA detector cost (kCHF).

Items	Cost	Responsibilities
Prototypes 2005, 2006, 2007	68	CERN, Giessen
Fiber tracker	80	Giessen
Titanium plates	30	Humboldt
Aluminization	40	Lisbon
Trigger counters	40	DESY
MAPMTs	310	DESY (125), Prague (50) + 80 PMTs reused from Giessen
Total ALFA detector	568	
Total with contingency	600	

Table 11-3 Electronics and Read Out cost (kCHF).

Items	Cost	Responsibilities
Prototypes PMF	20	Lund
Production PMF	43	Orsay
Prototype motherboard	10	Lund
Production motherboard	30	Lund
Prototype MAROC	20	Orsay
Production MAROC	40	Orsay
FPGA	10	CERN
TTC, DCS, MRODX	55	CERN
Custom trigger preprocessor	15	Not identified yet
HV power supplies	80	DESY
LV power supplies	25	Not identified yet
Total Electronics and read Out	348	
Total with contingency	375	

Table 11-4 Roman Pots cost (kCHF).

Items	Cost	Responsibilities
Prototyping	58	ATLAS, CERN
Bare Pots	27	Not identified yet
Mechanics	113	CERN (25), DESY (25), Orsay (25), Prague (38)
Instrumentation (motors, LVDTs)	73	ATLAS
Total mechanics	271	
Total with contingency	300	

Table 11-5 Infracstructure cost (kCHF).

Items	Cost	Responsibilities
Cables (installation, connectors)	194	ATLAS
Roman Pots pedestals	15	ATLAS
Polarity inverter	50	ATLAS
BPM	20	Not identified yet
Total Infracstructure	279	
Total with contingency	300	

Table 11-6 Summary cost (kCHF), including contingencies.

Items	Cost
ALFA detector	600
Electronics and Read Out	375
Roman Pots mechanics	300
Infrastructure	300
Total project	1575

11.3 Schedule

Below we discuss the preliminary schedule for the project. Again we break down the project in the same four categories as for the cost above. For a general overview, see Figure 11-1.

11.3.1 ALFA detector

As described in chapter 5 we have already constructed small prototype detectors that have been used in test beams to validate the concept. Next step is to construct one complete detector corresponding to one full Roman Pot or 1/8th of the total system. This work has started the summer 2007 with a tight planning in order to be ready for spring 2008. We would then like to validate this full prototype in laboratory tests and test beam. The full detector could be ready for installation during 2009 as seen in the overall planning of Figure 11-1.

11.3.2 ALFA electronics

We plan to have a full size prototype consisting of 23 PMF's and a motherboard ready for testing beginning 2008. The following sequence with lab tests and test beam and production would allow the electronics to be ready by end December 2008.

11.3.3 Roman pot mechanics

We are in the process of validating the prototype. We need about 6 months for the production and the assembly. The testing will be done during the first part of 2008.

11.3.4 Infrastructure

The remaining work related to the infrastructure consists of installing the few remaining cables and put on connectors on all cables. Once this is done the cables will be commissioned. All work related to cables will be finished in January 2008.

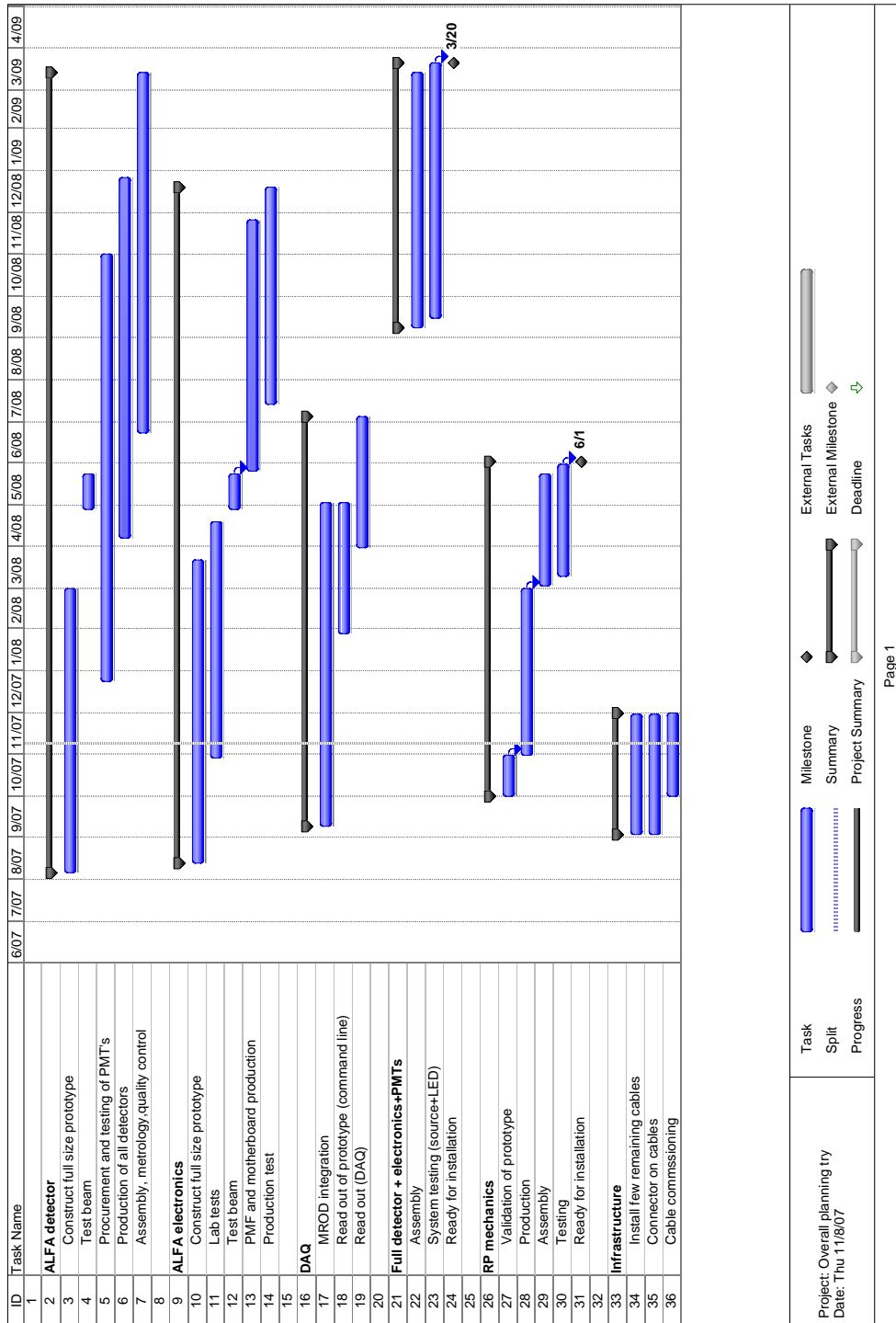


Figure 11-1 Overall ALFA planning overview.

A Members of the ATLAS ALFA Collaboration

CERN

European Laboratory for Particle Physics (CERN)

F. Anghinolfi, S. Ask, G. Blanchot, A. Braem, H.J. Burckhart, H. Burkhardt, B. Di Girolamo,
I. Efthymiopoulos, P. Farthouat, S. Franz, P. Grafstrom, W. Iwanski, C. Joram, A. Mapelli, S. White

Czech Republic

Charles University, Faculty of Mathematics and Physics, Prague

R. Leitner, T. Sykora, V. Vorobel

Institute of Physics, Academy of Science of the Czech Republic, Prague

J. Ridky

Palacky University, Olomouc

M. Hrabovsky, A. Kocnar

France

Laboratoire de l'Accélérateur Linéaire, Univ. Paris-Sud, CNRS/IN2P3, Orsay, France

P. Barrillon, S. Blin, S. Cavalier, C. Cheikali, P. Cornebise, D. Cuisy, C. De la Taille, D. Fournier,
M. Gaspard, M. Haguenaer¹, M. Heller, B. Lavigne, P. Puzo, N. Seguin-Moreau

Germany

Justus-Liebig University Giessen, Giessen

M. Düren, S. Hoffmann, H. Stenzel

DESY, Hamburg und Zeuthen

R. Ciesielski, I. Gregor, T. Haas, W. Hain, K.-H. Hiller, S. Levonian, E. Lobodzinska, H. Kowalski,
D. Notz, D. Petschull, U. Schneekloth

1. Work performed within LAL Orsay group.

Humboldt Universität Berlin, Institute für Physics, Berlin

M. Jablonski, T. Lohse

Great Britain

Department of Physics and Astronomy, University of Manchester, Manchester

B. Cox, F. Roncarolo

Portugal

Laboratorio de Fisica Experimental e Instrumentacao em, Particulas, Lisbon, Portugal

J. Faustino, L. Gurriana, A. Maio, M.J.P. Maneira, Y. Nunes, P. Conde Muino, J.G. Saraiva, A. Palma

Spain

Instituto de Fisica Corpuscular IFIC, Univ. de Valencia

A. Faus-Golfe

Sweden

Dept. of Experimental High Energy Physics, University of Lund, Lund

B. Lundberg, U. Mjornmark, V. Hedberg

United States of America

Dept. of Physics and Astronomy, Stony Brook University, Stony Brook

M. Rijssenbeek, M. Thioye

This TDR could not have been written without the essential engineering and technical support of the staff of all participating institutes. We warmly thank everyone that has contributed with her or his valuable competence to the work described in this TDR.